UNIVERSITÀ DEGLI STUDI DI MILANO

Scuola di Dottorato in Fisica, Astrofisica e Fisica Applicata

Dipartimento di Fisica

Corso di Dottorato in Fisica, Astrofisica e Fisica Applicata

Ciclo XXVI

On the Nature of the Pygmy Dipole Resonance in ^{124}Sn via Inelastic Scattering of ^{17}O

Settore Scientifico Disciplinare FIS/04

Tutor: Prof.ssa Angela BRACCO

Cotutor: Dott. Oliver WIELAND

Coordinatore: Prof. Marco BERSANELLI

Tesi di Dottorato di:

Luna PELLEGRI

Anno Accademico 2013-2014

Commission of the final examination:

External Referee:
Prof. Elias KHAN

External Member:
Prof. Santo LUNARDI

Internal Member:
Prof. Gianluca COLÓ

Final examination:

Date 07/03/2014
Università degli Studi di Milano, Dipartimento di Fisica, Milano, Italy

MIUR subjects:

FIS/04 - FISICA NUCLEARE E SUBNUCLEARE

PACS:

24.30.Cz- Giant Resonances (nuclear reactions)
25.70.-z - Heavy-ion reactions: low and intermediate energy

Alla mia famiglia

Contents

Introduction

The atomic nucleus is a many-body quantum system in which the occurrence of collective excitations is a common feature. Giant Resonances (GR) are an example of collective modes in nucleus. Their study over the years has provided useful information on the nuclear structure and on the effective nucleon-nucleon interaction, as well as on the bulk properties of nuclear matter such as the compression modulus and the symmetry energy. In particular, the understanding of the electric-dipole response around the binding energy is presently attracting considerable interest since the dipole strength distribution in that region affects the reaction rates in astrophysical scenarios, where photo disintegration reactions are important. In addition, the E1 strength is expected to provide information on the neutron skin and thus on the symmetry energy of the equation of state. The first evidence of an accumulation of low-lying E1 strength in heavy nuclei, larger than that due to the tail of the giant dipole resonance (GDR), dates back to early 70's. However, only in recent years, experimental and theoretical investigations, on both stable and unstable nuclei, revealed that this is a common phenomenon in most atomic nuclei. The accumulation of E1 strength around the particle separation energy is commonly denoted as pygmy dipole resonance (PDR) due to the much smaller size of its strength in comparison with the giant dipole resonance (GDR). The hydrodynamical model describes this pygmy strength as associated to the vibration of the neutron skin against the N = Z core. From the experimental point of view, the PDR has been investigated systematically in a large number of stable nuclei with the photon scattering technique. As the electromagnetic interaction of γ-rays is well understood, it allows model-independent derivation of absolute transition strengths. Additionally this method is very selective to E1 transitions. Both in stable and in exotic nuclei, however, the use of an electromagnetic probe allows

only for the measurement of the transition strength of the resonance. In order to gain more insight in the structure of the PDR, it is necessary to obtain more explicit information also on wave functions and transition densities. To this end one needs to measure the PDR with reactions where the nuclear part of the interaction is involved. An interesting feature in the region of the pygmy resonance has been observed in a number of different stable nuclei, by comparing results of photon-scattering, (γ,γ'), and α-scattering, , (α,$\alpha'\gamma$), experiments. In particular, it has been found that one group of states is excited in both type of reactions, while another group of states at higher energies is only excited in the (γ,γ') case. These experimental findings are in qualitative agreement with different phonon models which predict a low-lying isoscalar component dominated by neutron-skin oscillations and a higher-lying group of states with a stronger isovector character associated to the tail of the giant dipole resonance.

In order to verify if this splitting is a common feature of the pygmy resonance, it is necessary to measure the PDR using different hadroic probes in different mass regions. Therefore, an experiment has been performed at Legnaro National Laboratories (LNL) in Italy, aimed at the study of the gamma decay from high-lying bound and unbound states in several nuclei (^{124}Sn, ^{208}Pb and ^{140}Ce). The resonance states were populated using inelastic scattering of ^{17}O heavy ions at $\sim$ 20 MeV/u. The main aim of the experiment is the investigation of the microscopic structure of highly excited dipole states below particle threshold (in the energy region between 5 to 10 MeV), where pygmy dipole structures are expected to have a sizeable strength, especially in neutron-rich nuclei. The use of heavy ions inelastic scattering at approximately 20 MeV/u to study highly excited states is a good tool when the measurement of the subsequent gamma decay is also performed with high resolution. For this reason, the γ-rays produced during the de-excitation of the target have been measured using an array of highly segmented HPGe detectors (the AGATA Demonstrator) coupled to an array of 9 large volume $LaBr_3$:Ce scintillators (the HECTOR$^+$ array) used to increase the detection efficiency for high energy γ-rays. The detection of the scattered ^{17}O ions and and the measurement of the excitation energy transferred to the target nucleus was performed with two segmented ΔE-E silicon telescopes (pixel type), a prototype project called TRACE. The subject of this thesis has been the investigation of the nature of the PDR in

^{124}Sn nuclei. In summary, in Chapter 1 Giant Resonance modes will be described, while in Chapter 2 the method used for the excitation of these collective states will be presented. The experimental set-up and the data analysis will be reported in Chapter 3 and 4, respectively. Finally, the experimental results will be shown in Chapter 5.

Chapter 1

Giant Resonances

In this Chapter we briefly discuss the main aspects which are relevant for the study of the high-energy collective vibrational modes. In particular, we describe the general properties of such states (sec. 1.1) and their decay mechanism (sec. 1.2). We then focus on a particular type of collective vibration called Pygmy Dipole Resonance (PDR), which is the subject of this thesis, focusing on the theoretical models used to describe this resonance and on the experimental investigations (sec. 1.3).

1.1 General Features

The atomic nucleus is a many-body quantum system in which the occurrence of collective excitations is a common feature. Giant Resonances (GR) are an example of collective modes in nucleus. Their study over the years has provided useful information on the nuclear structure and on the effective nucleon-nucleon interaction, as well as on the bulk properties of nuclear matter such as the compression modulus, the symmetry energy, etc. Their main properties will be now recalled, following [1] and [2].

A Giant resonance can be interpreted as a high-frequency, damped, nearly harmonic vibration of the density or shape around the equilibrium of the nuclear system. The vibration amplitude is small, only a few per cent of the nuclear radius. A typical example of a giant resonance is shown in Fig. 1.1 where the absorption

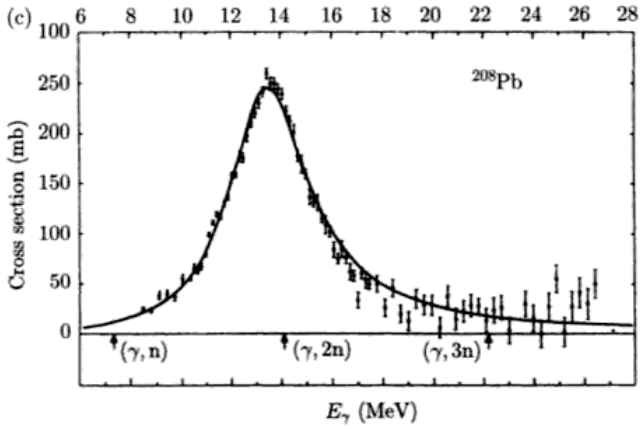

Figure 1.1: The photo-neutron cross section $\sigma(\gamma, n)$ as a function of the photon energy for ^{208}Pb [2].

cross section of photon energy for ^{208}Pb is depicted.

The experimental data are fitted with a Lorentzian curve function:

$$\sigma(E) = \frac{\sigma_m \Gamma_m^2 E^2}{(E^2 - E_m^2)^2 + \Gamma_m^2 E^2} \tag{1.1}$$

where σ_m, E_m and Γ_m are, respectively, the peak cross section, the resonance energy and resonance width. It has to be noticed the peak cross section is related to the strength S_R via a normalization factor. Typically, the centroid energy of a giant resonances lies well above the neutron separation energy (8-10 MeV), with a corresponding vibration frequency of $\sim 10^{21}$ Hz. Their width is of the order of 2.5-5 MeV implying that after a few vibrations the resonance is already completely damped owing to energy dissipation. The strength of a giant resonance is limited by and generally close to the maximum allowed by sum rule considerations: it can, indeed, be shown that in many quantum systems the sum of all transition strengths for a given set of quantum numbers is limited by basic properties of the system, which would be for example the number of nucleons A and the atomic number Z in the case of a nuclear system.

As a giant resonance is a collective motion of all nucleons it has to be expected that whatever mode it corresponds to, its characteristic properties do not depend

on the detailed microscopic structure of the nucleus but rather on its bulk structure. Indeed, giant resonances of various nature have been observed over the years throughout the mass table and their parameters have been shown to vary smoothly with the number of nucleons A. Although it should be noted that the width of a giant resonance is also dependent on the microscopic structure of the nucleus, due to direct particle emission and to the coupling to more complex configurations.

1.1.1 Classification of Giant-Resonance Modes

Macroscopic Description

The first evidence of a giant resonance excitation was found in 1937 in a measurement of (γ, n) cross-section in various target [3]. The resonance was interpreted by Goldhaber and Teller [4] and Steinwedel and Jesen [5] as the excitation of a collective nuclear vibration in which all the protons in the nucleus move collectively against all the neutrons resulting in a separation between the center of mass and center of charge thus creating an electric dipole moment. This vibration is known as the Giant Dipole Resonance (GDR) which is excited by electromagnetic dipole field of the photons. Many other vibrational modes are possible.
Giant resonance modes can be classified according to the multipolarity L, the spin S and the isospin T quantum numbers. A schematic view of the various type of resonance for multipolarity $\Delta L = 0, 1, 2$ is shown in Fig. 1.2

- Electric ($\Delta S = 0$) Isoscalar ($\Delta T = 0$) vibrations in which the protons and neutrons oscillate in phase according to a multipole pattern defined by $\Delta L = 0, 2, ...$ To first order the $\Delta L = 1$ vibration corresponds to a translational motion of the nuclear centre of mass and is thus not an intrinsic nuclear excitation; however, there is a higher-order $\Delta L = 1$ vibration as will be discussed.

- Electric ($\Delta S = 0$) Isovector ($\Delta T = 1$) vibrations in which protons oscillate against neutrons according to a multipole pattern defined by ΔL. For the same multipolarity, isovector modes have a higher excitations energy due to extra energy required to separate the protons from neutrons.

- Magnetic or spin-flip ($\Delta S = 1$) Isoscalar ($\Delta T = 0$) vibrations in which nucleons with spin up oscillate against nucleons with spin down, again in a

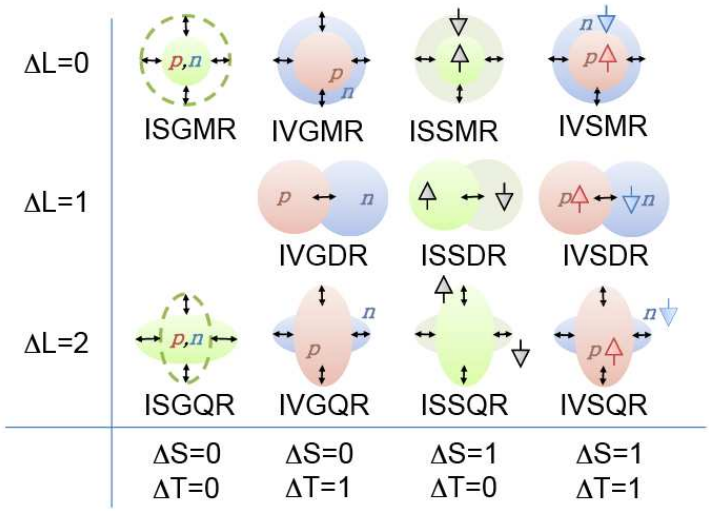

Figure 1.2: Classification of giant resonances according to the multipolarity, spin and isospin quantum numbers, taken from [1].

multipole pattern given by ΔL.

- Magnetic or spin-flip ($\Delta S = 1$) Isovector ($\Delta T = 1$) vibrations in which protons with spin up (down) oscillate against neutrons with spin down (up).

Microscopic Description

From a microscopic point of view giant resonances are commonly described as coherent superimposition of particle-hole excitations coupled to the same angular momentum, spin and isospin of the resonance. The giant resonance state can be seen as resulting from the operation on the ground state of the nucleus with a one-body operator:

$$|\Psi_{GR}^{\lambda,\sigma,\tau}\rangle = O^{\lambda,\sigma,\tau}|\Psi_{g.s.}\rangle \tag{1.2}$$

where λ refers to the multipolarity of the resonance, σ its spin and τ its isospin, respectively. For example, the electric isoscalar transition operator has the form:

$$O_{\mu}^{\lambda,0,0} = \sum_{i=1}^{A} r_i^{\lambda} Y_{\lambda\mu}(\Omega_i), \quad \lambda \geq 2 \tag{1.3}$$

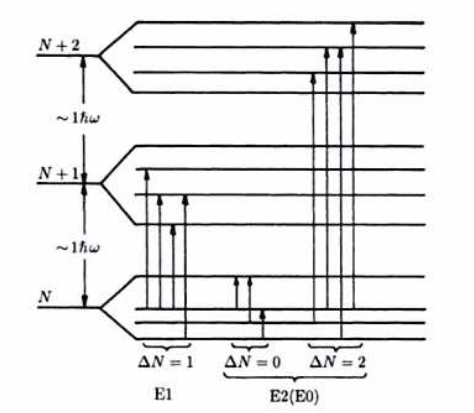

Figure 1.3: Schematic picture of E1 and E2(E0) single-particle transitions between shell-model states, taken from [2].

where the summation runs over all nucleons i.
The qualitative features of giant resonances can be understood by considering a schematic shell-model picture.

Fig. 1.3 shows a schematic picture of E1 and E2(E0) single-particle transitions between shell-model states. The single-particle wave functions in a subsequent shells N, N+1, N+2, ... have alternating parity and an energy difference $\Delta E = \Delta N \times 1\hbar\omega = \Delta N \times 41A^{-\frac{1}{3}}MeV$. The operator $O_{\mu}^{\lambda,0,0}$ can only induce transitions with $\Delta N \leq \lambda$ while, because of parity conservation, odd λ transitions require $\Delta N = 1, 3...$ and even λ transitions $\Delta N = 0, 2...$. Owing to the presence of a residual particle-hole interaction, a collective state is formed which is a coherent superimposition of all possible particle-hole states of a given multipolarity and parity.

More accurate microscopic descriptions of giant resonances are obtained with mean field models and effective nucleon-nucleon interactions. The most common approach is to describe the ground state of the nucleus with the Hartree-Fock method, generating a self-consistent mean field from the effective two-body interaction. The ground state is then a Slater determinant of a single-particle orbitals where all the states below the Fermi surface are fully occupied and all the states above are empty. One can then study the effect of a small-amplitude density fluc-

tuation, induced by an external field, around the equilibrium configuration. The fluctuations can be described with the time-dependent Hartree-Fock equation, and in the small-amplitude limit one can derive the Random-Phase Approximation (RPA) equations, which allow to diagonalize the residual interaction in the complete space of 1p-1h (one particle - one hole) configurations. Second order RPA calculations include 2p-2h to account for the coupling of the resonance to more complex configurations. Other excitations of the RPA can be made to include the coupling to the continuum states (CRPA) or the effects of pairing correlations (QRPA, quasiparticle RPA).
Mean field approaches have been very useful in describing the properties of nuclei near the β-stability valley; the improvement in experimental technique, however, makes it possible to study nuclei farther from stability, for which Relativistic Mean Field (RMF) approaches have been shown to be able to better reproduce the experimental data, in particular regarding the spin-orbit term (which is a parameter in non-relativistic approaches and is naturally derived from the Lagrangian in RMF approaches). It is also possible to build a self-consistent Relativistic RPA (RRPA) on top of a RMF description of the ground state, in order to study collective vibrations in a relativistic framework. RRPA can be extended to include the coupling to continuum states (CRRPA), which is very important with weakly bound exotic nuclei, and to include the pairing effect (QRRPA).

1.2 Decay Mechanism of Giant Resonances

As mentioned before, typical range values of centroid and FWHM of giant resonances are 10-15 MeV and 3-5 MeV, respectively. Consequently, giant vibrations go only through few periods of excitation before relax one. The decay of a giant resonance is explained by different mechanisms, each one contributes to the total width of the resonance. They can be characterized by whether the energy of the vibration escapes the system, or it is redistributed into other degrees of freedom within the system. The contributions to the total width Γ are:

- $\Gamma^{\downarrow}$: damping width, caused by the coupling of the 1p-1h states of the giant resonance to more complex configurations; it is the dominant contribution to the total width.

- $\Gamma^{\uparrow}$: escape width, which accounts for the direct emission of particles, since the 1p-1h state lies above the particle emission threshold; typically $\frac{\Gamma^{\uparrow}}{\Gamma} \sim 10^{-1}$
- Γ^{γ}: photon emission width, which is a much smaller contribution than the escape width because the particle emission is favoured ($\frac{\Gamma^{\gamma}}{\Gamma} \sim 10^{-4}$)

The damping of giant resonances is a prime example of how a well-ordered collective excitation dissolves into a disordered motion of internal degrees of freedom in fermionic quantum many-body system. At the high excitation energy of the giant resonance, indeed, there is a high density of 2p-2h configurations with the same spin and parity as resonance. The 1p-1h state can mix with 2p-2h states, which in turn mix to 3p-3h states, in a process that goes up in a hierarchy of complexity that ends in a state which the excitation energy has been spread over all degrees of freedom and a compound nucleus is eventually formed.
This scheme implies a hierarchy of time scales, corresponding to the lifetimes characteristic for each coupling step, and corresponding energy scales ranging from total width of the resonance, of the order of some MeV, to width of compound nuclear states of the order of eV. The search for experimental evidence of this picture is a long-standing problem.

1.3 The Pygmy Dipole Resonance

In atomic nuclei the isovector electric dipole (E1) strength is almost completely exhausted by the isovector giant dipole resonance (IVGDR), located in the energy range between 10-20 MeV, which has been investigated intensively using various experimental approaches [2, 6]. A small faction of a few percent of the total E1 strength is exhausted by the so-called Pygmy Dipole Resonance (PDR), a concentration of $J^{\pi} = 1^{-}$ states around the particle threshold.

In the recent years, the study of the PDR has attracted a great deal of interest in the nuclear structure community not only driven by an understanding of the underlying nuclear structure of this phenomenon, but has been further stimulated by implications to other subjects.
One application of the PDR is based on a possible relation between its total strength and the thickness of the neutron-skin [7]. Thus, a better understanding of the

structure of PDR provides an experimentally constrained approach to determine the neutron skin thickness of atomic nuclei in a complementary way compared to the others. The neutron-skin thickness itself is determined by the symmetry energy of the equation of state (EOS) and directly linked to its parameters [8, 9]. Since the EOS is a key ingredient in the description of dense astrophysical objects such as neutron stars, experimental constraints on the EOS are highly demanded.
Another implication of the PDR is its influence on reaction rates in the astrophysical r-process [10, 11] which synthesizes about 50% of the elements heavier than iron. The photon-absorption cross section σ_γ is directly related to the γ-ray strength function, which is an important input in calculation of neutron capture cross section and the corresponding (n, γ) rates. How strongly this finally influences the distribution of the produced elements in the r-process depends on the astrophysical scenario. However, since the relevant isotopes in the r-process are extremely neutron rich one has to rely on model calculations for the E1 strength distribution in these nuclei.

An overview on the theoretical models and the experimental investigations will be discussed in the following sections.

1.3.1 Theoretical Models

The PDR can be described in the most simple way as an out of phase vibration of a $N = Z$ core against a skin formed by the excess neutrons. A first theoretical interpretation of this excitation mode was given by a simple three-fluid hydrodynamical model which involves classical oscillations of the nucleon fluids [12]. The three fluids, here, are the protons, the neutrons sitting in the same orbitals as the protons and the excess neutrons. These led to two independent electric dipole resonances, one originating from the oscillation of all protons against all neutrons and an energetically lower lying mode where only the excess neutrons oscillate against a proton-neutron saturated core.

In recent years, various microscopic approaches are used including Hartree-Fock and Hartree-Fock-Bogoliubov plus (quasi-particle) random-phase approximation (Q)RPA based on different interactions [7], second RPA calculations [13], the

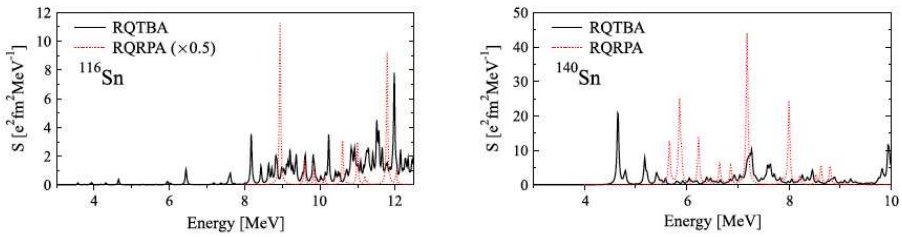

Figure 1.4: E1 strength distribution in the region calculated up to 12 MeV for ^{116}Sn (left) and up to 10 MeV for ^{140}Sn (right) in RQRPA and RQTBA [11].

quasi-particle phonon model (QPM) including complex configuration [14], the extended theory of finite Fermi systems (ETFFS) [15], the Landau-Vlasov equations [16], the relativistic RPA or QRPA [17], the relativistic quasi-particle time-blocking approximation [18], and the algebraic Interacting Boson Model [19]. While the low-lying component of the E1 strength is observed in almost all calculations, the degree of collectivity is under debate. For further details on these theoretical models refer to [20] and to given references.

So far, the best description of the experimentally observed low-lying dipole strength in stable medium and heavy nuclei is achieved in calculations within the quasiparticle-phonon model (QPM). The first 1^- state, the position, the total strength and the fine structure of the PDR are described very well in the wide model space including up to three-phonon configurations. However, because of the lack of the self-consistency and the presence of the adjustable parameters, the application of this approach to nuclei with large neutron excess remains questionable. Another successful tool for investigating the low-energy dipole response are approaches based on the covariant energy density functional, first of all, the fully self-consistent relativistic quasiparticle random-phase approximation (RQRPA) [21]. The RQRPA supplemented with the coupling to low lying vibrations within the relativistic quasiparticle time blocking approximation (RQTBA) [18] in a fully consistent way enables one to reproduce the fragmentation of the giant dipole resonance as well as of the PDR and to describe the dipole strength of the low-energy part of the spectrum.

Fig. 1.4 shows the E1 strength distributions for the stable ^{116}Sn nucleus and

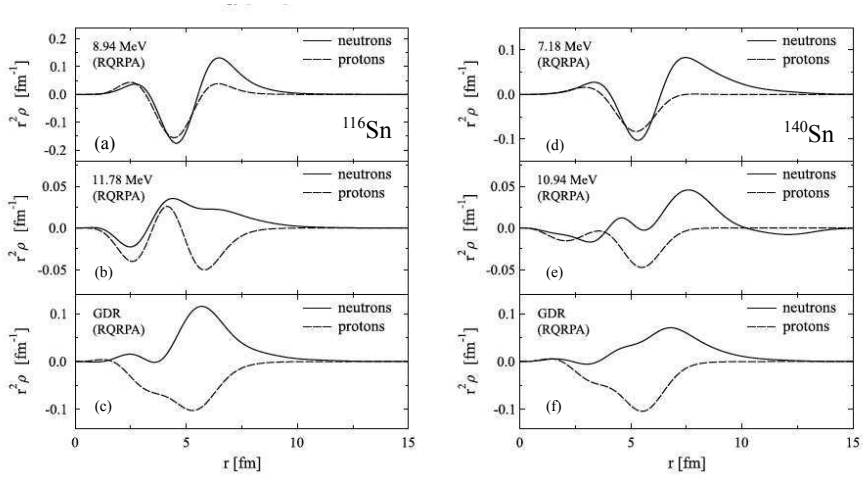

Figure 1.5: Proton e neutron transition densities corresponding to the most pronounced peaks at low excitation energies at 8.94 MeV and 11.78 MeV for ^{116}Sn (left) and 7.18 MeV and 10.94 MeV for ^{140}Sn (right), respectively [11, 22]. For comparison the transitional densities in the region of the GDR for both nuclei in the RQRPA calculation are also given, see panels (c) and (f).

very neutron rich ^{140}Sn calculated in RQTBA and RQRPA [11]. The low-lying E1 strength, that is present also in ^{116}Sn, is strongly enhanced and shifted to lower energies in the neutron rich ^{140}Sn. This qualitative observation about the separation of the PDR from the GDR in neutron-rich nuclei is confirmed by the analysis of the transition densities in the energy region around 10 MeV, see Fig. 1.5. The (a), (b) and (d), (e) panels of Fig. 1.5 exhibit the proton and neutron RQRPA transitional densities for the most pronounced peak of the PDR region (a-d panels) and the lowest peak of the GDR region (b-e panels) for ^{116}Sn and ^{140}Sn, respectively. For comparison the transitional densities in the region of the GDR for both nuclei in the RQRPA calculation are also given, see panels (c) and (f). As can be seen from Fig. 1.5(a) the neutron component, in ^{116}Sn, obviously dominate the transition density at the surface, however, with a noticeable proton mixture. In contrast, Fig. 1.5(d) implies that proton component is fully suppressed at the nuclear surface in the pygmy mode of ^{140}Sn, corresponding to the state at 7.18 MeV. Figs. 1.5(b) and 1.5(e) show that the structure of the RQRPA peaks changes drastically when the excitation energy increases and the lower part of the

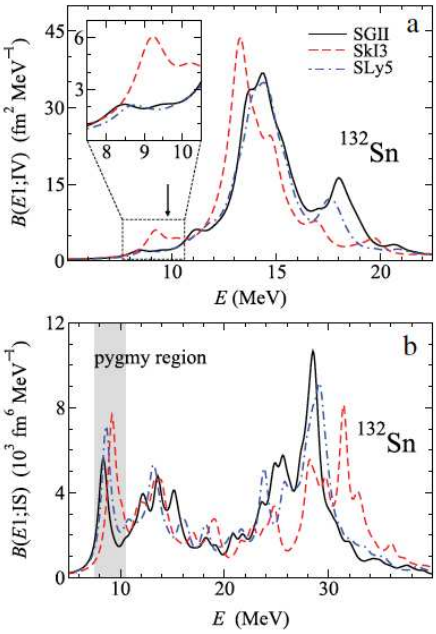

Figure 1.6: Strength function of the isovector (a) and isoscalar (b) responses of ^{132}Sn for different interaction [23].

GDR region is reached. Already the peaks at 11.78 MeV in ^{116}Sn and at 10.94 MeV in ^{140}Sn exhibit a completely different relative behaviour of the neutron and proton components. The two components are still in phase in the nuclear interior for ^{116}Sn, while they are not for ^{140}Sn. For ^{116}Sn, neutrons and protons are out of phase at the surface with protons even dominating; whereas in ^{140}Sn, protons do not contribute to the surface motion. Thus the (b) and (e) panels indicate that the states at these moderate excitation energies are no longer of pygmy type, but they also do not yet exhibit the typical GDR structure with protons and neutrons oscillating against each other, depicted in (c) and (f) panels. For more details see [11, 22].

Recently the isospin character of the low-energy dipole strength has been investigated in different calculations, partly stimulated by experiments on the PDR using isoscalar probes. Fig. 1.6 shows the isovector (IV) as well as the isoscalar (IS) E1 strength functions for RPA approach [23]. The PDR (assigned to the lowest

energy peak) is present in both the IS and IV strength function, which shows the mixed isospin nature of the PDR. Compared to the GDR the PDR is much more pronounced in the isoscalar channel. This calls for experimental investigations using complementary probes with different sensitivity to the isoscalar and isovector strength in order to verify this properties of the PDR. The experiment described in this thesis has this aim, a part from an investigation of the general properties of the PDR.

1.3.2 Experimental Investigations

The most widely used technique to study the PDR in stable nuclei is the Nuclear Resonance Fluorescence (NRF) [24]. This method has been used, from the very beginning, in systematic studies in different mass regions to investigate bound dipole excitations. The advantages of real photons as a probe are on the one hand the high selectivity to dipole-excited states, i.e. nearly exclusively $J = 1$ states are excited in an even-even nucleus. On the other hand the excitation mechanism is well known and includes exclusively the electromagnetic force. Therefore, intrinsic properties like spin, parity or transition strength can be extracted from the measured quantities (angular distribution, cross section etc.) in model independent way. In contrast to other particles used in scattering experiments photons are always fully absorbed in the excitation process. Consequently, to determine the excitation energy the photon energy has to be either known from the very beginning or has to be extracted from the spectroscopy of the decay products. In particular, since for high excitation energies photo-dissociation is the dominant reaction channel and neutron spectroscopy has no or very limited energy resolution in most cases, a knowledge of the energy of the incident photon is necessary.

To get a deeper insight into the structure of the excitations, the use of the hadronic interaction to populate the states of interest is a valuable complementary tool. One interesting approach is the inelastic scattering of α particles of about 30 MeV/u at forward angles. Due to their isoscalar internal structure α particles dominantly excite isoscalar states via the hadronic interaction from ground states. However, compared to the electromagnetic interaction, the hadronic interaction is much less selective. In contrast to real or virtual photons which favour $\Delta J = 1, 2$

excitations exhibiting strong electromagnetic transitions from the ground state, the hadronic interaction of α's or protons populates, depending on the kinematics, as well states with higher spins and show not trivial strength selectivity. These limitations could be overcome in experiments with γ-ray spectroscopy where, with a coincidence condition between the α's and γ's, low-spin states could be favoured. In addition the $\alpha - \gamma$ angular correlation could be analysed. The first experiment on ^{140}Ce [25] revealed an interesting result. By comparing this experiment with photon-scattering experiments, a clear selectivity in the population of the PDR states is observed. All E1 excitations below about 6.5 MeV detected in earlier photon scattering experiments are observed as well in the $(\alpha, \alpha'\gamma)$ experiment. However, in contrast all the E1 excitations above this energy are missing in the $(\alpha, \alpha'\gamma)$ spectra, see Fig. 1.7. To exclude that the ^{140}Ce is a special case the $(\alpha, \alpha'\gamma)$ studies were continued on the $N = 82$ isotone ^{138}Ba, the $Z = 50$ nucleus ^{124}Sn and the open-shell $N = 52$ nucleus ^{94}Mo. Whereas the fragmentation and the detailed structure of the E1 strength distribution observed in α-scattering experiments varies from nucleus to nucleus the overall excitation pattern is always quite similar. This different excitation pattern can only be explained by the different isospin nature of the two probes (isoscalar or isovector) or by their different interaction zones within the nucleus (whole nucleus or surface). Microscopic calculations show that this splitting reflects a different underlying structure of the PDR states: the low-energy states are of isoscalar nature and their transition density is peaked on the surface, while the high-energy states are of isovector nature and are associated to a transition towards the IVGDR [26]. To clarify the situation further experimental data using hadroic probes are obviously necessary.

Another new experimental approach to investigate the PDR using hadronc probes is the inelastic scattering of ^{17}O at bombarding energies of about 20 MeV/u [27]. This technique is the one used in the experiment described in this thesis. A first experiment has been performed at INFN-LNL using the AGATA demonstrator and large volume $LaBr_3$:Ce detectors for the γ-ray spectroscopy in coincidence with the detection of scattered ^{17}O ions. Preliminary results on ^{208}Pb indicate a similar behaviour as observed in the $(\alpha, \alpha'\gamma)$ experiments [27, 28]. The nuclei studied with this technique have been ^{208}Pb, ^{90}Zn, ^{140}Ce and ^{124}Sn. They have been chosen since they are all closed shell and consequently good candidate to investi-

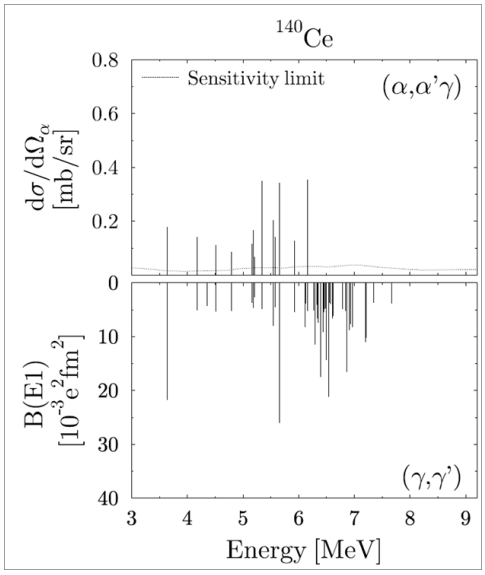

Figure 1.7: Comparison of cross section measured in the $(\alpha, \alpha'\gamma)$ experiments (upper part) with B(E1) strength derived from (γ, γ') experiments (lower part) for ^{140}Ce [29].

gate collective motions like PDR. In particular this thesis work it is concentrated on the study of the PDR in ^{124}Sn since it has been already investigated by (γ, γ') and $(\alpha, \alpha'\gamma)$ experiments. The combination of these different approaches promises a much more detailed understanding of the nature of the PDR in medium to heavy nuclei.

Chapter 2

Inelastic Scattering of Heavy Ions

Heavy ion reactions represent one of the most suitable instrument to investigate nuclear structure properties and nuclear reaction mechanisms. In the experiment described in this thesis, inelastic scattering of ^{17}O beam at the energy of 20 MeV/u in the laboratory frame was used to populate highly excited states in the target nuclei, including the pygmy dipole resonance. In Sec. 2.1 a short overview of a previous measurements employing the same technique will be given. In Sec. 2.2 the Distorted Wave Born Approximation (DWBA) will be presented, which can be used to give a simple but effective theoretical description of the inelastic scattering of heavy ions.

2.1 Giant Resonances via Inelastic Scattering

As discussed in Chap. 1 giant resonances have been studied over the years with several different probes. The use of heavy ions, compared to the others probes, can provide much larger cross-sections and a better peak-to-continuum ratio due to a decrease of knock-out reactions compare to protons [30]. When using heavy-ion scattering to study giant resonances, it has to be taken into account that angular distribution of the cross sections for the excitation of nuclear states are not very sensitive to the angular momentum transfer. This problem could be overcome by

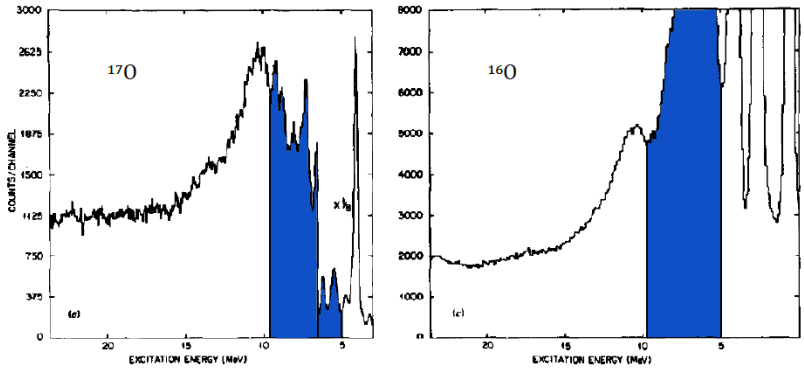

Figure 2.1: Inelastic scattering spectra for a ^{208}Pb target bombarded with an ^{17}O (left panel) and a ^{16}O (right panel) beam. The broad structure in the highlighted region of the ^{16}O spectrum is caused by projectile excitation and is completely removed with the ^{17}O beam because of its low neutron separation energy. Adapted from [30].

detecting the de-excitation γ-rays in coincident with the scattered ions, since photon selection rules are very sensitive to angular momentum. Moreover a proper choice of projectile is a crucial point in the study of GR via inelastic scattering of heavy ions. Indeed projectile excitation and nucleon pickup and subsequent nucleon decay could become a major source of background, forming broad structure superimposed on those caused by target excitation [30]. For these reasons the most suitable projectile for this type of experiment is the loosely bound ^{17}O ($S_n = 4.1$ MeV). In this way, if an excitation energy above S_n is transferred to the projectile, the neutron emission channel becomes dominant and the event could be easily removed from the inelastic scattering channel. The difference between the excitation spectra of a ^{208}Pb target, bombarded with an ^{17}O (left panel) or ^{16}O (right panel) beam is depicted in Fig. 2.1. As it can be clearly seen in the case of ^{16}O the region highlighted in blue is dominated by projectile excitation.

These spectra clearly demonstrate that care must be exercised in the choice of the heavy ion projectile used, and the energy of the ions should also be considered to ensure that the excitation energy region of interest is not compromised by projectile effects.

As mentioned in Sec. 1.3, an interesting feature in the region of the pygmy resonance has been observed in a number of different stable nuclei, by comparing results of photon-scattering and α-scattering experiments. The use of an additional probe as the inelastic scattering of ^{17}O at 20 MeV/u which has, similarly to alpha particles, a rather strong isoscalar character is expected to add valuable information on the quest of the nature of these low-lying E1 states.

These experimental technique has already been employed in the past in order to study the γ-decay of the ISGQR of ^{208}Pb [31] and the Coulomb excitation of the IVGDR [32].
The experiment described in thesis is the second of two experiments (for details on the first experiment see [28]). This experiment employs the same experimental technique described in [28] but can take advantage of improved experimental setup conditions. In particular, the γ-ray detection is performed with the AGATA Demonstrator, and by an array of 9 large volume $LaBr_3$:Ce scintillator detectors named HECTOR$^+$. The detection of the scattered ions is performed with two segmented Si telescopes, covering a large solide angle. For more details on the experimental setup see Chapter 3.

2.2 Distorted Wave Born Approximation

Inelastic scattering of heavy ions at intermediate energies ($10 - 100$ MeV/u) can be well described within the Distorted Wave Born Approximation (DWBA). The main features of the DWBA will now briefly be recalled, following references [33] [34].
The main assumption of all distorted wave theories is that elastic scattering and absorption are the most important mechanisms to occur when two nuclei collide. These phenomena can be described by the use of a complex optical potential. The elastic scattering is then described exactly (within the limitations of the optical model) and the other reaction channels are treated as a perturbations.

The collision between two nuclei can be seen as a wave process in which a plane wave (the projectile nucleus) hits an absorbing target nucleus creating a spherical

scattered wave. Consider the following binary reaction:

$$A + a \longrightarrow B + b \tag{2.1}$$

where a is an incoming beam ion, A is a target nucleus, and the reaction products are a beam-like ejectile b and target-like recoil B.
The system before the scattering occurs can be described by the following wave function in the center of mass frames of reference

$$\psi_i = N e^{i\vec{k}_\alpha \vec{r}_\alpha} \psi_a \psi_A \tag{2.2}$$

where ψ_a and ψ_A are the wave functions describing the internal degree of freedom of the two nuclei, while $\vec{r_\alpha}$ anf $\vec{k_\alpha}$ are respectively

$$\vec{r}_\alpha = \vec{r}_a - \vec{r}_A \tag{2.3}$$

$$\vec{k}_\alpha = \frac{m_a \vec{k}_a - m_A \vec{k}_A}{m_a + m_A} \tag{2.4}$$

It will be also convenient to introduce the reduced mass

$$\mu_\alpha = \frac{m_a m_A}{m_a + m_A} \tag{2.5}$$

After collisions the total wave function will have a scattered component for each possible reaction channel, that is

$$\psi_{tot} = N e^{i\vec{k}_\alpha \vec{r}_\alpha} \psi_a \psi_A + \sum_\beta \psi_{scatt,\beta} \tag{2.6}$$

The scattered wave function is spherical, and has the form

$$\psi_{scatt,\beta} = N f_\beta(\theta, \varphi) \frac{e^{i\vec{k}_\beta \vec{r}_\beta}}{r_\beta} \psi_b \psi_B \tag{2.7}$$

where the factor $f_b(\theta, \varphi)$ is called scattering amplitude and modulates the amplitude of the wave function as a function of the scattering angle and the bombarding energy, and ψ_b andψ_B are the wave functions describing the internal state of the reaction products.
Each nucleus moves away from the target with the relative velocity v_β therefore, since the wave functions describing the relative motion and the internal states are

normalized, the total particles emitted in a solid angle $d\Omega$ per unit time is just $v_\beta |N f_\beta(\theta,\varphi)|^2$. Dividing by the incident flux $v_\alpha |N|^2$, one obtains the differential cross section for the reaction channel β

$$\frac{d\sigma_\beta}{d\Omega} = \frac{v_\beta}{v_\alpha} |f_\beta(\theta,\varphi)|^2 \tag{2.8}$$

In order to give an expression for the scattering amplitude, one has to find a solution of the time independent Schrödinger equation of the form 2.6 and 2.7. For a single particle of mass m (with no internal degrees of freedom) which scatters from a fixed potential $U(\vec{r})$ such equation is

$$\left[-\frac{\hbar^2}{2m} \bigtriangledown^2 + U(\vec{r}) \right] \chi(\vec{r}) = \Sigma \chi(\vec{r}) \tag{2.9}$$

where Σ is the total energy of the particle. Since $U(\vec{r})$ may excite one or both the nuclei involved in the reaction, one has also to consider the nuclear internal states. The internal wave function ψ_a and ψ_A are solution of the Schrödinger equations

$$H_a \psi_a = \epsilon_a \psi_a \qquad H_A \psi_A = \epsilon_A \psi_A \tag{2.10}$$

where H_a and H_A contain a kinetic term and an interaction term. Adding, in the center of mass frame of reference, the Hamiltonian of the relative motion to those concerning the internal states, one gets the final Schrödinger equation to be solved

$$\left(H_a + H_A - \frac{\hbar^2}{2\mu_\alpha} \bigtriangledown_\alpha^2 + U_\alpha(\vec{r}) \right) \psi_{tot} = E \psi_{tot} \tag{2.11}$$

where E is the total energy of the system.
The general solution of Eq. 2.11 has the form

$$\psi_{tot} = \sum_{b,B} \chi_{b,B}(\vec{r}_\alpha) \psi_b \psi_B \tag{2.12}$$

Concentrating upon the relative motion, ignoring the internal degree of freedom, one can find an integral solution of Eq. 2.9 which allows to determine the scattering amplitude.
A more detailed description should include also the internal states and therefore

wave functions of the form 2.12. The general solution of Eq. 2.9 is given by the incident plane wave plus the scattered wave and it can be written as

$$\chi(\vec{k},\vec{r}) = e^{i\vec{k}\vec{r}} - \frac{1}{4\pi}\int \frac{e^{i\vec{k}|\vec{r}-\vec{r'}|}}{|\vec{r}-\vec{r'}|} U(\vec{r'})\chi(\vec{k},\vec{r'})d\vec{r'} \tag{2.13}$$

Evaluating the previous equation at large $|\vec{r'}|$ one obtains

$$\chi(\vec{k},\vec{r}) = e^{i\vec{k}\vec{r}} - \frac{e^{i\vec{k}\vec{r}}}{4\pi r}\int e^{i\vec{k'}\vec{r'}} U(\vec{r'})\chi(\vec{k},\vec{r'})d\vec{r'} \tag{2.14}$$

By comparison with 2.7 one can determine the scattering amplitude

$$f_\beta(\theta,\varphi) = -\frac{1}{4\pi}\int e^{i\vec{k'}\vec{r'}} U(\vec{r'})\chi(\vec{k},\vec{r'})d\vec{r'} \tag{2.15}$$

Of course, this is only a formal solution since it contains the unknown wave function $\chi(\vec{k},\vec{r'})$. Some approximations are necessary in order to solve the equation. In the DWBA approach, it is assumed that the potential U can be written as $U = U_1 + U_2$ and that the exact solution $\chi_1(\vec{k},\vec{r'})$ of Eq. 2.9 for U_1 is known. Typically U_1 is the optical potential which causes the elastic scattering, while U_2 is the potential that induces non-elastic transitions, and can be treated as a perturbation.

One can distinguish two types of solutions given by a plane wave plus a scattered wave in the exit channel $\chi_1^{(+)}(\vec{k},\vec{r})$ and a plane wave plus a scattered wave in the entrance channel $\chi_1^{(-)}(\vec{k},\vec{r})$. The two solutions are one the timing inverse of the other

$$\chi_1^{(-)}(\vec{k},\vec{r}) = \chi_1^{(+)}(-\vec{k},\vec{r})^* \tag{2.16}$$

The two waves are called distorted waves. One can rewrite Eq. 2.14 by replacing the plane waves with such distorted waves

$$\chi(\vec{k},\vec{r}) \longrightarrow \chi_1^{(+)}(\vec{k},\vec{r}) - \frac{e^{i\vec{k}\vec{r}}}{4\pi r}\int \chi_1^{(-)}(\vec{k'},\vec{r'})^* U_2(\vec{r'})\chi(\vec{k},\vec{r'})d\vec{r'} \tag{2.17}$$

The full scattering amplitude is the sum of a contribution given by U_1, and a term concerning U_2. Furthermore, if U_2 is weak compared to U_1 one can approximate $\chi(\vec{k},\vec{r'})$ with the solution $\chi_1^{(+)}(\vec{k},\vec{r})$ for U_1. The corresponding amplitude

is

$$f_{DWBA}(\theta,\varphi) = f_1(\theta,\varphi) - \frac{1}{4\pi}\int \chi_1^{(-)}(\vec{k'},\vec{r'})^* U_2(\vec{r'})\chi_1^{(+)}(\vec{k},\vec{r'})d\vec{r'} \tag{2.18}$$

The generalized expression for the DWBA transition amplitude for a reaction $A(a,b)B$ is given by

$$f_{DWBA}(\theta,\varphi) = -\frac{1}{4\pi}\int\int \chi_\beta(\vec{k}_\beta,\vec{r}_\beta)^* \langle b,B|U_2|a,A\rangle \chi_\alpha(\vec{k}_\alpha,\vec{r}_\alpha)d\vec{r}_\alpha d\vec{r}_\beta \tag{2.19}$$

where χ_α and χ_β are the generalization of χ_1 describing the elastic scattering in the entrance and exit channel respectively, while the matrix element $\langle b,B|U_2|a,A\rangle$ takes into account the non elastic channels, considering also the internal structure of the nuclei participating in the collision.

2.2.1 Nuclear Potential

The nuclear potentials discussed in the previous section are central potentials representing the interaction between two nuclei when they collide. Such potentials are made by the sum of the long range Coulomb potential, due to the presence of protons, and a short range potential due to the nuclear force. The nuclear potential depends on the nucleon-nucleon interaction which can be parametrized by several models. In a heavy ions reaction the nuclear potential is given by the integral over all the interactions between nucleons present both in the projectile nucleus and in the target nucleus. It can be written as:

$$U(\vec{R}) = \int\int \rho_p(\vec{r}_p)\rho_t(\vec{r}_t)v(\vec{r}_{tr})d^3r_p d^3r_t \tag{2.20}$$

where $\rho_p(\vec{r}_p)$ and $\rho_t(\vec{r}_t)$ represent the projectile nucleon density in the point $\vec{r}_p$ and the target nucleon density in the point $\vec{r}_t$, and $v(\vec{r}_{tr})$ is the nucleon-nucleon interaction, with $\vec{r}_{tr} = \vec{r}_t - \vec{r}_r$, as shown in Fig.

Typically, $U(\vec{R})$ has a Woods-Saxon form whose depth (around -50 MeV for a single nucleon potential) depends on the number of nucleons and on the model used to describe the nucleon-nucleon interaction. The potential has a real part, that describes the elastic scattering process, as well as an imaginary part:

$$U(R) = V(R) + iW(R) \tag{2.21}$$

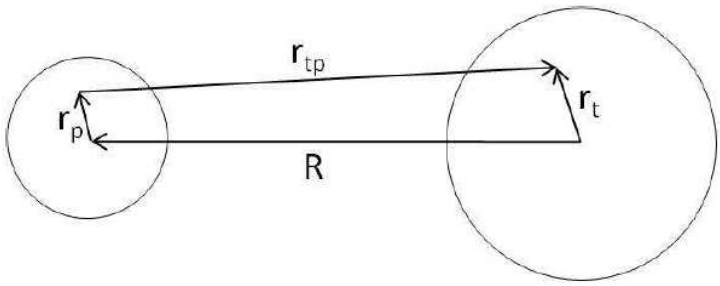

Figure 2.2: Coordinates of the integral Eq. 2.20.

where $V(R)$ is a Wood-Saxon potential with depth V, radius $R_v = r_{v0}A^{1/3}$ and a diffusiveness a_v, and $W(R)$ is the imaginary component of the potential, with depth W (typically a fraction of V), radius $R_w = r_{w0}A^{1/3}$ and a diffusiveness a_w:

$$V(R) = \frac{V}{1 + e^{\frac{R - R_v}{a_v}}} \qquad W(R) = \frac{W}{1 + e^{\frac{R - R_w}{a_w}}} \tag{2.22}$$

The imaginary part of the potential accounts for the absorption of the incident wave caused by non-elastic processes: in a heavy ion reaction there are many open channels, and if an internal excitation or a particle transfer occurs, the system does not return to the entrance channel and the projectile is absorbed. This optical potential accounts for the dominant part of the interaction between the two nuclei, and corresponds to the U_1 term in the discussion above. In order to calculate the reaction cross section for an inelastic scattering process, however, it is also necessary to describe the residual interaction that corresponds to the U_2 term in the discussion above.

All DWBA calculations for our experiment were carried out with the FRESCO code [35], which calculates virtually any nuclear reaction which can be expressed in a coupled-channel form. It can perform calculations for both heavy ion reactions and light ions reactions, providing particle angular distributions for all the reaction channels. The basic ingredient for the elastic calculations are the two-body wave function and the optical potential, which describes the nuclear interaction between projectile and target nuclei. The effective interaction is given by the sum

Optical potential parameters used in [36]

Nucleus	V	R_0	a_v	W	R_{w0}	a_w
^{90}Zn	40	1.15	0.671	26	1.15	0.671
^{208}Pb	60	1.17	0.665	38	1.17	0.665

Table 2.1: Optical potential parameters used in [36].

of Coulomb potential and nuclear optical potential. In the case of inelastic excitations, the FRESCO computer code uses a collective model for the nuclear part of the effective interaction. The deformation of the excited level is also required. In the present work, the deformation of the excited states of ^{124}Sn have been calculated using the tabulated experimental values of $B(E, 0 \longrightarrow k)$, which is connected to the deformation (β) by the reduced deformation length ($RDEF(k)$):

$$RDEF(k, I \longrightarrow I') = \sqrt{B(E, 0 \longrightarrow k)} * \frac{4\pi}{3ZR^{k-1}} \tag{2.23}$$

where $R = 1.2A^{1/3}$.
For more details on the inputs of the FRESCO code used for our calculations see Appendix C.

The present model has been already tested in the case of inelastic scattering of ^{16}O on ^{208}Pb and ^{90}Zn, [36]. The code used in this analysis was the PTOLEMY code. Fig. 2.3 and Fig. 2.4 show the experimental inelastic scattering angular distributions and the results of the DWBA calculations for ^{208}Pb and ^{90}Zn, respectively. As can be observed from these figures there is a reasonable agreement between the experimental and calculated angular distributions for the excited states considered. In this analysis the optical model parameters were obtained by setting the real well depth (V) to a fixed value and allowing the imaginary well depth (W) to vary along with the radius (r_0) and a diffuseness (a) parameters. The real and imaginary radius and diffuseness parameters were set to be equal. The Coulomb radius parameters was 1.2 fm. The optical model parameters are reported in Table 2.1.

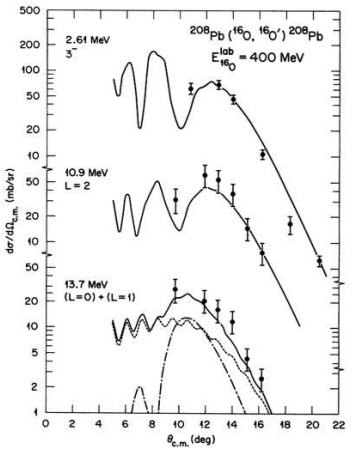

Figure 2.3: Measured and calculated angular distributions for indicated states in ^{208}Pb, [36].

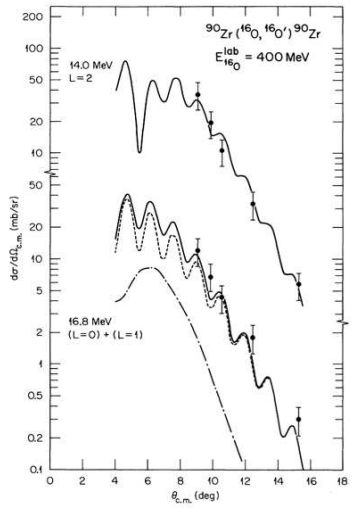

Figure 2.4: Measured and calculated angular distributions for indicated states in ^{90}Zn, [36].

Chapter 3

Experimental Set-Up

The experiment described in this thesis was performed in December 2011, at the Legnaro National Laboratories (LNL), in Italy.
The Giant Resonance modes have been excited by inelastic scattering of ^{17}O ions at 20 MeV/u, in the laboratory frame, on a ^{124}Sn target (3 mg/cm^2 thick, enriched to 99%). ^{17}O has been chosen since it is loosely bound (4.1 MeV), and thus it allows to have a γ-spectrum mainly containing target de-excitation, particularly in the region of interest E$^* > 4.5$ MeV.
The beam was provided by the PIAVE-ALPI accelerator system, with an average current of 0.5 pnA. PIAVE is a superconducting radio-frequency quadrupole, and was used as an injector for the superconducting linear accelerator ALPI.
The detection of the scattered ions was performed with two ΔE-E Silicon Telescopes mounted inside the scattering chamber. The detectors used in this experiment are the prototypes for the TRacking Array for light Charged particle Ejectile (TRACE) [37], a 4π array of segmented ΔE-E silicon telescopes, designed for the detection of protons and alpha particles in experiment with fusion-evaporation and direct reactions. A more detailed description of this array is done in sec. 3.1.
The γ-rays produced during the de-excitation of the reaction participants have been measured using an array of HPGe segmented detectors (the AGATA Demonstrator [38], see sec. 3.2) coupled to an array of 9 large volume $LaBr_3$:Ce scintillators, (the HECTOR$^+$ array [39], see sec. 3.3) used to increase the detection efficiency for high energy γ-rays.

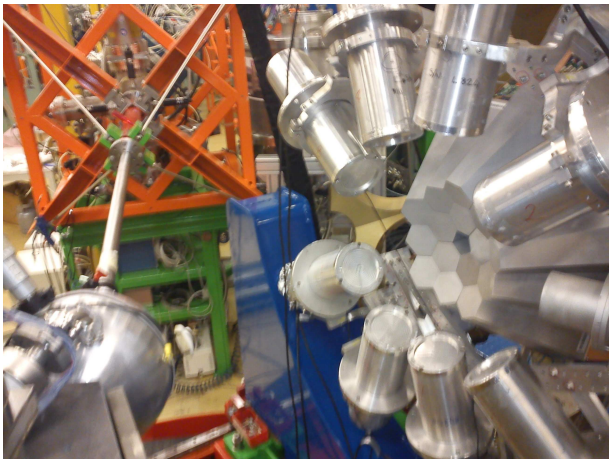

Figure 3.1: Picture of the experimental setup, comprising five triple clusters of AGATA (in the back of the picture) and an array of 9 $LaBr_3$:Ce detectors named HECTOR$^+$.

A picture of the experimental set-up is shown in Fig. 3.1; the AGATA Demonstrator detectors are in the middle, while the detectors around them are the $LaBr_3$:Ce scintillators of the HECTOR$^+$ array.
A schematic view of the complete experimental set-up is shown in Fig. 3.2. Two Data AcQuisition (DAQ) systems, described in sec. 3.4, were running in parallel during the experiment: one for the AGATA Demonstator, based on NARVAL [40], and one for ancillary detectors, based on KMAX [41]. The trigger conditions are described in sec. 3.5.

3.1 The Silicon Telescopes

The detection of the scattered ^{17}O ions was performed with two segmented ΔE-E silicon telescopes. The ΔE detectors were 200 μm thick, corresponding to an energy loss of about 70 MeV for an ^{17}O ion of 340 MeV (20 MeV/u). The E detectors were 1 mm thick, enough to stop the ^{17}O ions completely.
Each detector is segmented in 60 pads of 4 x 4 mm^2, for an active area of 20 x 48 mm^2. The large active area allows for a good solid angle coverage, and the segmentation for a higher counting rate limit. Furthermore, the detectors have for

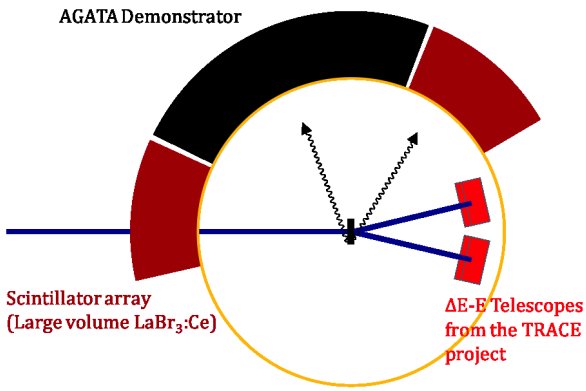

Figure 3.2: Schematic view of the experimental setup, comprising five triple clusters of AGATA, an array of 9 $LaBr_3$:Ce detectors named HECTOR$^+$ and two E-ΔE Silicon telescope of the TRACE projects.

each pad a much better energy resolution compared to a non-segmented Silicon detector of the same total area: the electrical noise of a solid-state detector is proportional to its capacity, which is in turn proportional to the detector surface area for a planar geometry.

The detectors were mounted inside the scattering chamber at ~ 7 cm from the target, covering a solid angle of ~ 100 msr per telescopes and an angular range of $\sim 25°$. An ad-hoc adapter board was built, which selects the 32 pads closest to the beam direction and connects them to the charge pre-amplifiers and to the rest of the electronics: in this way, we reduced by a factor of 2 the number of electronics channels needed, without losing efficiency in the region of interest. Each detector was connected to a custom 32-channels charge preamplifier. The preamplifiers were mounted as close to the detectors as possible. The preamplifiers were placed on a metallic board to favour heat dispersion. The preamplifiers were under vacuum, and were connected through high-density cables to a flange and from the flange to an active circuit splitting the signals of each into 2 standard flat cables. Each of these cables was the input of a CAEN N1568 16-channel spectroscopic amplifier, set with a shaping time of 2 μs. The output of the amplifiers was then sent to the CAEN V879 ADCs (Analog to Digital Converters) for data acquisition. Each amplifier channel also had a built-in CFD (Constant Fraction Discriminator), that was sent to the CAEN V878 TDCs (Time to Digital Converters). Finally, the

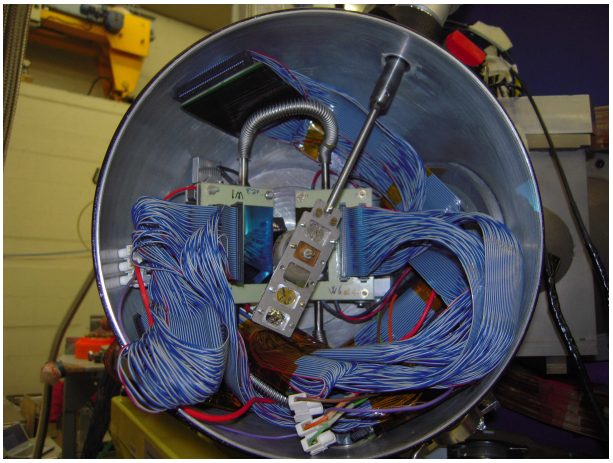

Figure 3.3: Picture of the Silicon telescopes pixels of the TRACE project type inside the scattering chamber.

amplifiers also have a "OR" output that is the logical "OR" of all the 16 CFD channels, and is used to build the trigger condition (see section 3.5).
The detectors were mounted on a mechanical support that allowed to change angular position of both telescopes with respect to the beam direction. For our experiment the detectors were placed at an angle of $\sim 9°$measured in the centre of the first column of pads. The distance between the target centre and the ΔE detectors was ~ 7 cm. The detectors can be seen mounted in the scattering chamber in Fig. 3.3.
Two Peltier cells were placed behind each of the telescopes in order to cool them to a temperature of about $-25°$. In order to guarantee a good heat transfer, the detectors were mounted in aluminium oxide PCBs (Printed Circuit Boards) and brass dices were used to fix the ΔE detector to the E detector. The hot side of the Peltier cells was in turn cooled by a refrigerant liquid kept at $\sim 10°$by a chiller system.

3.2 The AGATA Demonstrator

AGATA (Advanced Gamma Tracking Array) is a European project aiming at the development and construction of a 4π array for nuclear spectroscopy studies. This

kind of detectors is based on γ-ray tracking, whose principle is the reconstruction of the sequence of interactions of each γ-ray inside the array, in order to achieve a good suppression of the Compton background. As a consequence high efficiency is achieved, overcoming the limits of Compton-suppressed HPGe arrays.
In the actual phase AGATA is composed by 5 triple and 5 double-clusters of HPGe segmented detectors, this configuration was named AGATA Demonstrator. The Demonstrator has started its campaign in 2009, when test experiments were done in order to evaluate the performances of the tracking algorithms in terms of energy resolution, efficiency and Peak-to-Total (P/T) ratio. The physical campaign, instead, has begun in February 2010, when the first in-beam measurement took place; at that moment only 3 triple-clusters were available. At the time of our experiment two triple-cluster was added to the existing set-up, resulting in 5 triple-clusters for a total of 15 HPGe detectors.

3.2.1 AGATA: Advanced GAmma Tracking Array

The aim of the Advanced GAmma Tracking Array (AGATA) project [38] is the construction of an array based on the novel concepts of pulse shape analysis and γ-ray tracking with highly segmented Ge semiconductor detectors.
The best geometrical design has been deeply investigated, as described in [42]; here only the main ideas and principles are summarized.
The first need was to have the best detection efficiency and solid angle coverage; an additional requirement in the conceptual design of AGATA was to keep a sufficiently large inner space inside the array in order to host ancillary instrumentation, which often is indispensable in the physics programme of AGATA. GEANT4 simulations [42] were used to decide the best performing configuration based on geodesic tiling of a sphere with 12 regular pentagons and 180 hexagons. Owing to the symmetries of this specific buckyball construction, three slightly different irregular hexagons are needed (see Fig. 3.4); the three shapes are indicated by the colours red, green, and blue. The detectors are grouped in 60 identical triple-clusters, each containing a red, a green, and a blue crystal (see Fig. 3.5); the pentagonal detectors are individually canned. The three detectors are placed inside a single cryostat and are cooled to 90 °K with a liquid nitrogen system. The preamplifiers for all segments and core signals are also cooled to 130 °K.

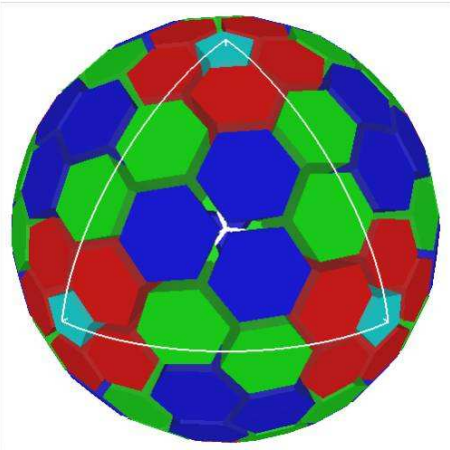

Figure 3.4: Schematic view of the full AGATA detector; the different colours represent the different shapes of the detectors [38].

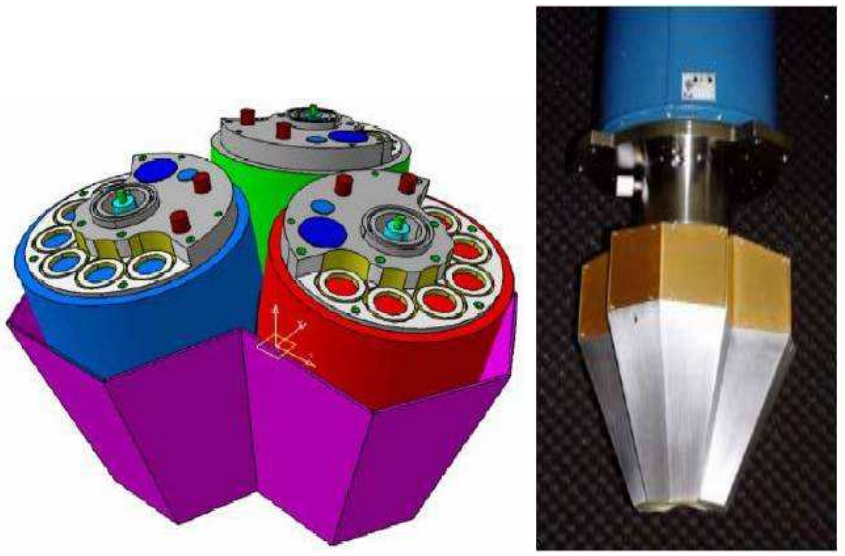

Figure 3.5: The AGATA triple-cluster: Technical drawing on the left and picture of a real cluster on the right

The inner radius of the array is 23.5 cm. The total solid angle covered by HPGe material is close to 80% and the photo peak efficiency is as high as 50% for individual 1 MeV γ-rays. A key feature of AGATA is the capability to determine the emission direction of the detected γ-rays with a precision of $\sim 1°$. This corresponds to an effective solid angle granularity of $5 \cdot 10^4$ (unachievable with individual germanium crystals) and ensures an energy resolution better than 0.5% for transitions emitted by nuclei recoiling at velocities as high as 50% of the speed of light. This value is only a factor of two bigger than the intrinsic resolution of HPGe detectors and is comparable with the values currently observed at 10 times smaller recoil velocity.

3.2.2 High-Fold Segmented Detectors

In order to achieve a large tracking efficiency (see Section 3.2.5), the positions where the γ-rays interact inside the detector volume should be determined with an accuracy of ~ 5 mm at an energy of 1 MeV. This corresponds to an effective granularity of approximately 30000 voxels (the analogous of pixel in 3D) per Ge detector. While it is impossible to achieve such a granularity by a physical segmentation of the crystal, pulse-shape analysis methods (PSA) (see Section 3.2.4) can provide this position accuracy; a medium level segmentation of the outer detector contact is however required: each detector is then divided into 20 - 40 segments. The AGATA array is composed by large volume 36-fold segmented n-type germanium detectors in the semi-coaxial geometry, like the one depicted in Fig. 3.6. The detectors are produced by the French company Camberra and have a length of 90 mm, a diameter of 80 mm at the rear, and a tapering to a irregular hexagonal shape with an angle of 10° at the front. The sector-wise segmentation goes through the middle of each hexagonal side, the longitudinal segmentation forms rings of varying thickness, optimised for a uniform distribution of the γ-ray interactions. Because of their complexity and the need of packing them very close to each other, these detectors use the encapsulation technology developed for the clusters of the EUROBALL array.

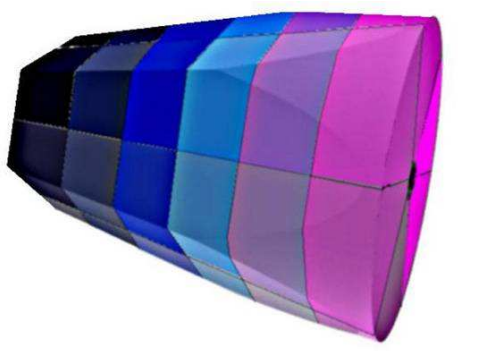

Figure 3.6: Schematic view of the 36-fold segmented, hexaconically tapered germanium crystal, of the AGATA Demonstrator.

3.2.3 Digital Electronics

The use of Pulse Shape Analysis (PSA) techniques obviously requires that the shape of each pulse in the detector is recorded and processed digitally. For this reason, all 37 signals (36 segments + the central electrode) from each detector are digitised at 100 MHz immediately after the preamplifiers by high-resolution (14 bits) fast ADCs. Using the digitized signals the energy, time and position of each γ-ray interaction are then extracted using digital processing techniques. These data are associated with unique time-stamp and unique positional label which will be used by the data acquisition processors to associate data produced by the same event.

Digital processing allows to use filters that have no analogue counterpart such as the Moving Window Deconvolution algorithm [43] to reconstruct the original charge collection by removing the effect of the preamplifier response. A good energy resolution can be achieved with shorter shaping time; in this way the array is able to sustain a counting rate per detector 5 times higher than the "traditional" apparatus (50 kHz per detector instead of 10 kHz).

3.2.4 Pulse Shape Analysis

The task of Pulse Shape Analysis (PSA) is to identify with high precision the location of the individual interaction points and the corresponding energy deposits of a γ-ray. There can be more than one interaction in one detector segment and/or the

γ-ray can be scattered to another segment of the same crystal or to an adjacent detector or even across the array. Simulations show that in order to reach a satisfactory efficiency, tracking algorithms have to be provided with information on the gamma interaction localization with a precision of at least 5 mm.

The parameters of interest (i.e. three dimensional interaction position, energy, time and a confidence in the quality of the determined fit) are determined by comparing the detector pulse shapes to a calculated reference basis, where each signal corresponds to a well-localised single interaction point.

The input data for the PSA process for an AGATA detector consist in 37 signals $S_j(E,t)$, with $j = 0, 1, ..., 36$, sampled at the output of the HPGe detector preamplifiers (36 segments + core). Since the detector response is linear, $S_j(E,t)$ can be written as the superposition of the signals associated to the single hits of the gamma $S_j(x_i, y_i, z_i, t)$ weighted by their energy release E_i:

$$S_j(E,t) = \sum_{i=1}^{N} E_i S_j(x_i, y_i, z_i, t) \tag{3.1}$$

where N is the number of interactions inside the segment and $E = \sum_{i=1}^{N} E_i$.
In the case where $N = 1$, Eq. 3.1 reduces to

$$S_j(E,t) = E S_j(x_i, y_i, z_i, t) \tag{3.2}$$

Solving this equation means finding the interaction point that better reproduces the measured signal shape, by a comparison between the measured signal shape and the set of shapes belonging to the signal basis. In order to achieve a good position resolution, it is not sufficient to compare the net-charge signal of a segment with the basis, but the transient shapes in the neighbouring segments must also be compared to a basis for transient signals. If $N>1$, there is the added complication of disentangling the single interactions of each segment, all with an unknown energy deposit and unknown position.

The comparison of waveforms is a very challenging task if performed in a naive way, more so if a decomposition of each signal shape in multiple interaction points is needed, because it requires a large quantity of memory and of CPU time; fast and efficient PSA algorithms are therefore needed. Many approaches to the "PSA problem" have been proposed: adaptive grid search [44], neural networks, matrix inversion [45], genetic algorithms [46], recursive subtraction [47], etc.

In the experiment presented in this thesis, as in the whole LNL experimental campaign, it has been decided to use a grid search algorithm because it is the only one with processing times small enough to be used in on-line acquisition. A basic assumption for this algorithm is that the size of a segment is small enough that multiple interactions inside the same segments can be neglected, so that the PSA is performed under the simpler case of Eq. 3.2, i.e. $N = 1$. While it is known that it is not a very realistic approximation, the effect on the overall performance of the detector has been found negligible [44].

Independently of the chosen algorithm, the quality of the PSA also depends critically on the signal basis that is used for the decomposition of the measured shapes. There is a large effort in the AGATA community to build an experimental signal basis [48, 49], but it is not yet available due to the long times needed to build up the necessary statistics while achieving a good precision on the reference positions. The basis used at the moment is obtained via detailed calculations of the charge transport through the detector [50], [51].

The reconstruction of the signal shape performed by PSA algorithms can also be used to increase the time resolution of a HPGe detector, compared with that obtained with a common approach based on a constant fraction discriminator. While such possibilities are under study [52], they were not employed for the present analysis.

Once the interaction points, with the corresponding energy and time, have been determined, the events have to be reassembled according to their timestamps and a tracking algorithm (see Section 3.2.5) is applied in order to disentangle the coincident interaction points and to determine the total energy and the emission direction of those γ-rays that have been fully absorbed in the germanium array. Absolute positions of the individual crystals and target position corrections enter at this stage.

3.2.5 Gamma-ray Tracking

The aim of tracking algorithms is to reconstruct the trajectories of the incident photons in order to determine their energy and direction. To do this, the algorithms must disentangle the interaction points identified in the detectors and establish the proper sequences of interaction points. Tracking algorithms can be divided into two

classes: algorithms based on back tracking [53] and algorithms based on clustering and forward tracking [54]. Both are related to the particular properties of the interaction of photons with matter.

Back tracking The back tracking algorithm [53] is based on the fact that the photoelectric energy deposition is almost independent from the incident photon energy and is peaked around $100 - 250$ keV; it assumes that the interaction points within a given deposited energy interval $e_{min} \leq e_i \leq e_{max}$ are the last interaction (in time) of a fully absorbed γ-ray; the algorithm then finds the closest interaction to the photoelectric one, it computes the scattering angle using the incident and the scattered energies and, finally, it searches for the other previous interactions along this direction; such process is iterated until the direction points directly to the target. This algorithm, however, was found to be less efficient and showed a worse P/T in the reconstructed spectra [55], and was therefore not used for our analysis.

Forward tracking In the forward tracking algorithm the first step is the identification of clusters of interaction points that may belong to a single γ-ray. Looking at the forward peaking of Compton scattering cross-section, clusters are identified as a set of interaction points with an angular distance $\leq \theta_0$ between each other (link algorithm) or with respect to a given point (leader algorithm).
Secondly, each cluster is evaluated to determine whether it contains all the interaction points belonging to a single γ-ray with the following criteria:

1. If the interaction points satisfy the Compton scattering formula, the tracking algorithm uses the angle-energy relation of Compton scattering to determine the most likely scattering sequence from the position and energy of the interaction points:
$$\chi^2 = \sum_{j=1}^{N-1} W_j \left(\frac{E_{\gamma'} - E_{\gamma'}^{pos}}{E_\gamma} \right)_j^2 \tag{3.3}$$
where E_γ is the sum of the deposits from 1 to $N-1$, and $E_{\gamma'}^{pos}$ is the energy of the scattered photons according to the Compton scattering formula. For a cluster of N interaction points, the $N!$ permutations are tested, and the cluster is defined as "good" if the χ^2 is below a predetermined threshold.

2. If the cluster is composed by a single interaction point and the energy satisfy photoelectric conditions, the algorithm checks the compatibility between γ-ray energy and interaction depth in the detector. If the compatibility is reached, a Monte Carlo-like approach is taken to decide if to consider the interaction point as an actual photoelectric event or if to discard it as an isolated Compton scattering event.

3. If there are two γ-rays of energy equal to 511 keV and an interaction point in the middle with energy greater than 1022 keV, that is a pair production event, the three energies are summed and considered as a single γ-ray.

The algorithm tries to recover some of the wrongly identified clusters. For example, one type of incorrectly identified cluster comes from a single γ-ray being separated into two clusters. This γ-ray can be correctly identified by tracking together all pairs of bad clusters. When the result gives a small χ^2, the γ-ray is recovered by adding the two clusters. The clusters which do not satisfy any of the above criteria are rejected, thus improving the P/T (peak to total) ratio of the spectra without the need for Compton suppression shields. If a large solid angle is covered with segmented germanium detectors, the combination of PSA and γ-ray tracking allows for a very high photopeak efficiency together with a good P/T ratio. An example of the interaction clustering is represented in Fig. 3.7, where a high-multiplicity event is considered: the coloured dots represent single interaction points of γ-rays inside a 4π detector shell; the red circles correspond to clusters of interaction points identified by the tracking as belonging to a single γ-ray, while the green squares correspond to clusters that are discarded.

The forward tracking algorithm is the basis for the Orsay Forward Tracking (OFT) code [55] and the Mars Gamma-ray Tracking (MGT) code [56], that are implemented in the Narval code for the experimental data; the last one is also used for GEANT4 simulations.

3.2.6 The Demonstrator Phase of AGATA at LNL

It has been planned by the international collaboration that the development of AGATA will proceed in stages, with the construction of the full array preceded by an R&D phase aimed at building a subsystem of 5 triple clusters, called AGATA

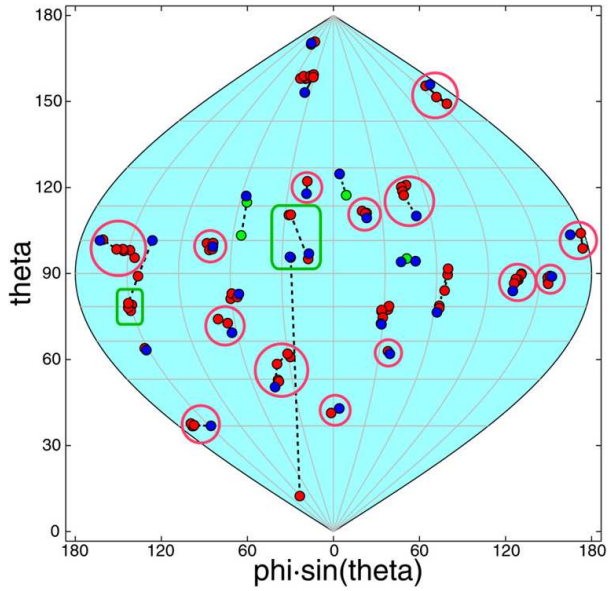

Figure 3.7: "World map" representation of $M_\gamma = 30$ events of $E_\gamma = 1.0$ MeV detected in an ideal 4π HPGe shell and reconstructed with the tracking algorithm. Correctly reconstructed transitions are grouped with red circles while green rectangles represent badly reconstructed background events.

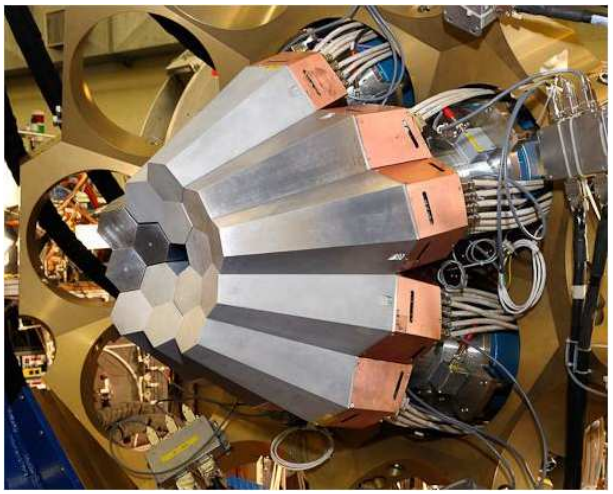

Figure 3.8: Photo of the AGATA Demonstrator installed at Legnaro National Laboratories.

Demonstrator array. The Demonstrator, together with its digital electronics, DAQ, has been installed at LNL in 2008 and operated in various physics experiments from February 2010 to December 2011. The aim of the experimental campaign of the Demonstrator is to confirm the performances of the γ-ray tracking algorithms in real measurement. A picture of the full Demonstrator is shown in Fig. 3.8. In a "conventional" array of germanium detectors, a collimator is placed in front of each detector in order to minimize the scattering of photons between different crystals, therefore, only a small region around the target position is actually visible from the detectors. In the case of the AGATA Demonstrator array, no collimators are present, and thus it is possible to modify the placement of the detectors relative to the target position depending on the specific measurement. In particular, given the limited solid angle coverage, it is feasible to place the detectors closer to the target position compared to the "reference" 23.5 cm distance of the full AGATA array in order to cover a larger solid angle. The simulated photo-peak efficiency and P/T ratio as a function of the shift towards the geometrical centre are shown in Fig. 3.9 for monochromatic 1 MeV γ-rays.

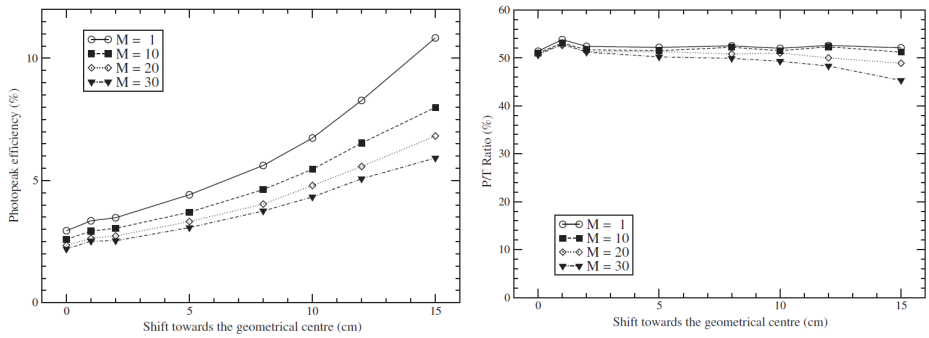

Figure 3.9: Photo-peak efficiency (left) and peak-to-total ratio (right) of the AGATA Demonstrator array for 1 MeV photons emitted from a point source at rest [42].

3.2.7 Energy Resolution

The energy resolution is one of the main parameters characterizing the performances of an HPGe detector array. The response of AGATA segmented HPGe detectors to γ-rays was measured in the energy range 2-9 MeV. The γ-rays between 2 and 9 MeV were produced using an Am-Be-Fe radioactive source, see [57]. This source is composed by a core of ^{9}Be and alpha-unstable ^{241}Am and it was placed into a 3 x 3 cm hole drilled in a iron slab of 7 x 7 x 20 cm and surrounded by a paraffin wax in a 20 x 20 cm cylindrical shape. When an alpha particle is emitted by the ^{241}Am, there is a high probability that it is captured by a ^{9}Be, making a $^{9}Be(\alpha, n)^{12}C$ reaction. The neutron are emitted with energies between 400 keV and 5 MeV and are thermalized by the multiple scattering in the paraffin layer, which serves both as moderator and as a shielding. The slow neutrons are then captured by the iron isotopes. Note that the $^{9}Be(\alpha, n)^{12}C$ reaction can also populate the ^{12}C in its first excited state, at 4.4 MeV; the gamma decay from the level is Doppler broadened because of the ^{12}C has a v/c of 10 %. The Am-Be-Fe source is very useful because the $^{54}Fe(n, \gamma)^{55}Fe$ reaction produces γ-rays up to 9 MeV. This is one of the few ways to have such high-energy γ-rays without using an accelerator. The relative energy resolution (i.e. $\frac{FWHM}{E_\gamma}$) has been measured as a function of the γ-ray energy. As can be seen from Fig. 3.10 the experimental data follow the expected $\frac{1}{\sqrt{E}}$ trend (indicated by the dashed line). The empty black circles represent the data associated to the single crystal; instead, the black trian-

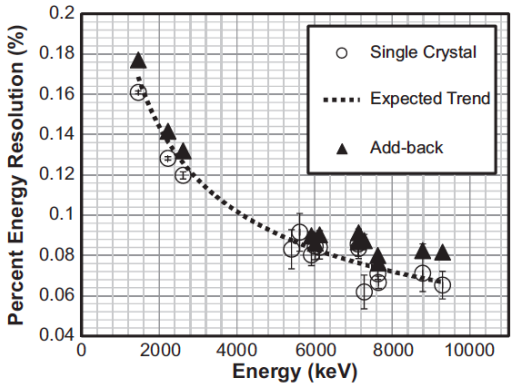

Figure 3.10: Energy resolution of the AGATA detectors is given for the Am-Be-Fe source data. The empty black circles represent the data associated to the single crystal; instead, the black triangles represent the energy resolution for the add-back procedure [57].

gle represent the energy resolution obtained by summing the energies detected by the crystals that fired in each event (add-back). The FWHM of the highest-energy gamma line (i.e. 9297.8 keV) is 6.1 keV in the case of the single crystal, and 7.6 keV for the add-back case.

3.2.8 Efficiency

The other most important property of a multi-detector array is the detection efficiency, which corresponds to the total photo-peak absorption probability over the 4π solid angle. The detection efficiency depends on the energy of the γ-ray detected.

The relative efficiency of γ-ray detection for the AGATA array can be obtained with simulated and in-beam data. Since a crucial point for the experiment described in this thesis is the detection of the high energy γ-rays, it was necessary to evaluate the efficiency of the tracking algorithm and the add-back procedure of the AGATA Demonstrator [57, 58]. Fig. 3.11 provides the γ-ray detection efficiency obtained with tracking algorithm over the efficiency obtained with the add-back procedure as a function of the γ-ray energy in the energy range 2-15 MeV. The 15.1 MeV γ-rays were produced using the reaction $d(^{11}B, n\gamma)^{12}C$ at E_{beam} =19.1 MeV, while γ-rays

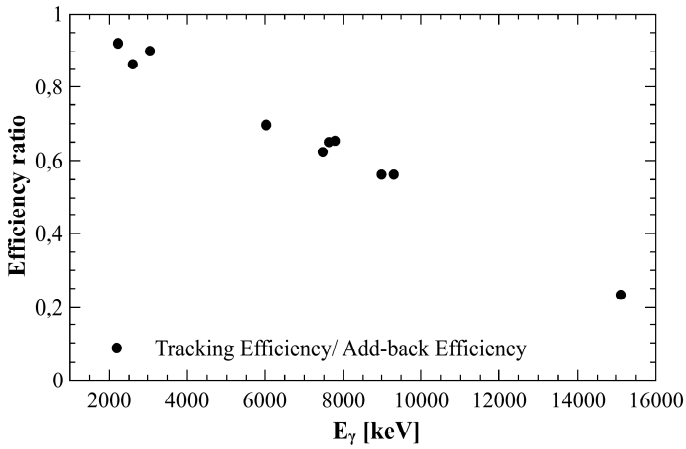

Figure 3.11: Ratio between the tracking and add-back detection efficiency as a function of γ-rays energy for experimental data [58].

between 2 and 9 MeV were produced using a Am-Be-Fe radioactive source. As can be seen the add-back procedure seems to be more efficient at 15.1 MeV. Indeed, this procedure, in the case of the 15.1 MeV γ-rays, resulted to provide four times more counts in the full energy peak than the standard tracking algorithm. This is due to the fact that the 15.1 MeV γ-ray has multiplicity 1, the level of background is low and that the tracking algorithm was optimized in the energy range 0-4 MeV where Compton scattering dominates; at 15 MeV the pair production is the main interaction mechanism instead [57]. For these reason since our physics case involve the measurement of high-energy γ-rays with "multiplicity=1" condition and level of background radiation is sufficiently low the used of the simple add-back procedure is an efficient alternative to standard tracking to produce the γ-rays spectra for this experiment. The add-back efficiency curve of the AGATA array is shown in Fig. 3.12; the efficiency is extracted from simulated data [42].

In order to give a clear overview on the performances of the AGATA Demonstrator array it is interesting to compare it to an other HPGe detector array, named EXOGAM. EXOGAM is an array of 16 segmented Clover germanium detectors shaped in such a way that they can be closely packed at a distance of $\sim$ 11 cm from the target. The 16 detectors are arranged in rings of 4 detectors at 135°, 8 at 90°and again 4 at 45°with respect to the beam direction. Each segmented Clover

Energy [keV]	Tracking Efficiency/Add-back Efficiency [%]
2223	0.92
2612	0.86
3060	0.90
6016	0.70
7471	0.62
7630	0.65
7784	0.65
8992	0.56
9295	0.56
15100	0.23

Table 3.1: Ratio between the tracking and the add-back efficiency data plotted in fig. 3.11.

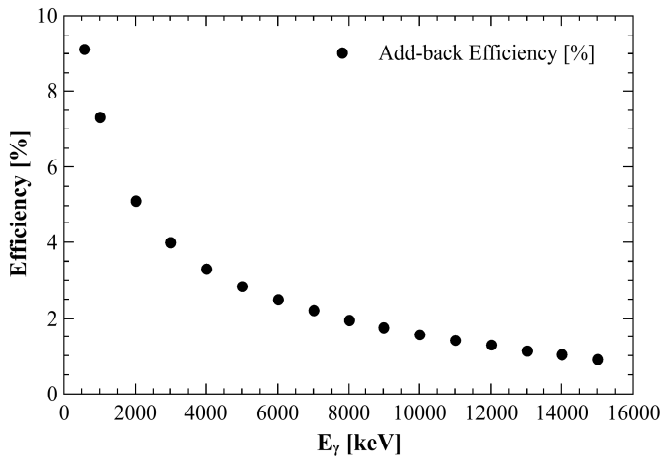

Figure 3.12: Efficiency curve of the AGATA array obtained from simulated spectra created with the add-back procedure. [42]

Energy [keV]	Add-back Efficiency [%]
584	9.1
1000	7.3
2000	5.1
3000	4
4000	3.3
5000	2.9
6000	2.5
7000	2.2
8000	2.0
9000	1.8
10000	1.6
11000	1.4
12000	1.3
13000	1.2
14000	1.0
15000	0.9

Table 3.2: Add-back efficiency data plotted in fig. 3.12.

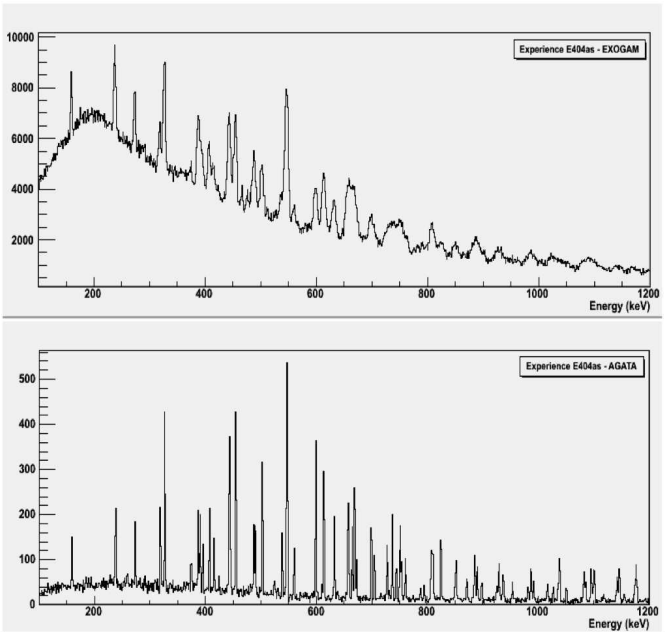

Figure 3.13: Total gamma spectra for EXOGAM (top) and the AGATA demonstrator (bottom). Both spectra are without background subtraction.

detector consists of four coaxial n-type germanium crystals (of 60 mm diameter and 90 mm length) arranged in the configuration of a four-leaf clover and housed in the same cryostat. For more details on it see [59]. In Fig. 3.13 the γ-ray spectra obtained for EXOGAM (upper part) and AGATA (lower part) are presented. While the large EXOGAM efficiency allows collecting more statistics, the much better peak-to-total ratio and the very much improved FWHM, for the AGATA Demonstrator lead to a spectrum of very high quality. Peaks that are hardly resolved with EXOGAM at low energy are well separated by AGATA Demonstrator. In addition, the AGATA Demonstrator does not suffer from the Doppler broadening even at energies around 1 MeV, while finer peak structures already disappear at 700 keV for EXOGAM. In Table 3.3 are reported the performances of the AGATA Demonstrator and the EXOGAN array for a 1.3 MeV γ-ray and a target detector distance of 10 cm for the AGATA demonstrator.

	AGATA Demonstrator	EXOGAM
Ph-efficiency [%]	7.5	18
P/T [%]	65	45
FWHM [keV]	3	15

Table 3.3: Comparison of the AGATA Demonstrator and Exogam array.

3.3 The HECTOR$^+$ Array

Recent studies have shown that a $LaBr_3$:Ce scintillator detector gives an optimal energy resolution for scintillators ($< 3\%$ at 662 keV), an excellent time resolution (<1 ns), a good efficiency and a negligible variation of the light output with temperature. Furthermore, the study of the signal line-shape allows to discriminate between alpha particle and γ-rays, using Pulse Shape Analysis techniques [60]. Thanks to the availability of $LaBr_3$:Ce crystals in volumes larger than $1000cc$, an array based on these scintillators (eventually coupled with HPGe detectors) will constitute an extremely performing, efficient, cost-effective and easy to handle array for gamma spectroscopy experiments. Indeed the good energy resolution and high efficiency allow the measurement of low and high-energy γ-rays in nuclear physics experiments in a wide energy range (0-40 MeV), as for example the measurements of the gamma decay of the Giant Resonances. In addition the sub-nanosecond time resolution enables an extremely efficient rejection of background radiation not originating from target position. Moreover thanks to the fast decay time constant (16 ns), these detectors could be used with count rates of hundreds of kHz.
In the experiment described in this thesis, 9 large volume $LaBr_3$:Ce detectors (of the HECTOR$^+$ array) [39], were placed around the AGATA Demonstrator array (see Fig. 3.14).

The signal of each HECTOR$^+$ crystal was sent for its processing to a channel of a LaBrpro module [61]. LaBrpro is a custom spectroscopy amplifier developed in Milan for the shaping of $LaBr_3$:Ce signals; it has 16 channels and for each of them it gives a "fast" and a "slow" outputs, corresponding to the fast and slow components of the signal, as well as a "time" output obtained by a Constant Fraction Discriminator (CFD).

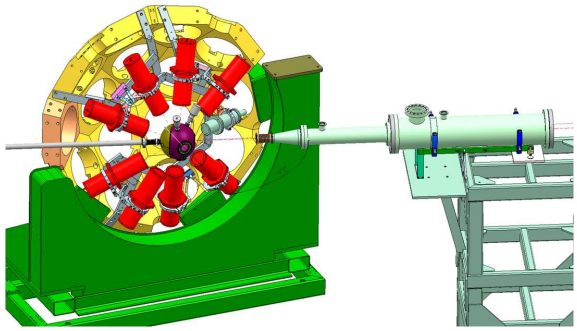

Figure 3.14: Schematic view of the installation set-up of the HECTOR$^+$ array: the red coloured detectors are 3.5"x8", the gray one is 3"x3".

3.3.1 Energy Resolution

The energy resolution and the efficiency are crucial factors in case of high-energy γ-rays measurement. Lanthanum bromide detectors allow clear separation of the full energy from the first escape peak up to 25-30 MeV (which was previously possible only with HPGe detectors). For this reason, they are particular suited in the experiment described in this thesis. This means that this experiment could be used as a commissioning to study the performances of these detectors in an beam experiments.
Unfortunately the performances of $LaBr_3$:Ce (3.5"x8") crystals cannot be easily scaled from those of smaller ones [2], because of possible self absorption or possible incomplete reflections of the scintillation light, count rate effects, large PMTs, crystal in-homogeneities and a much higher sensitivity to high energy γ-rays. For these reasons, in order to characterize the HECTOR$^+$ array for this experiment mono-energetic γ-rays from 1 MeV up to 22.6 MeV at Debrecen ATOMKI Laboratories (Hungary) have been measured. In the energy range used between 2 and 9 MeV calibration sources have been used, e.g. ^{60}Co, ^{133}Ba, ^{137}Cs, ^{152}Eu, ^{88}Y and an Am-Be-Ni source. Monochromatic γ-rays with energy above 9 MeV can be obtained only with accelerator-driven nuclear reactions. The reactions used are reported in Table 3.4.

Fig. 3.15 shows the FWHM energy resolution in the energy range between 1 and 22.6 MeV obtained at the ATOMKI Institute, with one detector of the HECTOR$^+$

Reaction	E_{res}	γ-ray energy [keV]
$^{39}K(p,\gamma)^{40}Ca$	1346.6	3904.4 5736.5
$^{23}Na(p,\gamma)^{24}Mg$	1318.1	1368.6 11584.8
$^{27}Al(p,\gamma)^{28}Si$	767.2	2838.7 7706.5
$^{23}Na(p,\gamma)^{24}Mg$	1416.9	2754.0 8925.2
$^{7}Li(p,\gamma)^{8}Be$	441	17619
$^{11}B(p,\gamma)^{12}C$	675	4438.0 12137.1
$^{11}B(p,\gamma)^{12}C$	7250	22600

Table 3.4: Reactions obtained at the ATOMKI Institute are tabulated. The corresponding proton energy and the γ-ray energies produced are reported.

array coupled to an active voltage divider, developed by the electronic group of INFN Milano and the analog electronics. As can be seen in Fig. 3.15 the energy resolution of the $LaBr_3$:Ce detectors deviates from a strictly statistical behaviour, i.e. $\frac{1}{\sqrt{E}}$ asymptotic curve (dashed curve), in case of high-energy γ-rays showing that the energy resolution of $LaBr_3$:Ce detectors tends to saturate at constant value around $0.5 - 1\%$. The continuous red line takes into account this saturation contribution and it has the following expression:

$$ER_{FWHM} = \sqrt{400 + 0.625E + 28 \cdot 10^{-6}E^2} \tag{3.4}$$

For more details see [39].

A measured high-energy monochromatic γ-ray spectra acquired with one of the crystal of the HECTOR$^+$ array is shown in Fig. 3.16, it is possible to see the full energy peak and the first escape peak clearly resolved.

3.3.2 Efficiency

The absolute γ-ray detection full energy peak efficiency of a 3.5"x8" volume detectors was estimated by means of the sum peak technique [62]. A ^{60}Co source positioned at a distance of 10 mm ($\pm$1 mm) from the detector front face was used. Fig. 3.17 shows the experimental results, together with the GEANT3 simulation results (from 100 keV up to 30 MeV), very well in agreement with each other. Fig. 3.17 shows the simulated efficiency (performed with GEANT3) for a source positioned at 200 mm from the detector front-face.

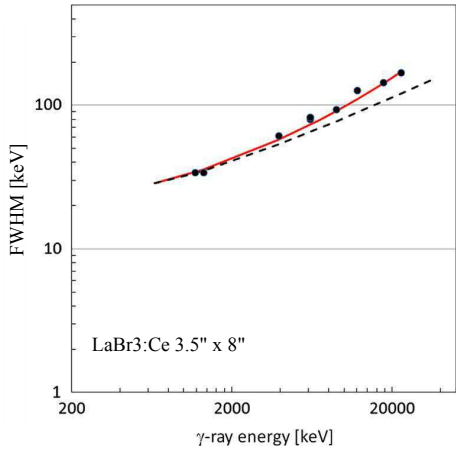

Figure 3.15: The FWHM energy resolution in the energy range between 1 and 22.6 MeV obtained with one detector of the HECTOR$^+$ array. The dashed line represents the energy estimation based only on statistical and electronic noise contribution, instead the continuous red line represent the function of Eq. 3.4 that takes into account the saturation effects present at high γ-rays energy [39].

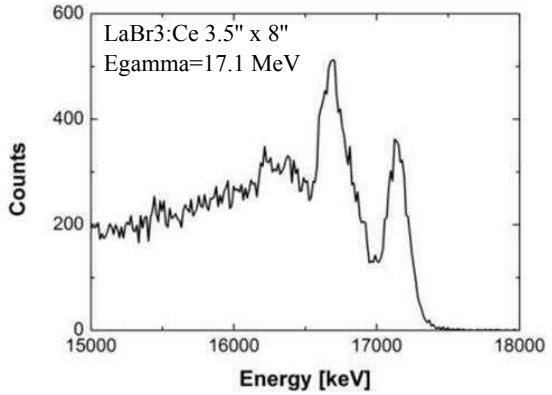

Figure 3.16: The gamma spectrum of the reaction $^{11}B(p,\gamma)^{12}C$ at 17.6 MeV. It is possible to see the clear separation between the full energy peak and the first escape peak [39].

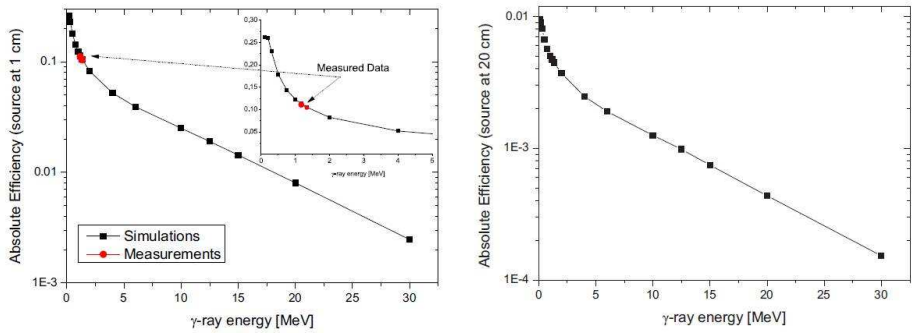

Figure 3.17: Measured values of absolute efficiency for a crystal of the HECTOR$^+$ array, with a ^{60}Co source positioned at a distance of 10 mm ($\pm$1 mm) from the detector on the right and at 20 mm on the left [39].

In conclusion, it has to be pointed out that even if the energy resolution of these scitillator detectors is not good as the one of the AGATA detectors, it is enough to resolve almost all the transitions in the PDR region. In addition, the used of the HECTOR$^+$ array permits to increase the efficiency for the detection of γ-rays with energy above 5 MeV. For these reasons, the used of the AGATA Demonstrator coupled to the HECTOR$^+$ array is a powerful tool to study the gamma decay from high lying nuclear states.

3.4 The Data Acquisition System

As mentioned in Sec. 3.2.2, the electrical contacts of each AGATA detector are divided into 36 segments and the digitizers sample the pulses from each segment at 14 bits precision with a frequency of 100 MHz; for every accepted event, a pulse trace of 60 samples is extracted and acquired. With a counting rate of 50 kHz/crystal the data-flow for each detector is therefore of the order of 100 MB/s (with zero suppression). Furthermore, in order to have an online analysis, the PSA has to be performed in real time for each of the acquired traces and tracking algorithms must reconstruct the detected γ-rays from the PSA information.
This means that the Data Acquisition (DAQ) software for AGATA has to be able to handle large quantities of data, control a computing farm for the PSA and tracking algorithms, and coordinate the flow of information between the digitizers, the

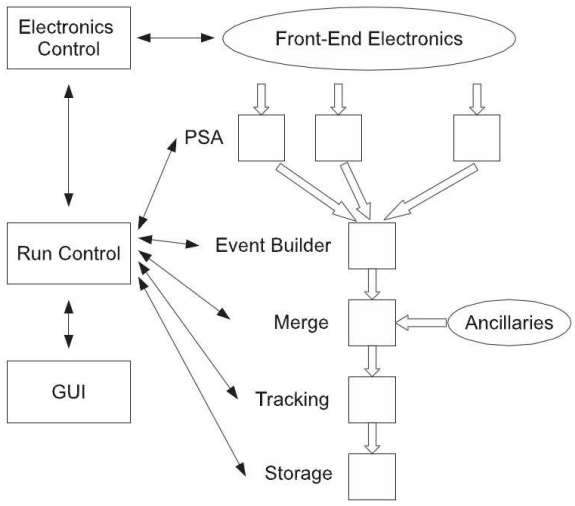

Figure 3.18: Layout of the AGATA acquisition system, NARVAL, [38].

computing farm, and the disk server where all the data are written. All of this is performed by a NARVAL-based DAQ software [63].
The ancillary detectors (TRACE and HECTOR$^+$) were controlled by an independent DAQ running on a KMAX environment [41], which communicated with the VME crate via an optical fibres and with NARVAL via TCP/IP.
NARVAL is based on actors corresponding to separate processes that receive and send out data at any stage of the data-flow chain; actors communicate with each other with a UNIX fifo if running on the same machine or with a TCP/IP socket if running on different machines. There are 3 types of actors:

- producer: they interface with the hardware and read out the data;
- intermediary: they perform operation on the data, receiving input and sending output from/to one or more other actors;
- consumer: they can only receive input from the other actors and store the data to disk or act as histogrammers.

From the point of view of NARVAL, each AGATA detector is considered as a separate entity and the whole array may be considered as the aggregation of synchronized data supplied by the individual crystals. The synchronization is guaranteed

by the AGATA Global Trigger and Synchronization (GTS) hardware with a common 100 MHz digital clock.
For each AGATA detector there is a producer actor reading the pulse traces from the front-end electronics; the traces are sent (together with the timestamp information) to an intermediary actor that performs the PSA and to a consumer that writes them to disk; the PSA data from all detectors are sent to an intermediary actor that acts as event builder, matching the data from different detectors through the timestamp information. For the ancillary detectors, there is a producer actor that receives the data from the KMAX acquisition, kept synchronized to the GTS via the AGAVA (AGATA Ancillary VME Adapter) module. The producer sends the VME data to a consumer that writes them to disk and to an intermediary that decodes the VME words and sends only the actual data words to the event builder, discarding VME header and trailer words. The builder then matches the ancillary data to the AGATA data and sends the event to another intermediary that performs the online tracking. A schematic representation of the Data Acquisition System is given in Fig. 3.18.

3.5 Trigger Conditions

When a γ-ray is detected in an AGATA crystal, a trigger request is formed and sent via the GTS to the trigger processor, which can validate the request (meaning that all the information about the event are acquired, written and processed) or reject it. This software trigger can be used to make multiplicity requirements on the AGATA crystals, or to make a coincidence between AGATA and the ancillary detectors via the AGAVA module.

This way to proceed was not suitable for this experiment, because a more complex trigger was needed. Therefore, a standard NIM electronics was used to build the master gate trigger and to send it via AGAVA as a trigger request to the DAQ system. The master gate is schematically described in Fig. 3.19 and is the logical OR of four conditions:

- the coincidence between TRACE and AGATA
- the coincidence between TRACE and HECTOR$^+$
- the TRACE scaled-down singles (1/50)

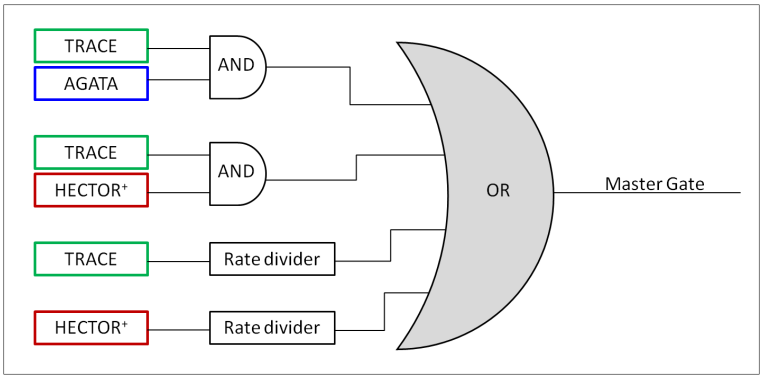

Figure 3.19: Schematic view of the trigger conditions used during the experiment. The hardware and software components are put in evidence.

- the HECTOR$^+$ scaled-down singles (1/250)

where the AGATA trigger was made using the analog output of each AGATA detector (present for debug purposes), sent to a standard CFD modules and to a logical OR; the TRACE trigger was the OR of all the pads of the two E detectors, taken from the amplifiers; and the HECTOR$^+$ trigger was the OR of all the $LaBr_3$:Ce detectors, taken from LaBrPro electronic amplifier module [61]. The resulting trigger is schematically described in Fig. 3.19.

The coincidence between TRACE and the γ-ray detectors was setup in such a way that the gate opens when there is a signal in one of the E detectors. In this way both types of coincidence events (TRACE-AGATA and TRACE-HECTOR$^+$) have a common time reference, since in both cases the Master Gate is opened by the TRACE E detectors.

Chapter 4

Data Analysis

A preliminary step of the analysis was the data reduction. The first part has been focused on the presorting of the raw data. In order to obtain better performances of the Pulse Shape Analysis (PSA) and tracking algorithm, the so-called "replay" of the data is needed. This means that the same procedure of performing PSA and γ-ray tracking on-line, i.e. during the experiment, has to be done off-line, starting from the pulse shape of the HPGe AGATA detectors written to disk.
After that the data reduction for each detectors have been performed concerning the time and energy calibrations, drift correction, ejection identification for Silicon detectors and correction of the Doppler effect for γ-rays detectors. The "replay" procedure is described in sec. 4.1. The time spectra are shown in sec. 4.2. The energy calibration procedure for each array and the drift correction for the silicon detectors are described in sec. 4.3. In sec. 4.4 the technique for the identification of the ejectile is depicted. The Doppler correction for the γ-ray emitted in-flight was performed, see sec. 4.5.
Due to the non-spherical geometry of the TRACE telescopes a number of events were lost if considering only the standard ΔE-E combination of pads. In order to increase the statistics other configurations of pads were considered, see sec. 4.6.
At this point of the analysis only one more condition has to be applied to extract the final energy spectrum of the gamma decay from the PDR region. In sec. 4.7 the correlation between the γ-ray energy and the excitation energy transferred to the target nuclei is described. In order to clearly identify the gamma decay from

the PDR, a background subtraction was performed as shown in sec. 4.8.1. Finally, sec. 4.8 shows the γ-ray energy spectrum of the PDR in ^{124}Sn.
In addition, since the inelastic scattering of ^{17}O at 20 MeV/u is expected to populate strongly the giant resonance region of the target nuclei, the energy spectra of the inelastic scattered ^{17}O ions were investigated in sec. 4.9.

4.1 Replay of the Data

As described in Sec. 3.2 the performances (i.e. energy resolution, efficiency and P/T ratio) of the AGATA Demonstrator depend on the performances of the PSA and tracking algorithms. During the experiment these operations are done in real time by the NARVAL Data AcQuisition (DAQ) system (see also Sec. 3.4), but they can also be performed after the experiment with a C++ emulator of NARVAL.
This is possible because the DAQ writes to disk a list-mode file for each detector, containing the digitized pulse signals from the segments and the timestamp information for each event; the emulator can process all these files, running again the PSA and γ-ray tracking and matching the AGATA and ancillary data. This procedure is called "replay", because from the point of view of the data processing it is essentially a repetition of the experiment.

In the case of the present experiment, the replay was necessary in order to apply a better calibration to the AGATA detectors segments (see Sec. 4.3.2), since the calibration used on-line was not very accurate being based on a short run at the beginning of the data taking. We could also make use of improvements in the PSA that were not available at the time of the experiment, such as the correction for neutron damage (see Ref. [38] and references therein).

The replay was performed in two steps:

1. The energy calibration was applied and the PSA was performed for all AGATA detectors. The original data, including the pulse shapes of each HPGe detector were "reduced" to only energy, position and time information; for all the events they were saved to disk.

2. The data from all the segments were merged and the tracking was performed. The ancillary detectors were calibrated and data from the AGATA, HECTOR$^+$ and TRACE arrays were combined for each event.

The advantage of this separation in two steps is that the PSA is a very long process, requiring a large amount of computing power and memory: in the present experiment about one week was needed to perform the first step with 10 computers working in parallel. The tracking, instead, is a much faster procedure and could be repeated several times as we changed parameters, without having to perform the PSA again.

After the replay is completed, the user is given a list-mode file in ROOT tree format. For each event, the file contains the list of reconstructed gammas, together with their energy, time information and the position of the first interaction, as well as the data of the ancillary detectors received from the VME crate. A sorting code was developed for the analysis of the list-mode data.

4.2 Time Spectra

4.2.1 TRACE Time Spectra

During the experiment, a time signal was acquired for each pad of the Silicon detectors by two VME Time-to-Digital Converters (TDCs). The TDCs worked in "common start" mode: each TDC channel is started by the master trigger (see Sec. 3.5) and is stopped by the delayed time signal of the silicon pad. Note that this means that the start of all the TDCs is given by the E detectors in case of a TRACE-γ coincidence. The timing of the Silicon detectors is affected by the large spread in energy (and time of flight) of the various reaction products. Fig. 4.1 shows the time spectrum obtained by gating on the ^{17}O scattering reaction channel for both one pad of the E, (a), and of ΔE, (b), detectors.

For the rest of the analysis, all the TRACE spectra were gated on the time peak of the E detector.

4.2.2 AGATA Time Spectra

Each γ-ray reconstructed by the tracking algorithm is associated to a timestamp T_{AGATA}, which measures the absolute time from the start of the Global Trigger and Synchronization (GTS) clock in steps of 10 ns. A more precise information is given by the PSA, that uses a Constant Fraction Discriminator (CFD) to determine the start time of the signal t_{CFD}. The sum of these two values gives the detection

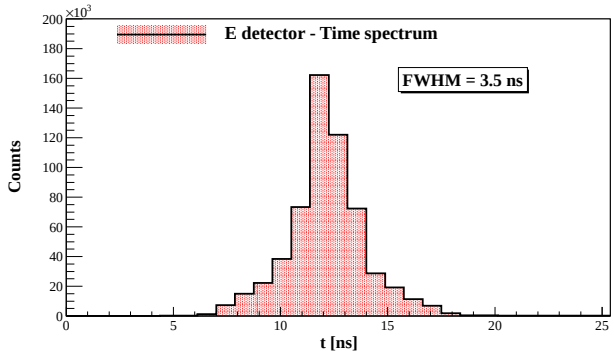

(a)

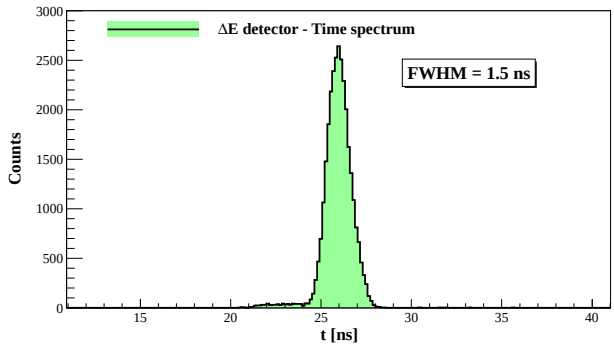

(b)

Figure 4.1: Time spectra for one pad of the E, (a), and ΔE, (b), Silicon detectors under the gating condition that an ^{17}O is detected in the pad.

time of the gamma relative to the start time of the GTS, as reported in Eq. 4.1.

$$time_{TT} = T_{AGATA} + t_{CFD} \tag{4.1}$$

Figure 4.2 shows the AGATA time spectra, obtained by choosing one of the 15 detectors as a reference and by measuring the time difference between that detector and the other. A time walk of $\sim$ 10 ns was observed, as one can see in the (a) panel. This has been corrected by adding an offset term during the second step of the data replay (within the tracking algorithm). The resulting spectra, after the correction, are shown in the (b) panel: here the spectra are aligned in less than 5 ns, that is smaller than the time resolution of HPGe detectors ($\sim$ 10 ns).

In order to obtain useful physical information, however, the detection time of the γ-ray must be correlated to the detection time of the ^{17}O ions. This work, at the first stage, is done by the Narval emulator, that creates spectra obtained as the difference between each AGATA detector and the AGAVA (i.e. TRACE ancillary detectors) time stamp, in step of 10 ns. A better precision can be obtained either by adding to the AGAVA timestamp the so-called "phase shift" $t_{phase-shift}$ and by including the CFD information t_{CFD} to the AGATA timestamp. The AGAVA phase-shift is acquired by one channel of the TDCs and measures when the VME master gate was opened relative to the GTS clock, while the CFD information is extracted during the PSA, as mentioned before. The AGATA time relative to the trigger time is then defined as follows:

$$t_{\gamma} = T_{AGATA} + t_{CFD} - T_{AGAVA} - t_{phase-shift} \tag{4.2}$$

where T_{AGATA} and T_{AGAVA} are the timestamps for AGATA and for the ancillary detectors, as obtained by the Data Acquisition System.
The spectrum shown in Fig. 4.3 is obtained by calculating for each γ-ray the time information as given by Eq. 4.2.

4.2.3 HECTOR$^+$ Time Spectra

Another time spectrum useful for the analysis is obtained from the time difference between the trigger of the acquisition and the HECTOR$^+$ detectors, here indicated as t_{HECTOR^+}. This information is given by the TDC, because these modules

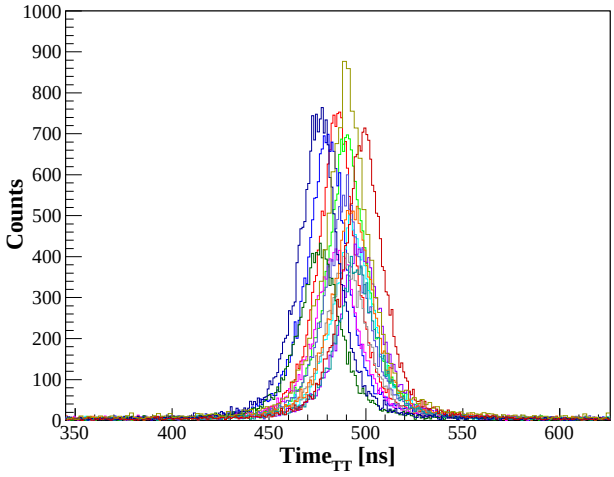

(a) Not Allined

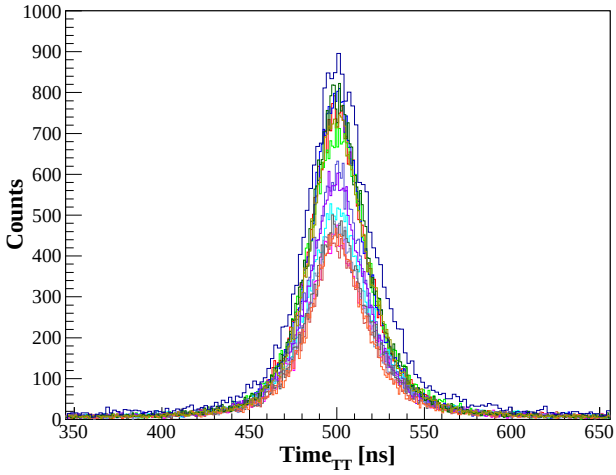

(b) Allined

Figure 4.2: Time spectra of all AGATA detectors against a reference one, before ((a) panel) and after ((b) panel) the correction of the time walk

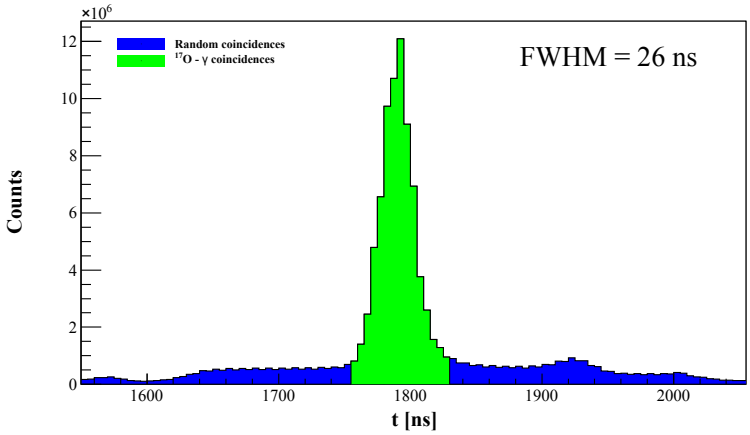

Figure 4.3: Example of time AGATA vs TRACE spectrum constructed following Eq. 4.2

work in "common start" mode, meaning that each TDC channel is started by the master trigger (see Sec. 3.5) and is stopped by the time signal of the corresponding $LaBr_3$:Ce detector. Fig. 4.4 shows the time spectra of one of the HECTOR$^+$ detectors. The narrow peak centred at 300 ns corresponds to the coincidences between the detector and a ^{17}O event in the TRACE array, while the tail to the right of the coincidence is caused by neutrons as indicated in the figure. The blue regions of the spectrum is related to background events.

4.3 Energy Calibration

4.3.1 TRACE

Since there are no long-lived emitters of alpha particles with higher energy, the energy calibration of charged particle detectors with radioactive sources is only possible up to a few MeV of energy. For this reason and since the energy loss in the E and ΔE detectors was known, the calibration where performed by fitting the peaks related to the elastic peak in the ΔE and E pads. The scaled down single allows to have this information. From this procedure we extract the calibration coefficients for each pad of the ΔE and E pads. Fig. 4.5 shows the energy spectrum

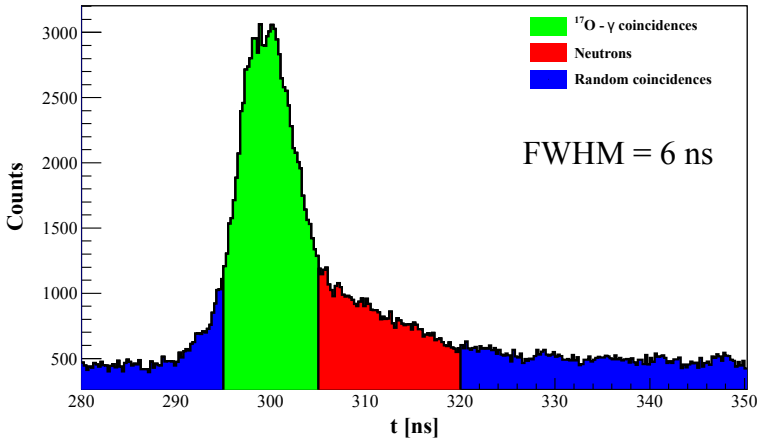

Figure 4.4: Time spectra of one of $LaBr_3$:Ce detectors of the HECTOR$^+$ array, with respect to the master trigger signal.

of a ΔE (a) and E pad (b).
Once the ΔE and E detectors have been calibrated, it was possible to sum the energy deposit in each ΔE pad with the energy deposit in the E pad behind it, obtaining a measure of the Total Kinetic Energy (TKE) of the ions stopped in each pad of the telescope. Fig. 4.5(c) shows the TKE spectrum measured in one pad.

Drift Correction

During the course of the experiment, the leakage current passing through the detectors has steadily increased due to the radiation damage caused by the scattered beam. This effect causes a gradual loss of the energy resolution and a variation over time of the energy gain for the different pads.
These effects can be clearly seen in Fig. 4.6(a), where the TKE for one pad is shown in relation to the time (measured by the event counter): the pad has a clear drift of the elastic peak energy, as well as a degradation of the energy resolution.

In order to correct the drift, a fitting of the elastic peak every $\sim$ 5 million events have been performed. In this way a series of recalibration coefficients have been obtained and used for an event-by-event correction. The result is shown in Fig. 4.6(b). The pad is the same of Fig. 4.6(a). Thanks to this correction, there

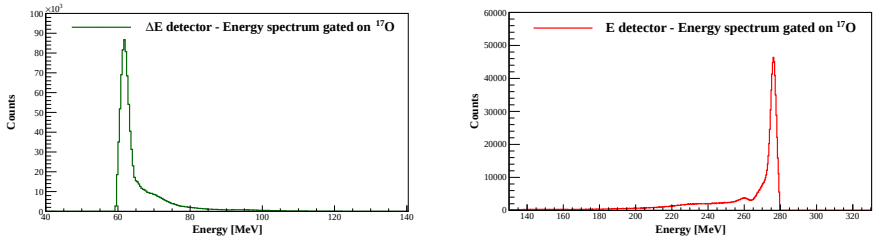

(a)

(b)

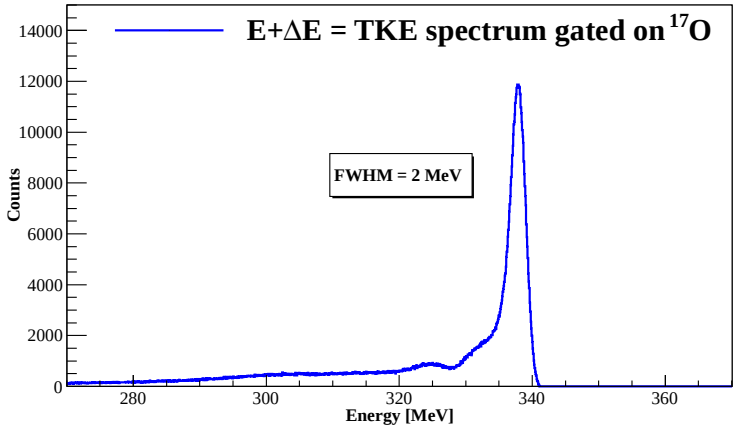

(c)

Figure 4.5: Energy spectra for one pad of the ΔE, (a), and E, (b), Silicon detectors under the gating condition that an ^{17}O is detected in the pad. The Total Kinetic Energy spectra is shown in (c).

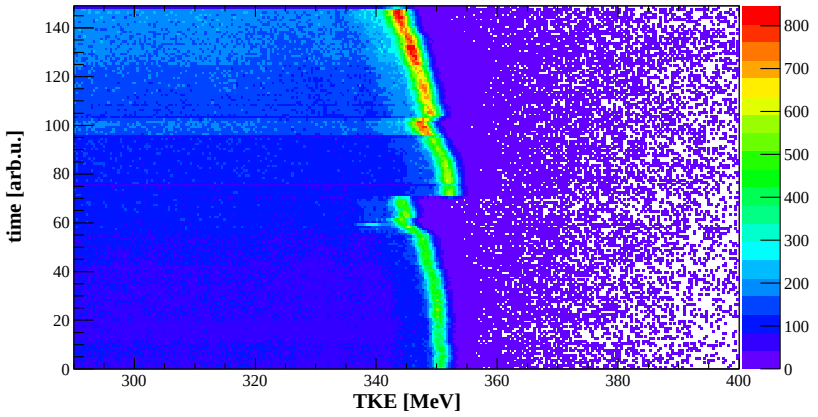

(a)

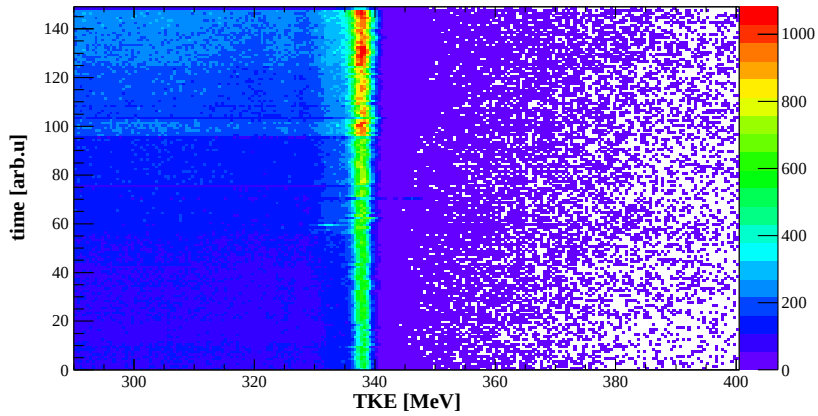

(b)

Figure 4.6: Scatter plot of the energy measured in one pad of the TRACE telescopes versus the time of acquisition. The (a) panel shows the pad with a clear drift over time, while the (b) panel shows the same pad after the drift correction.

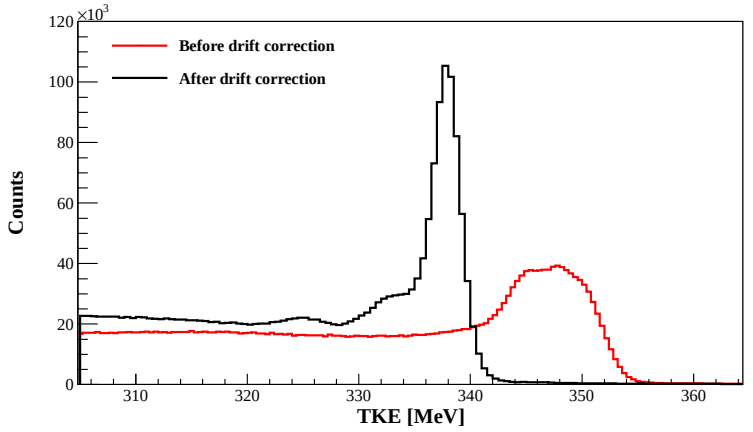

Figure 4.7: Total Kinetic Energy spectrum measured in the same pad before (in red) and after (in black) the correction for the gain drift.

was a clear improvement in the energy resolution, see Fig. 4.7. The FWHM after the drift correction was ~ 2 MeV at 340 MeV.

4.3.2 AGATA

The energy calibration of the AGATA detectors is performed during the first step of the replay, together with the PSA. The calibration coefficient for each segment of the 15 detectors and for the core electrode were calculated using calibration runs acquired with an ^{137}Cs, ^{60}Co and ^{88}Y sources. Fig. 4.8 shows the energy spectrum used for the calibration.

The front-end electronics for the AGATA detectors has two settings, one for low dynamic range (up to 4 MeV) and one for high dynamic range (up to 20 MeV). In the present experiment, the 20 MeV range was used, although it is known that the segments show a non-linearity at high energies with this setting. While this effect is not large enough to compromise the performance of the tracking algorithms, it can deteriorate the energy resolution of the reconstructed γ-rays. Since this non-linearity affects only the segments, and not the core signals of the detectors, it is possible to correct this effect requiring in the tracking algorithm that, for every event, the sum of the segment energies in a crystal is recalibrated to be equal to the energy measured in the core.

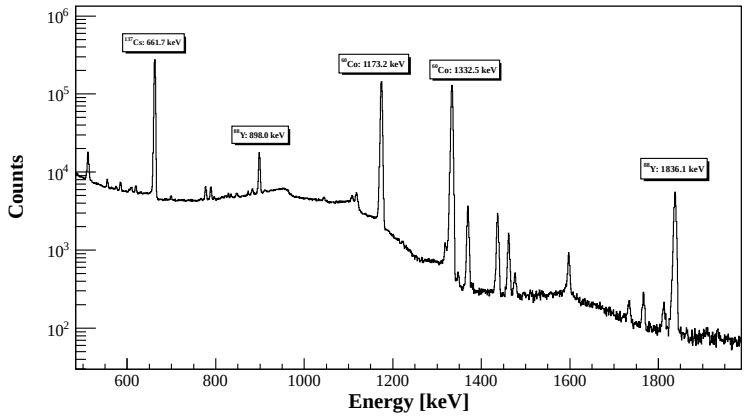

Figure 4.8: Energy spectrum from ^{137}Cs, ^{60}Co and ^{88}Y sources measured with the AGATA Demonstrator. The spectrum has been obtained after recalibrating segment energies with the energy measured by the core, for each crystal.

After this first calibration, the calibration coefficients were refined in order to check the gain stability over the time. This was done by choosing a set of reference lines and comparing the measured energy with the known value, for each crystal and each run. A new linear calibration was applied and the coefficient of the linear term was plotted, as shown in Fig. 4.9. The gain variation over the all measurement, that lasted one week, is less than 0.3 % indicating that the AGATA detectors were very stable.

4.3.3 HECTOR$^+$

All the $LaBr_3$:Ce detectors of the HECTOR$^+$ array were calibrated in energy with standard radioactive sources such as ^{137}Cs and ^{60}Co.
A recalibration for each HECTOR$^+$ detectors was necessary for the spectra taken during the measurement, probably due to the higher counting rate. This was performed by taking the energy spectra gated on the ^{17}O scattering channel and performing a fit on the decay from the first 2^+ state to g.s. (corresponding to a γ-ray energy of 1131.69 keV) and on the decay from the first 3^- state to the first excited state (corresponding to a γ-ray energy of 1470.71 keV) of ^{124}Sn. Fig. 4.10 shows the energy spectrum of the HECTOR$^+$ detectors after the recalibration with

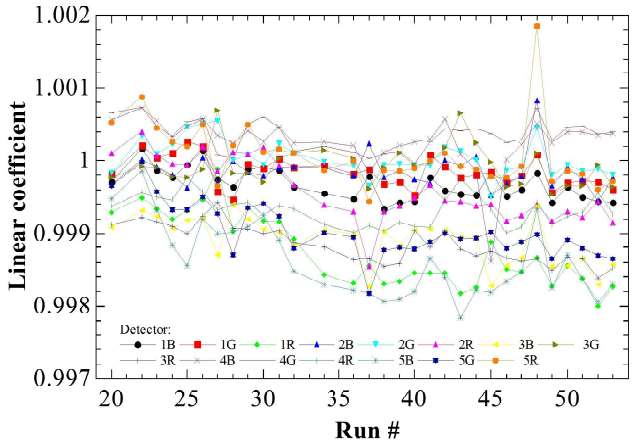

Figure 4.9: The coefficient of the linear term of the recalibration fit is plotted for each crystal and for each run. The gain fluctuations are within 0.3 %.

Isotope	Population [%]
^{18}O	9.1
^{17}O	54.3
^{16}O	36.6

Table 4.1: Oxygen isotopes population.

the ^{124}Sn gamma-decay lines.

4.4 Ejectile Identification

The identification of the scattered ions detected in the TRACE array was performed with the standard ΔE-E technique. The ΔE-E technique is applicable when particles with kinetic energy E_0 pass through a first detector, ΔE detector, and are stopped in the second one, E detector. The partition of kinetic energy E_0 between the two detectors is different for different particles, due to their different stopping powers.

A typical ΔE-E matrix obtained for one pad is shown in Fig. 4.11(a). A clear separation between ions from Boron to Fluorine is visible. In particular a clear

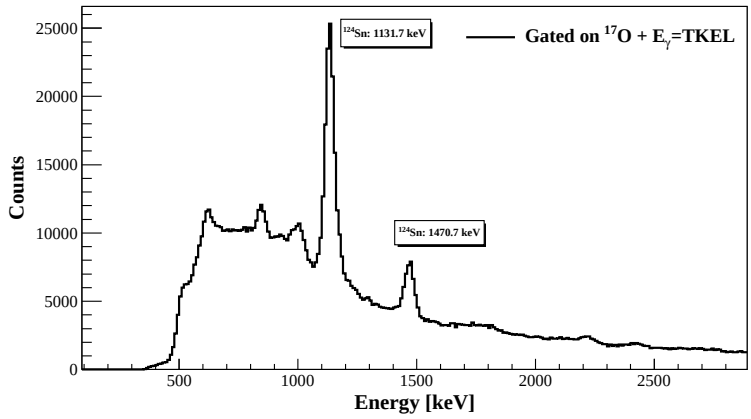

Figure 4.10: Energy spectrum recalibrated with ^{124}Sn gamma-decay measured with the HECTOR^{+} detectors.

mass separation could be observed in Fig. 4.11(b) where the region of the oxygen isotopes is depicted and the relative population is reported in Table 4.1.

The selection of the events related to the ^{17}O scattering was performed by applying a gate condition on the energy loss of the ion. In particular, the request for each event was that the energy loss in one pad of the ΔE detector and the TKE must be inside of the black solid line depicted in Fig 4.11(b) as well as the time signal of the E detector must be inside the self-coincidence peak, see Fig. 4.1, while all the other pads were without signal.

4.5 Doppler Correction

4.5.1 Doppler Correction for the Target-like Partner

The scattering of the ^{17}O beam transfers some recoil kinetic energy to the target nuclei. The amount of this recoil energy can be calculated with simple kinematics considerations, as shown in Appendix A.

The speed obtained for the recoil is of the order of 0.5% of the speed of light.

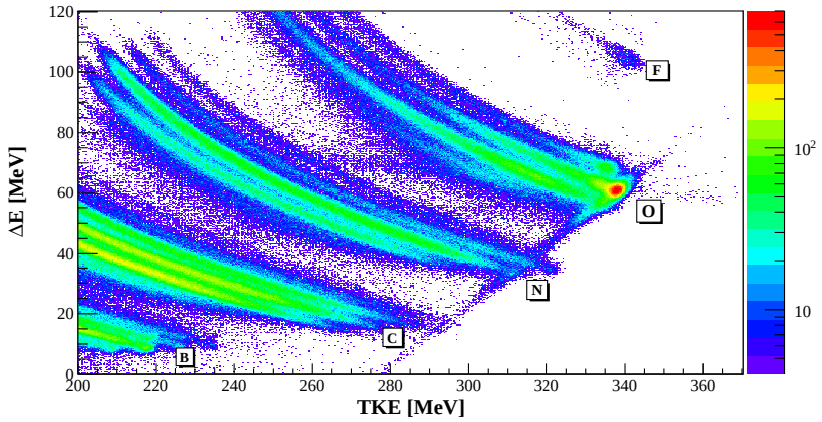

(a)

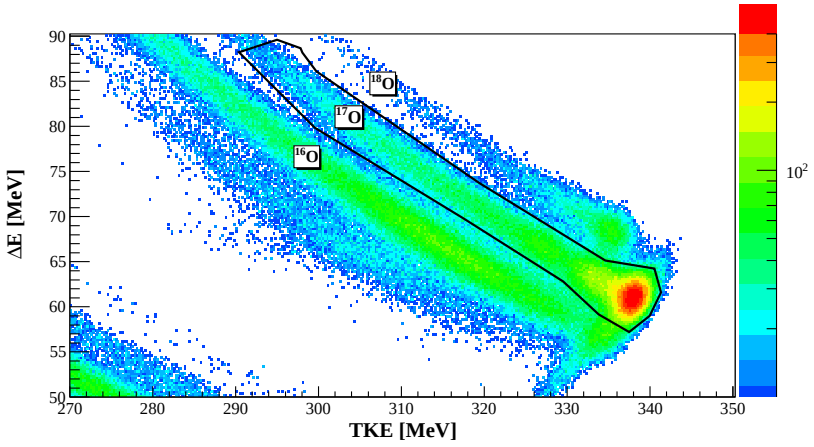

(b)

Figure 4.11: Scatter plot of the Total Kinetic Energy measured in one pad of the TRACE telescopes versus the energy deposit measured in the ΔE pad. The (a) panel shows the full range of ions that were measured, while the (b) panel shows the separation between the oxygen isotopes.

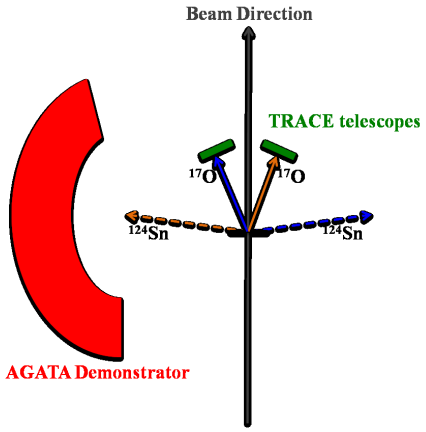

Figure 4.12: Schematic view of the direction of the ^{17}O ions (solid line) and of the recoiling ^{124}Sn ions (dashed line) when an ^{17}O has been detected in the left or right telescope.

While this value of β is quite small, it is enough to cause a shift of more than 10 keV for high energy γ-rays. This can be seen clearly if we compare the γ-ray energy spectrum obtained in coincidence with an ^{17}O ion detected in the left TRACE telescope with the one in coincidence with the right telescope. Indeed, due to kinematics in one case the recoil goes away from the AGATA Demonstrator, while in the other goes towards it, as shown in Fig. 4.12.

Fig. 4.13(a) shows the gamma decay from the first 3^- excited state, at an energy of 1471 keV, of the ^{124}Sn detected in coincident with an ^{17}O in the left telescope, blue spectrum, and with an ^{17}O in the right telescope, red spectrum. Due the short-lifetime of the state, the γ-ray is emitted when the ^{124}Sn is still recoiling and for that the two spectra are clearly shifted.
In order to perform a Doppler correction for the recoil, Eq. A.5 has been used to associate to each pad of the TRACE telescope the velocity vector of the corresponding recoil, and kept a fixed value of v/c. The result of the Doppler correction is shown in Fig. 4.13(b) for the 1471 keV line of the ^{124}Sn.

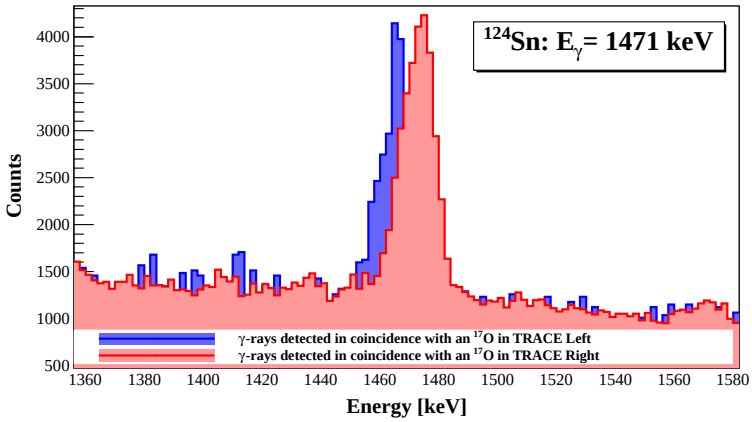

(a)

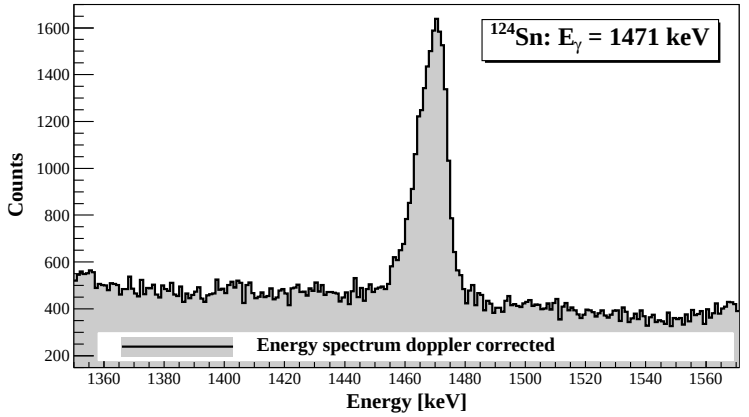

(b)

Figure 4.13: Energy spectra of the γ-rays in coincidence with an ^{17}O ion measured in the left, blue spectrum, or right, red spectrum, TRACE telescope ((a) panel). The (b) panel shows the spectrum after the Doppler correction

4.5.2 Doppler Correction for the Projectile-like Ejectile

One of the main challenges of the next generation of gamma spectrometers will be the detection of γ-ray emitted in-flight by radioactive beams, in condition of high background and relativistic velocity. For this reason, it was interesting to study the gamma decay from the projectile-like ejectiles produces in our experiment as they had a v/c of the order of 20%.
We choose to focus on the ^{16}O because it has a very strong γ-ray line at 6129 keV where the Doppler effect is larger and the background from the target lower.
The Doppler correction was applied using the well-known equation:

$$E_{corr} = E_{lab}\frac{1-\beta\cos\theta}{\sqrt{1-\beta^2}} \tag{4.3}$$

where E_{lab} is the energy measured in the laboratory frame of reference, E_{corr} is the energy of the projectile frame of reference, and θ is the angle between the projectile velocity vector and the γ-ray velocity vector.

For the γ-rays detected by the AGATA Demonstrator, the direction of the γ-ray velocity vector was determined by the position of the first point of the interaction the AGATA Demonstrator. Tracking algorithms are able to determine, for each reconstructed γ-ray, the first interaction point and its coordinates, which are given as a part of the output in the ROOT tree. The coordinates for the interaction points are given in the AGATA frame of reference.
The direction of the projectile velocity vector was similarly determined by the position of the pad in which the ion was detected. In order to account the uncertainties in the position of the silicon detectors, we performed an optimization procedure for the position of the telescopes. Starting from the design position, we have moved them horizontally in a 1 cm x 1 cm large grid with step of 1 mm. For each point a figure of merit that takes into account the FWHM and the correct energy of the ^{16}O line was evaluated. The procedure was applied for the data measured with the ^{208}Pb target that had the same geometries of the ^{124}Sn. For the rest of the analysis, we used the optimal positions found in this way as the reference position of the TRACE telescopes.
The spectra obtained for the ^{16}O gamma-decay are shown in Fig. 4.14 measured in coincidence with one pad of the TRACE telescope. The Doppler correction

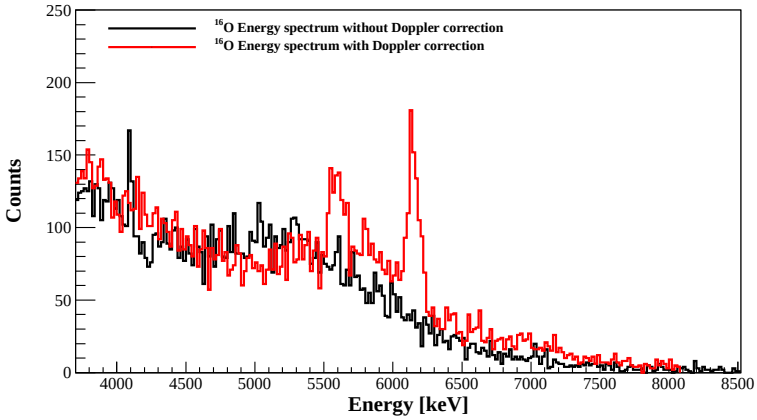

Figure 4.14: Energy spectra of the γ-rays measured in coincident with the ^{16}O reaction channel, measured by one pad of the TRACE telescope, for the AGATA Demonstrator before, black spectrum, and after, red spectrum, the Doppler correction

was performed with the optimal position of the TRACE telescopes and the full information of the PSA and tracking. A fixed value of β=0.203, calculated from the reaction kinematics, have been used. The Fig. 4.14 shows clearly a marked improvement in the energy resolution of the Doppler-corrected spectrum thanks to the high position resolution of the AGATA detectors.

The same procedure was applied for γ-rays of ^{16}O detected by the HECTOR$^+$ array. In this case, the γ-ray velocity vector was determined by the position of the centres of the crystals and the projectile velocity vector in the same way described above. Fig. 4.15 shows the γ-ray spectra before and after the Doppler correction. Even if the correction is limited by the not so good angular resolution of the HECTOR$^+$ array (each detectors cover an angle of about 20°at 25 cm from the target) there is a marked improvement of the energy resolution also in this case.

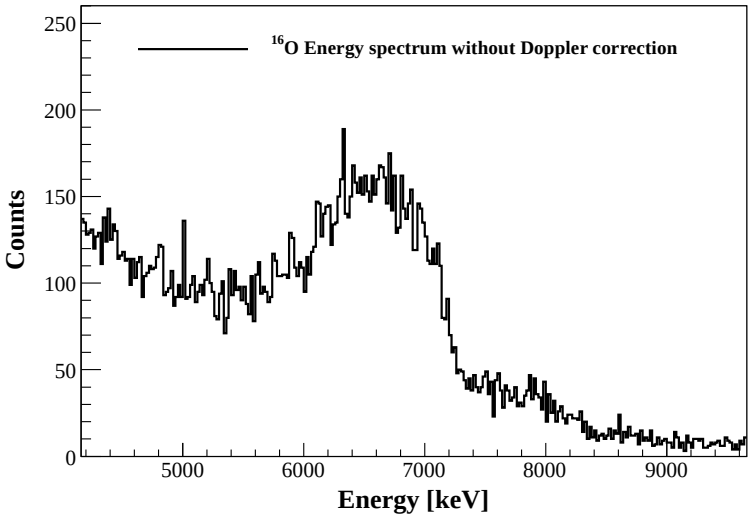

(a)

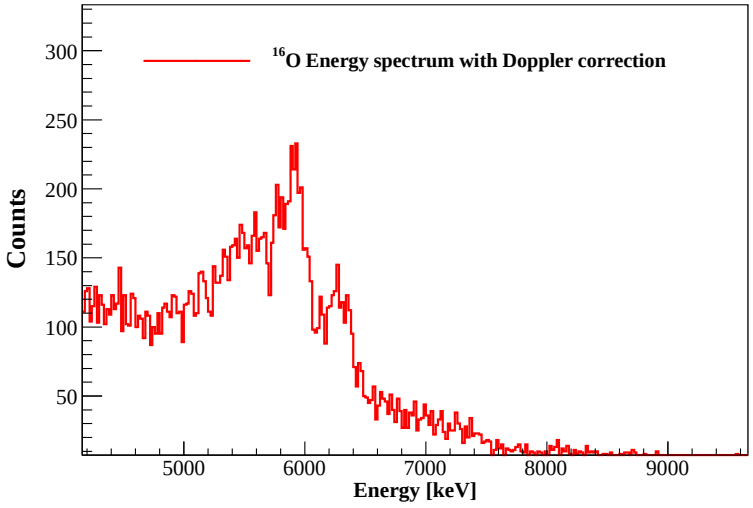

(b)

Figure 4.15: Energy spectra of the γ-rays measured in coincident with the ^{16}O reaction channel for one of the HECTOR^{+} detector. The (a) panel shows the spectrum without Doppler correction while the (b) panel is the spectrum with the Doppler correction.

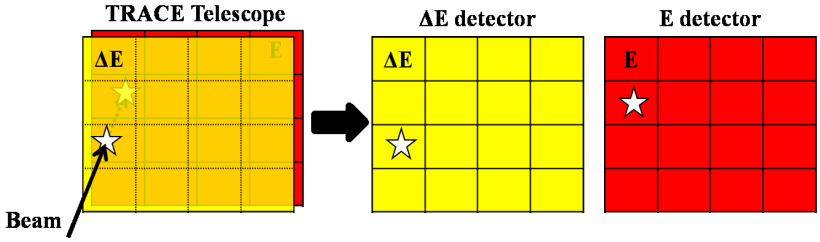

Figure 4.16: Schematic view of scattered ion that lost its energy in a ΔE pads, marked with a star, and that it stopped in the neighbour E pad of the "standard" E pad.

4.6 Silicon Neighbour Configurations

As explained in sec. 3.1 the TRACE telescope was composed by two segmented silicon detectors mounted inside the scattering chamber. Due to the no-spherical geometry of these detectors and the reaction kinematics, we have noticed that if we considered only the "standard" ΔE-E combination of pads, for which a ΔE pad is combined with the E pad behind it, a number of "good" events would be lost. Indeed, the scattered ions that lost their energy in a ΔE pads, are not necessary stopped in the corresponding E pad, as shown in Fig. 4.16. This effect has to be taken into account in order to increase the statistics of our experiment. For these reasons, all the possible combination of ΔE-E pads (named "silicon neighbour" combinations) have been considered and we have verified that the corresponding ΔE-TKE matrix made sense. In Fig. 4.17 are shown the results for a configuration of silicon pads in which a ΔE pad is associated with the E pad directly below the "standard" one. The green pad are the ones for which the corresponding ΔE-TKE matrix made sense, see Fig. 4.18. As can be seen from Fig. 4.18 ΔE-TKE matrix generated by this combination of pads has the typical ΔE-TKE matrix shape. Also in this case, a clear separation between ions from Boron to Fluorine is visible and there is a good mass separation. It is clear that, if we think at the geometry and the reaction kinematics, the only pads involved in the configuration just described are the ones, coloured in green in Fig. 4.17, in the bottom part of the two telescopes. By considering all the possible silicon neighbour combinations, the statistics have been increased by approximately $\sim 20\%$.

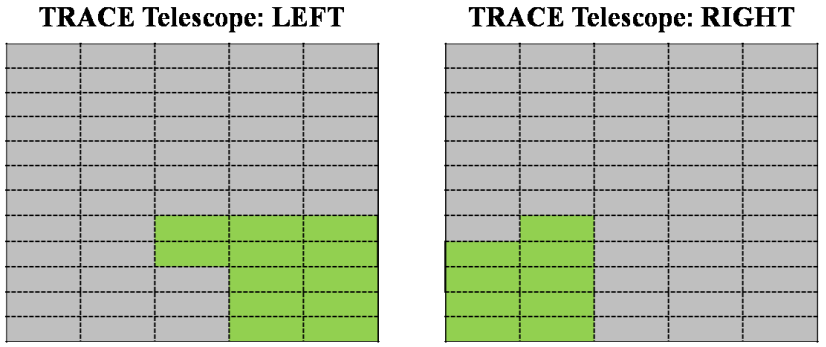

Figure 4.17: Results for a configuration of silicon pads in which a ΔE pad is associated with the E pad directly below the "standard" one. The green pads are the ones for which the associated ΔE-TKE matrix made sense, see. 4.18

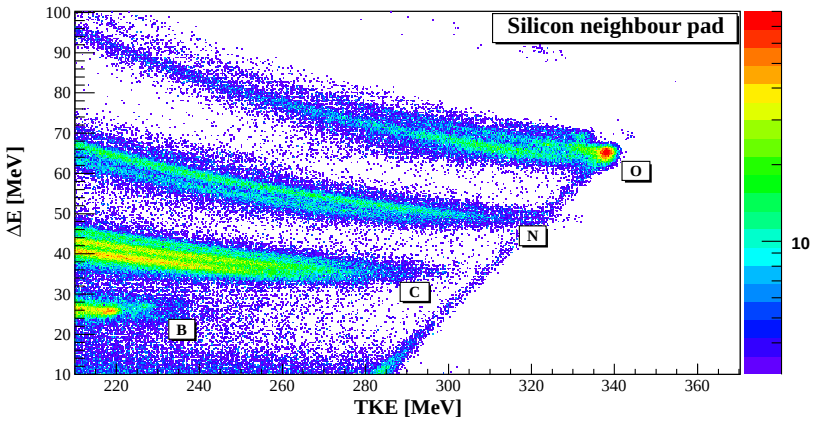

Figure 4.18: ΔE-TKE matrix in the case of a silicon neighbour combination of pads.

4.7 Correlation Between Gamma-rays and Scattered Ions

As described in sec. 4.4, the TRACE array was used, in our experiment, to select the inelastic scattering channel of the ^{17}O. Another key features of this array is the possibility to used it with the AGATA or the HECTOR$^+$ arrays in order to select transitions to a given state of the excited nucleus. This can be done correlating the γ-ray energy, measured with the AGATA or the HECTOR$^+$ array, with the excitation energy transferred to the target nuclei. This latter quantity can be measured as the Total Kinetic Energy Loss (TKEL) of the projectile, that is the difference between the Total Kinetic Energy (TKE) measured in an event and the energy corresponding to an elastic scattering event.
After the selection of the inelastic scattering channel, see sec. 4.4, all the events can be used to construct a coincident matrix of the measured decay energy (E_{AGATA} or E_{HECTOR^+}) versus the excitation energy (TKEL), see Fig. 4.19. In these matrix, γ-ray transitions occur as horizontal lines thanks to the better energy resolution of the AGATA/HECTOR$^+$ arrays compared to the energy resolution of the TRACE telescopes. The transition to a given state of the nucleus are located on diagonal lines. Hence, by applying diagonal gates on these matrix, decays into a define final state of the nucleus can be selected and the corresponding γ-ray spectra can be generated and analysed. Since we are interested to select the ground-state decays, a diagonal gates on these matrix have been performed, as shown by the diagonal regions in Fig. 4.19. It has to be noticed that, due to the not so good energy resolution of the TRACE telescopes, the diagonal cuts have a width of $\pm$1 MeV. In principal this gating condition should exclude both the gamma decay from higher lying states (see in the bottom right part of the matrix) and the γ-rays corresponding to a random coincidence with an elastic scattering event (vertical structure in the top part of the matrix).

Fig. 4.20 shows the energy spectrum measured with the AGATA array, (a) panel, and the HECTOR$^+$ array, (b) panel, under different gating conditions. The black spectrum is obtained without any gate condition while the blue one is the energy spectrum of the γ-rays detected in coincidence with the scattered ^{17}O ion. Since both spectra are normalized to the total number of counts, it is clear how the selection of the ^{17}O scattering channel enhances the intensity of the ^{124}Sn

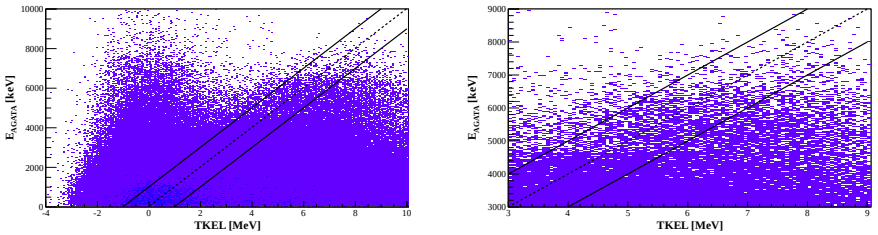

(a) AGATA-TRACE matrix

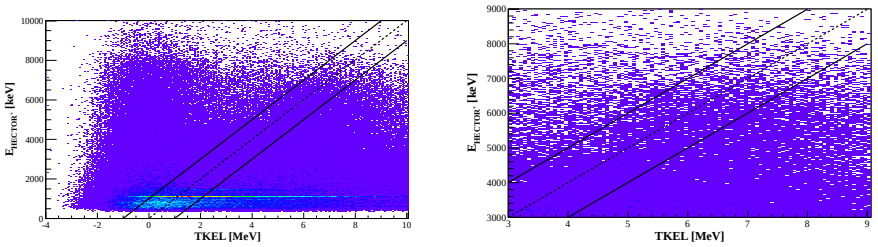

(b) HECTOR^{+}-TRACE matrix

Figure 4.19: Scattered plot showing the γ-ray energy of the ^{124}Sn, measured by the AGATA array in the (a) panel and HECTOR^{+} array in the (b) panel, versus the TKEL, measured by the TRACE telescopes. The diagonal gate for the selection of the ground-state decays is mark by the solid black lines.

transitions. The red spectrum is the energy spectrum with the additional diagonal gate condition as explained above. It is evident how the transition corresponding to the ground-state decay of the 2^+ states are further enhanced compared to the blue spectrum. Fig. 4.21 shows the level scheme of the ground-state decays, red solid lines, of ^{124}Sn observed in our experiment. However, due to the poor energy resolution of the TRACE telescopes, some gamma decays from higher lying states are still present (i.e. E_γ=1471 keV, black solid line in Fig. 4.21).

4.8 Gamma Decay from the Pygmy Dipole Resonance

4.8.1 Background subtraction

Due to the limited energy resolution of the TRACE telescopes, some gamma decay from higher lying states are still present in the γ-ray energy spectrum generated with the diagonal gate described in sec. 4.7. In order to obtained an energy spectrum free from these decays, a background subtraction has been performed. Since this background comes from high lying states, we applied a diagonal gate on the γ-TKEL matrix in order to select the decays from these states into the first excited state at 1131.7 keV. In Fig. 4.22 are shown the diagonal gates for the selection of the background marked by the solid black lines in the γ-TKEL matrices for the AGATA array and the HECTOR$^+$ array.

Fig. 4.23 shows the energy spectrum, in the energy range of the PDR decay, measured by the AGATA array ((a) panel) and the HECTOR$^+$ array ((b) panel) gated on the background diagonal cut depicted in Fig. 4.22. As can be seen in the background energy spectra no evident structures are present and its decay seems to be more of statistical exponential nature in the PDR region.

The background spectra generated as described above have been subtracted to the energy spectra of the ground-states decays, in order to obtain a clean energy spectra of the gamma decay from the PDR states. The results are shown in the following section.

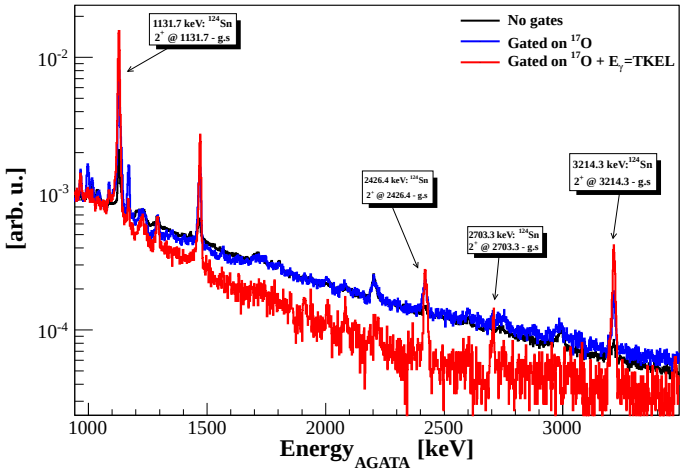

(a) AGATA energy spectrum

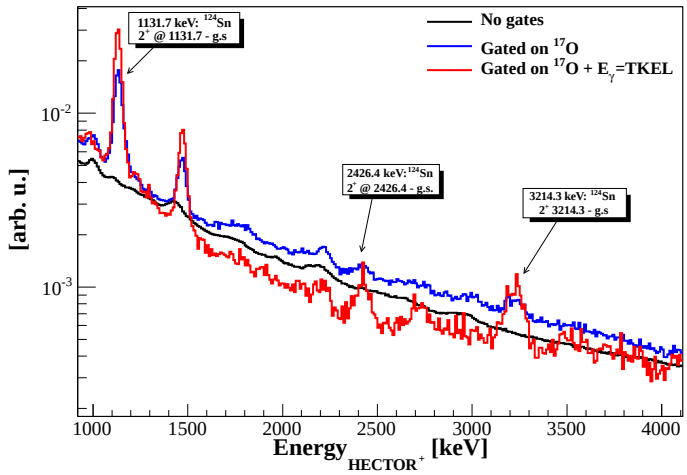

(b) HECTOR$^+$ energy spectrum

Figure 4.20: AGATA ((a) panel) and HECTOR$^+$ ((b) panel) and energy spectrum under different gating conditions: the black spectrum is without any gate, the blu spectrum is gated on the ^{17}O scattering channel and on the coincidence peak of the time spectrum, and the red one has the additional diagonal gates shown in Fig. 4.19.

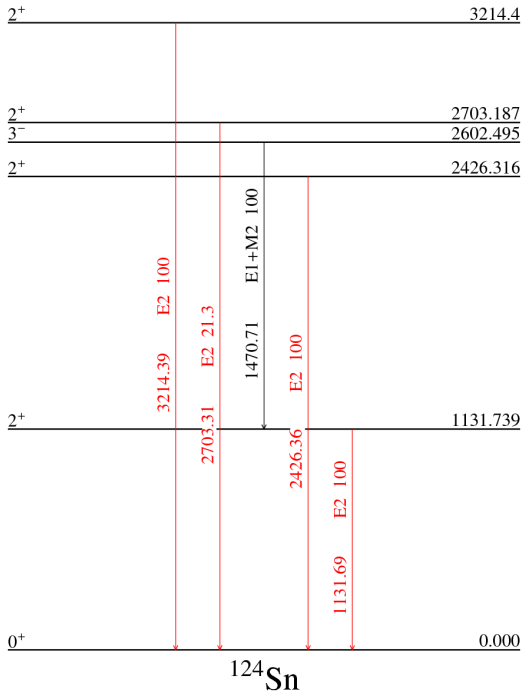

Figure 4.21: Level scheme of the the ground-state decays, red solid lines, of ^{124}Sn observed in our experiment, see 4.20 . Due to the poor energy resolution of the TRACE telescopes, some gamma decays from higher lying states are still present (i.e. E_γ=1471 keV, black solid line)

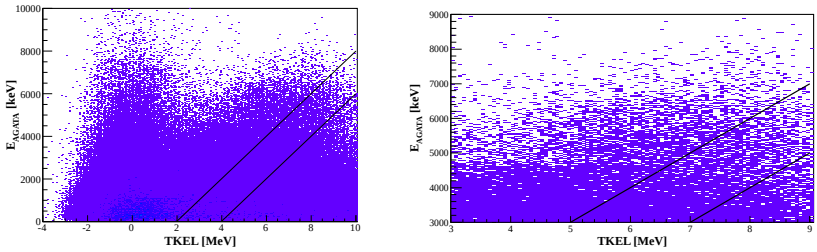

(a) AGATA-TRACE matrix

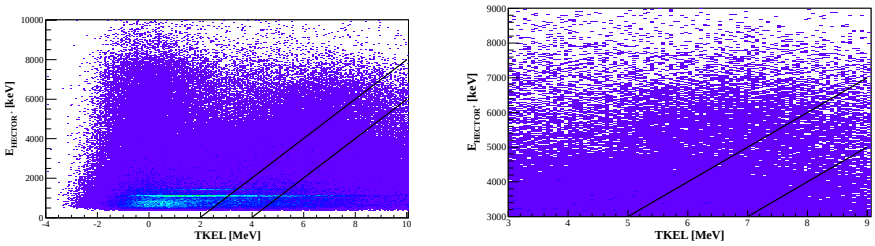

(b) HECTOR^{+}-TRACE matrix

Figure 4.22: Scattered plot showing the γ-ray energy of the ^{124}Sn, measured by the AGATA array in the (a) panel and HECTOR^{+} array in the (b) panel, versus the TKEL, measured by the TRACE telescopes. The diagonal gate for the selection of the background is mark by the solid black lines.

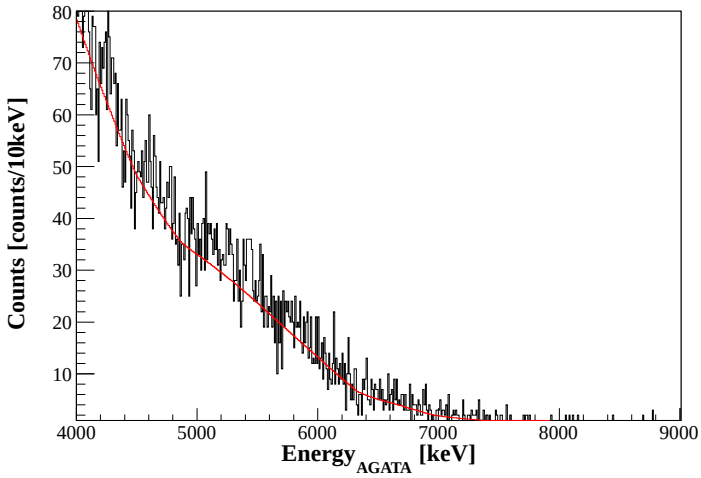

(a) AGATA energy spectrum

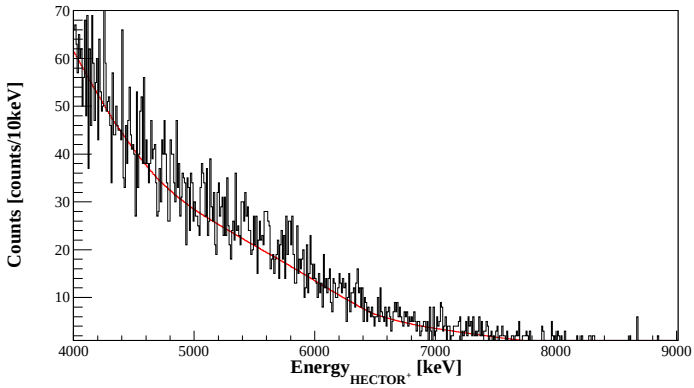

(b) HECTOR$^+$ energy spectrum

Figure 4.23: AGATA ((a) panel) and HECTOR$^+$ ((b) panel) and energy spectrum gated on the background diagonal cuts shown in Fig. 4.22.

4.8.2 Pygmy Dipole Resonance Decay

As mentioned in sec. 1.3, the PDR is composed by a number of discrete states of $J^{\pi}=1^{-}$ nature, whose dominant decay channel is towards the 0^{+} ground-state. In order to measure the gamma decay from the PDR, the ^{17}O inelastic scattering channel have to be selected, a gate on the time spectrum have to be performed as well as request that the γ-ray energy have to be equal to the TKEL within detector resolution, as explained in sec. 4.7. In order to subtract the Compton continuum and the escape peaks present in the energy spectra, a procedure named "unfolding" could be applied to the experimental energy spectrum, see Appendix B. Unfortunately, in our case, this procedure could not be applied due to the low statistics in the PDR region but it has been applied on the other nuclei measured in our experiment (^{208}Pb, ^{90}Zn and ^{140}Ce). However, a background subtraction, as described in sec. 4.8.1, have been performed. Furthermore, since the typical lifetime of these states is of the order of femtoseconds, a Doppler correction for the recoil has been also applied (see sec. 4.5.1). Fig. 4.24 shows the γ-ray energy spectrum of the ^{124}Sn in the PDR decay region obtained with these condition for the AGATA ((a) panel) and the HECTOR^{+} ((b) panel) arrays. As can be seen from these spectra, a large fragmentation of the dipole strength is observed and for this reason the clear identification of the transition is difficult, only the stronger transitions can clearly be identified. The coloured lines mark the energy at which PDR transitions have been measured with photon ([64]) and alpha ([65]) scattering experiments. The blue and red lines correspond to known E1 transitions we observed (the dashed ones when the identification is not clear).

It has to be noticed that the structure of the γ-rays from the PDR measured by the two γ-ray detector arrays is similar. Note that the efficiency at high energy is higher for the $LaBr_3$:Ce detectors but still the states in this region are not populated. This confirm that the states above 7 MeV are not populated via inelastic scattering of ^{17}O.

4.9 Giant Quadrupole Resonance

Since the inelastic scattering of ^{17}O at 20 MeV/u is expected to populate strongly the giant resonance region of the target nuclei, it was interesting to investigate

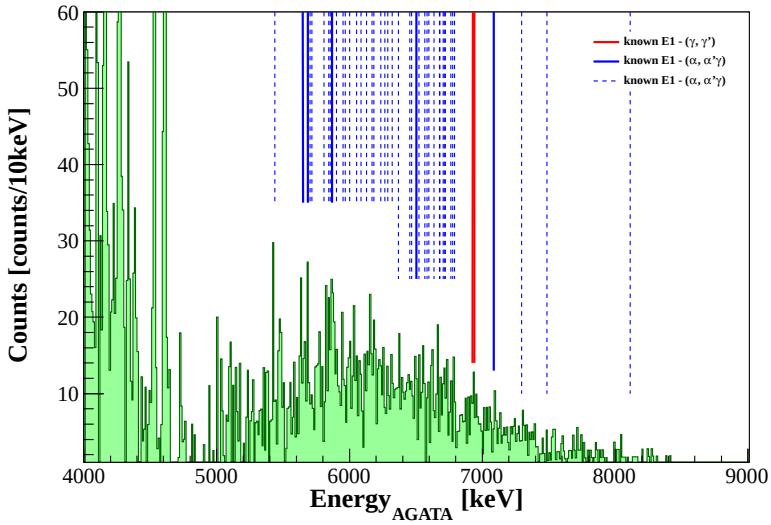

(a) AGATA energy spectrum

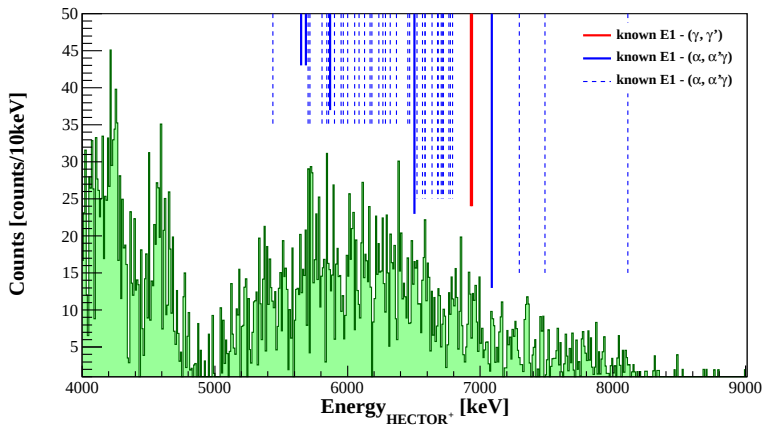

(b) HECTOR$^+$ energy spectrum

Figure 4.24: AGATA ((a) panel) and HECTOR$^+$ ((b) panel) energy spectrum of the ^{124}Sn in the PDR region with the gating conditions described in the text.

Resonance	Multipolarity	Energy [MeV]	FWHM [MeV]
ISGQR	2	12.3	3.1
ISGMR	0	14.0	3.8

Table 4.2: Multipolarity, centroid energy and FWHM of the IsoScalar Giant Monopole and Quadrupole in ^{124}Sn taken from [66].

this excitation in our experiment. The energy spectra of the inelastic scattered ^{17}O ions are expected to show strong peaks above the separation energy. Indeed the excitation energy transferred to the target is measured by the Total Kinetic Energy Loss (TKEL) of the projectile, that is the difference between the Total Kinetic Energy (TKE) measured in an event and the energy corresponding to the elastic scattering event.
Fig. 4.25 shows the excitation spectra in the Giant Resonance region for the ^{124}Sn. The bump arising from the excitation of the giant resonance region is clearly visible and it has been fitted with a simple Gaussian to show that the centroid energy measured in our experiment is 12.4 MeV and it is close to the known energy of the ISGQR (12.3 MeV). The width is, however, larger (4.8 MeV) then the predicted one (3.1 MeV) this is probably due to the fact that the ISGQR is not the only giant resonance to be populated in the reaction and the peak in Fig. 4.25 could be the result of the partial superimposition of more than one resonance. The reference values are reported in Table 4.2.

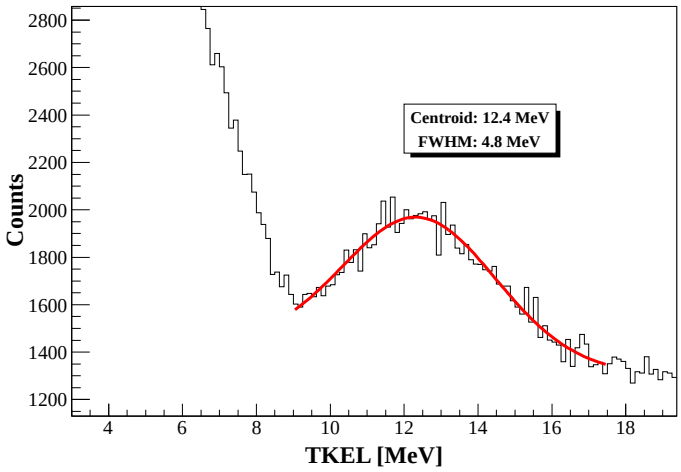

Figure 4.25: Energy spectrum of the scattered ^{17}O ions measured with ^{124}Sn target. The peak is due to the population of the ISGQR.

Chapter 5

Experimental Results

Following the procedure described in chap. 4, the experimental results of the experiment described in this thesis are given and discussed in this chapter. In particular, the determination of the mutlipolarities of the PDR transitions is described in sec. 5.1 and a comparison of the measured intensities of the observed transitions to the B(E1) value reported in literature has been, also, performed in sec. 5.2. Furthermore a determination of the differential cross section of the PDR transitions is presented in sec. 5.3.

5.1 Determination of The Multipolarities

As discussed in sec. 1.3 the Pygmy Dipole Resonance is a concentration of $J^{\pi}=1^{-}$ states around the particle threshold. The investigation on the multipolarties of these transitions has been performed taking advantage of the angular distribution of the emitted γ-rays.

The angular distribution associated with an electromagnetic transition from a state $|J_i\rangle$ to a state $|J_f\rangle$ is given by:

$$W(\theta) = \sum_{m_j,\mu} |\langle J_i m_i \lambda\mu | J_f m_f\rangle|^2 P(m_i) Z_{\lambda\mu}(\theta) \tag{5.1}$$

where $P(m_i)$ is the population probability of each magnetic component m_i of the initial state, and $Z_{\lambda\mu}(\theta)$ is the angular distribution of the photons of multipolarity

λ with component μ, which can be calculated exactly (see [67]). In absence of specific constraints all the possible magnetic substates m are equally populated, so there is no alignment. In some cases, as in the present of magnetic fields or in the case of states formed in nuclear reactions, some substates are selected in a privileged way, therefore giving a certain alignment to the nuclear spin. The excited states formed in nuclear reactions are generally oriented with respect to the beam direction and the degree of orientation depends on the formation process and on the reaction mechanism. For these reasons we expected a certain degree of alignments in our experiment.

Exploiting the position sensitivity of the AGATA Demonstrator and TRACE arrays it is possible to obtain almost continuous angular distributions. The AGATA Demostrator has been treated as a continuous HPGe detector and for each γ-ray the angular position of the first interaction point with respect to the recoil direction has been considered.
Qualitatively, the multipolarity can be identify by comparing the γ-ray energy spectrum gated on the angular distribution of the emitted γ-rays. Indeed, if we put a gate on the angular distribution, see Fig. 5.1, it is possible to identify the E1 and E2 component in the γ-ray spectra. Fig. 5.2 shows the comparison between the γ-rays spectra of ^{124}Sn in the PDR energy region. The red spectrum is gated on 65°-115°angular range in order to enhanced the E1 transitions while the blue spectrum is gate on 0°-65°and 115°-180°angular range to enhanced the E2 transitions. The PDR transitions are clearly enhanced in the red spectrum, showing as expected an E1 behaviour.

The same analysis described above has been also performed with the HECTOR$^+$ array. In this case the angular range has been define as the angle between the recoil direction and the center of the $LaBr_3$:Ce crystals in which the emitted γ-ray has been detected. Fig. 5.3 shows the spectra obtained by gating on different angular range as described above. The PDR region shows an E1 character also in this case but thanks to the PSA and tracking algorithms a much better discrimination between the E1 and the E2 component is achieved with the AGATA Demonstrator array.

In order to better evaluate the multipolarity of the PDR transitions we decided

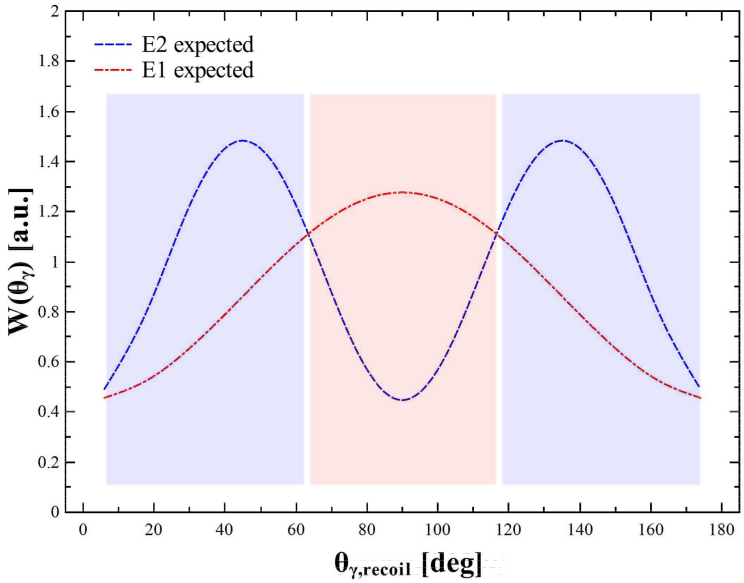

Figure 5.1: Expected angular distributions for an E1, red dashed line, and E2, blue dashed line, transition. The highlighted blue and red region represent the angular gate used to enhanced the E2 and E1 transitions respectively.

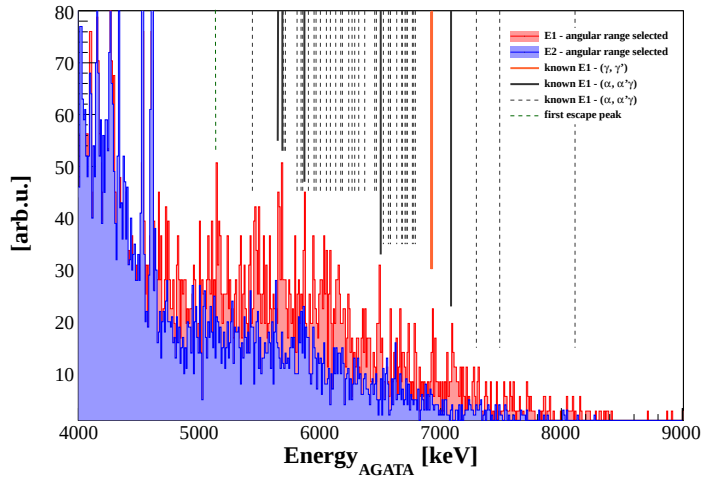

Figure 5.2: γ-rays spectra of ^{124}Sn in the PDR energy region measured with the AGATA Demonstrator. The red spectrum is gated on 65°-115°angular range in order to enhanced the E1 transitions while the blue spectrum is gate on 0°-65°and 115°-180°angular range to enhanced the E2 transitions.

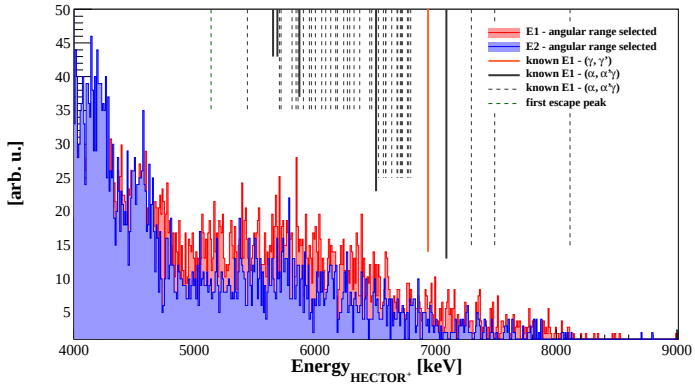

Figure 5.3: γ-rays spectra of ^{124}Sn in the PDR energy region measured with the HECTOR$^+$ array. The red spectrum concerns the angular range 65°-115°in order to enhanced the E1 transitions while the blue spectrum concerns the angular range 0°-65°and 115°-180°to enhanced the E2 transitions.

to focused on the events detected by the AGATA Demonstrator array, thanks to the better position sensitivity achieved with this array. We considered the angular range between 0°and 180°and we simulated the efficiency for each angle of a γ-ray at the energies needed for our analysis. We have then measured for each angle the intensity of the different transitions in the ^{124}Sn spectrum and the results have been divided by the efficiency at the considered energy. In this way, the angular distribution for each transitions of interest has been extracted, see Fig. 5.4. In (a) panel the known E2 transition from the first 2^+ excited state at 1132 keV to the ground state is depicted with blu squared and the black circles represent the angular distribution of the region between 4 and 5 MeV that has several known 2^+ states. In (b) panel the known E1 transition at 1471 keV from the first 3^- excited state to the first 2^+ excited state at 1132 keV is depicted with red squared and the black circles represent the angular distribution of the PDR region between 6 and 7 MeV. As can be noticed all the angular distributions follow the expected trend. It has to be pointed out that, due to the low statistics of the recoil detected in the left pad of the TRACE telescopes, the angular distributions between 90°and 180°is dominated by statistical fluctuations.

The ratio between the number of counts in the 65°-115°angular range over the number of counts in the 15°- 65°angular range for different transitions has been evaluated. Fig. 5.5 shows these ratio: the horizontal red region corresponds to E1 expected angular distribution and the blue one to E2 distribution. As can be seen from Fig. 5.5 the PDR region shows, as expected, an E1 behaviour.

5.2 Dipole Strength

The investigation of the angular distribution described in sec. 5.1 of several energy ranges up to 9 MeV clearly proves the E1 character of the strength in the PDR region. As mentioned in sec. 1.3, while almost all $J^\pi=1^-$ states have been excited and observed up to 6.8 MeV in (α, $\alpha'\gamma$) [65], as well as in (γ, γ'),[64] reactions, the intensity drop off significantly for higher energies in the case of (α, $\alpha'\gamma$) reaction. Between 7 and 8 MeV only a few states are excited in the case of α-scattering experiments while a high concentration of $J^\pi=1^-$ states with large B(E1)$\uparrow$ values has been observed in (γ, γ') experiments. This splitting of the dipole strength has been observed in different nuclei and could be explained as a different under-

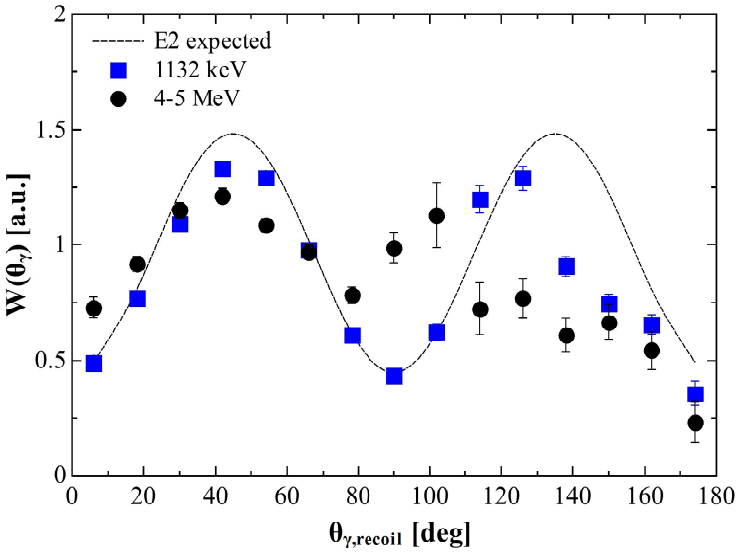

(a) E2 angular distribution

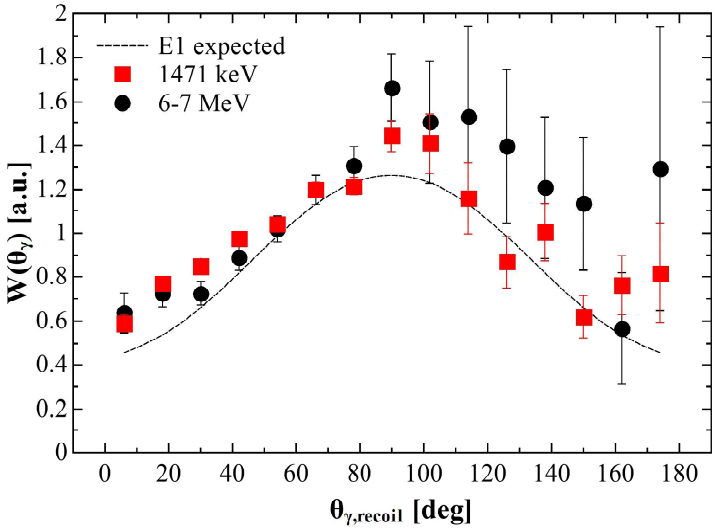

(b) E1 angular distribution

Figure 5.4: Absolute angular distributions for different E1 ((b) panel) and E2 ((a) panel) transitions of ^{124}Sn.

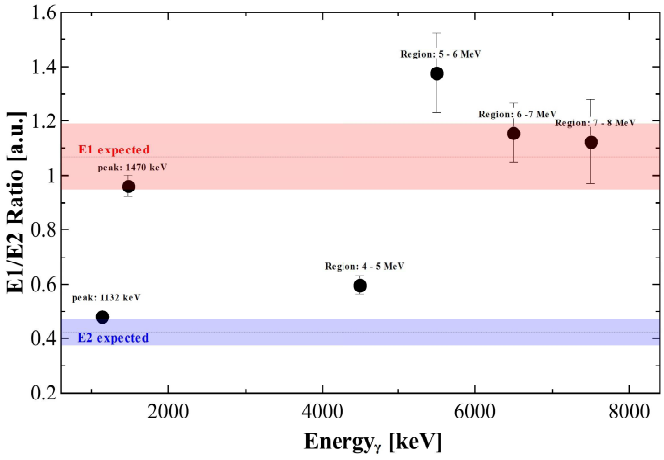

Figure 5.5: Ratio between the number of counts in the 65°-115°angular range over the number of counts in the 15°- 65°angular range, measured with the AGATA Demonstrator, for different transitions of ^{124}Sn. The horizontal red region corresponds to E1 expected angular distribution and the blue one to E2 distribution.

ling structure of these low-lying E1 states. The low-energy group of states has a strong isoscalar component while the high-energy group of states has a stronger isovector component. In order to better understand this phenomenon the complete ground-state decay spectrum, measured with the AGATA Demonstrator and the HECTOR$^+$ arrays, has been deduced in bins of 100 keV width after subtracting the contribution of random coincidence and the feeding from the excited states as described in sec. 4.8. The results are shown in Fig. 5.6 and compared to the one obtained in the (α, $\alpha'\gamma$) experiments, in pink, and in the (γ, γ') experiments in blue. The low-energy part, below 7 MeV, of the resonance is equally excited by heavy ions, alphas and photons, while the high-energy part, above 7 MeV, is weakly excited by ions and alphas. The strength in peaks for the two different energy region, below and above 7 MeV, is shown in Fig. 5.7. Also from this figure, it could be deduced that the strength measured in the (γ, γ') experiment are almost equal in both energy ranges, which it is not the case in our experiment and in the (α, $\alpha'\gamma$) experiments. We can therefore say that the inelastic scattering of ^{17}O at 20 MeV/u was successfully used to measure the gamma decay from the PDR states of

γ-ray energy [keV]	Multipolarity	B(Eλ)$\uparrow$ [W.u.]
1131.7	E2	9.0
3214.4	E2	1.5
3761.8	E2	0.3
5500-7000	E1	0.22
7000-9000	E1	0.08

Table 5.1: Known B(Eλ)$\uparrow$ used for the cross sections calculation performed with the FRESCO code as described in Appendix C. The data were taken from [68] and [64].

^{124}Sn, and that the results point to the presence of a splitting of the PDR similar to what has been observed with the (α, $\alpha'\gamma$) technique.

5.3 Determination of Differential Cross Section

As already mentioned, by comparing results of photon, alpha and heavy ions scattering experiments, a clear selectivity in the population of these PDR states has been observed. It is thought that this splitting reflects a different underlying structure: the low-energy states are of isoscalar nature and their transition density is peaked on the surface, while the high-energy states are of isovector nature and are associated to a transition towards the IVGDR. While the photons in the (γ, γ') experiments interact with the nucleus as a whole based on the electromagnetic interaction, the heavy ions in our experiments are predominately isoscalar hadronic probes with an interaction located at the surface of the nucleus. Because of the different interaction depth of the probes within the nucleus, the excitation of the states with different radial transition densities is strongly affected. In order to better understand the character of these states, the excitation cross sections calculated with the FRESCO code and the cross sections measured in our experiment have been compared.
The cross sections for the given kinematic conditions have been calculated with the FRESCO code, see Appendix C, based on the known B(Eλ)$\uparrow$ values, reported in Table 5.1.

In principal, the differential cross sections obtained from the DWBA calculation

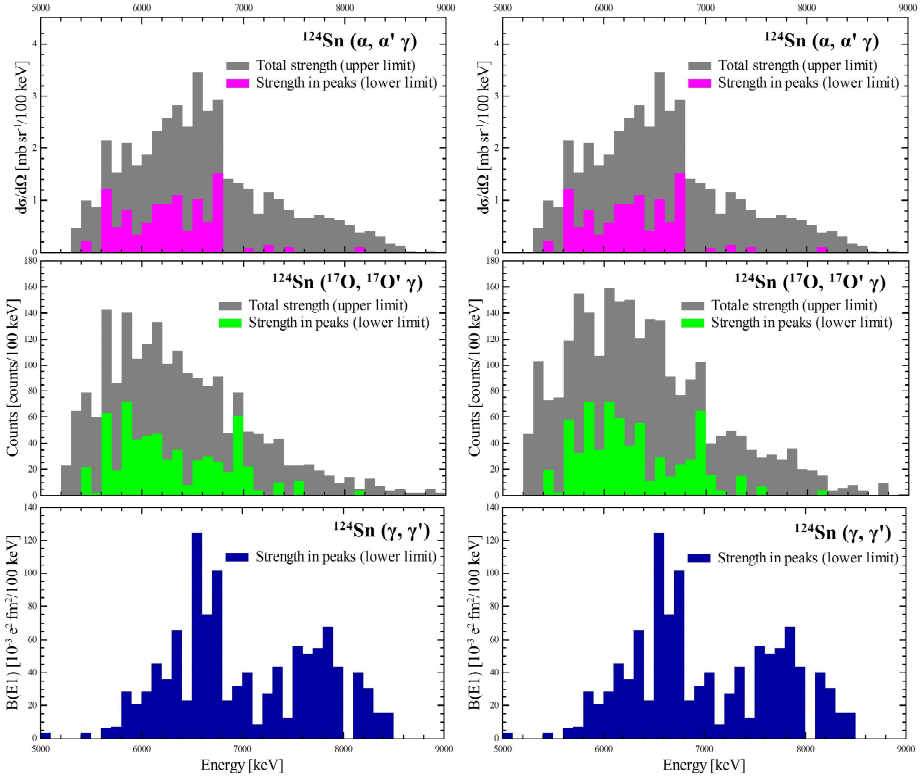

(a) AGATA array

(b) HECTOR$^+$ array

Figure 5.6: Complete and in peaks ground-state decay spectrum, measured with the AGATA Demonstrator ((a) panel) and the HECTOR$^+$ ((b) panel) arrays, in bins of 100 keV (depicted in green). The blue and the pink graphics are the strengths measured in photon and alpha-scattering respectively.

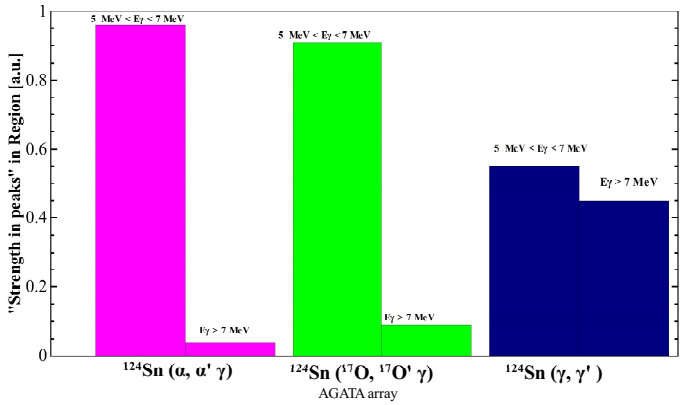

(a) AGATA array

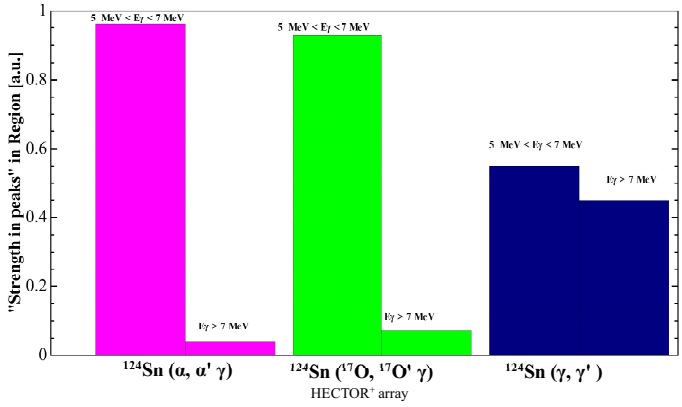

(b) HECTOR$^+$ array

Figure 5.7: Ratio of the strength in peaks evaluated in the two energy region, below and above 7 MeV, for the three experiments.

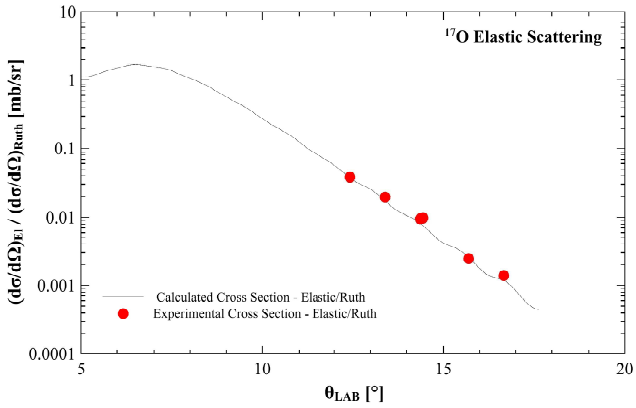

Figure 5.8: Experimental cross sections for the elastic scattering measured in (^{17}O, ^{17}O'γ) experiment, black circles. The dashed line represent the calculated cross section with the FRESCO code.

should be compared to the experimental cross sections, obtained from the spectra as

$$\frac{d^2\sigma}{dEd\Omega} = \frac{N_\gamma(E)}{\epsilon(E)N_{beam}N_{target}d\Omega} \tag{5.2}$$

where $N_\gamma(E)$ is the number of the γ-rays measured at an energy E, $\epsilon(E)$ is the absolute efficiency of the γ-ray detection array at the energy E (which should take into account also the angular distribution of the γ-rays), $d\Omega$ is the solid angle of the TRACE pads, N_{target} is the number of the target nuclei per unit surface and N_{beam} are the number beam nuclei that passed through the target during the whole measurement. Unfortunately, the latter term could not be evaluated, because no calibrated faraday cup was available for use as a beam dump. For this reason we have normalized the values of the experimental cross section in the case of the elastic scattering on the cross section value calculated with the code. This normalization factor has been used for the calculation of the cross section of the other states of interest. Fig. 5.8 shows the Elastic over Rutherford cross section as a function of the scattering angle. The experimental results have been normalized to the calculated cross section in this case.

In order to prove the reliability and the accuracy of our calculation the compari-

son between the experimental and the calculated cross sections for different excited states has been evaluated. It has to be pointed out that all the experimental cross sections have been corrected for the intrinsic efficiency of the AGATA array and for the ^{17}O-γ angular correlation. The uncertainties given for the cross sections take into account the uncertainties due to the statistics, the angular correlation (10%) and the AGATA array efficiencies (10%). The excited states considered were all 2^+ states at 1131.74 keV, 3214.36 keV and the sum of two states at 4528.8 keV and 4604.6 keV.

As explain in sec. 2.2.1 the deformed potential model was used with the FRESCO computer code in the Distorted Wave Born Approximation (DWBA). Nuclear transition potential for angular momentum transfer L are assumed as:

$$H_L^N(r) = -\delta_V(L)\frac{dV(r)}{dr} - i\delta_W(L)\frac{dW(r)}{dr} \tag{5.3}$$

In our calculations, the real and the imaginary deformation length are assumed equal: $\delta_V(L) = \delta_W(L) = \delta_L$. The Coulomb interaction is represented in the form of a multipole expansion between a point charge and a uniformly charged sphere with radius R_c, and can be written as:

$$H_L^c(r) = \frac{4\pi Z_p e}{2L+1}\left[B(EL)\uparrow\right]^{1/2}\begin{cases} r^L/R_c^{2L+1} & \text{se } r < R_c \\ 1/r^{L+1} & \text{se } r > R_c \end{cases}$$

where Z_p is the atomic number of the projectile and the $B(EL)\uparrow$ is the charge multipole moment. This model assumes that the deformation length of the transition potential is equal to that of the nuclear density distribution. The mass multipole moment can then be expressed as

$$B(L)\uparrow = \delta_L^2\left[\frac{3A}{4\pi}R^{L-1}\right]^2 \tag{5.4}$$

if a uniform distribution with radius R is assumed. It is possible to express the mass multipole in terms of the r^L radial moments of the neutron and proton transition densities as follow

$$B(L)\uparrow = |M_n + M_p|^2 \tag{5.5}$$

Since $B(EL)\uparrow = |M_p|^2$, it follows

$$\left|\frac{M_n}{M_p}\right| = \left[\frac{B(L)\uparrow}{B(EL)\uparrow}\right]^{1/2} - 1 \tag{5.6}$$

which is an indication of the isospin character for the excitation. For multipoles with $L \geq 2$, the deformation length δ_L corresponding to 100% of the isoscalar energy-weighted sum rule (EWSR) is given by the relation

$$\delta_L^2 = 2\pi\hbar^2 \frac{L(2L+1)}{3mAE_x} \tag{5.7}$$

where m is the nucleon mass, A is the mass number, and all the strength is assumed to be localized at an excitation energy E_x. The magnitude and shape of the differential cross section are dependent upon the magnitudes of nuclear and Coulomb amplitudes as well as their relative phase. For more details on the model see [34] and [69]. In the analysis describe in this thesis, the differential cross section for the 2^+ states was calculated using the $B(E2)\uparrow$ known from literature and reported here in Table 5.1. In order to verify the performances of the FRESCO calculations, the cross section for the first 2^+ state has been evaluated with different values of M_n/M_p. As can be observed from Fig. 5.9(a) the best value for M_n/M_p is N/Z in agreement with the pure isoscalar nature of this state. Since the calculations seem to be sensible to the value of M_n/M_p, for all the other 2^+ states the FRESCO calculations have been performed with the value $M_n/M_p = N/Z$ according to the nature of these states. Since the $B(E2)\uparrow$ of the states at 4.5-4.6 MeV has not yet been measured we decided to used the $B(E2)\uparrow$ of the highest 2^+ state known up to now (3761.83 keV). Due to the nature of these states the $B(E2)\uparrow$ of the excited states at 3761.83 keV has to be almost similar to the real one for the two states considered in our case. Fig. 5.9 shows the experimental cross section for the known E2 transitions of the ^{124}Sn. It is clear from Fig. 5.9 that the differential cross sections can be well reproduced by DWBA calculations using the deformed optical potential model transition densities. In addition the experimental data are clearly in agreement with the calculations remarking that the procedure used for the normalization is correct. In particular even the calculated cross sections for the two states around 4.5-4.6 MeV seem to reproduced the experimental data correctly, thing that validate our assumptions about the $B(E2)\uparrow$ used. It has to be noticed that it is the first time that these E2 γ-rays transitions have been measured with

γ-ray energy keV	$\frac{d\sigma}{d\Omega}$ mb/sr
5600-5800	0.58
5800-6000	1.22
6000-6200	0.95
6200-6400	0.50
6400-6600	0.42
6600-6800	0.45
6800-7000	1.22
7000-7200	0.19
7200-7400	0.10
7400-7600	0.99
8000-8200	1.44

Table 5.2: Cross sections for the excitation of $J^{\pi}=1^{-}$ states in ^{124}Sn via inelastic scattering of ^{17}O.

an hadronic probe.

Unfortunately, in the energy region of the PDR, statistics were insufficient for a quantitative analysis of the differential cross section of each single transition. For this reason the PDR transitions have been divided in two energy regions, below and above 7 MeV, and the cross sections integrated in these energy regions have been evaluated. Fig. 5.10 shows the results in the two energy regions. The FRESCO calculations were performed using the sum of the $B(E1)\uparrow$ of the 1^{-} states measured in the (γ, γ') experiment, [64]. In Fig. 5.10 the Coulomb and total cross sections calculated with the FRESCO code are reported. As can be observed the experimental cross sections for PDR transitions are larger compared to the expected calculated cross sections, especially for the low-energy states remarking the isoscalar nature of these transitions.

The differential cross sections for the identified $J^{\pi}=1^{-}$ states, integrated in bins of 200 keV, have been evaluated at the scattering angle $\theta_{^{17}O,Lab}$=13°. Fig. 5.11 shows the cross sections for the excitation of $J^{\pi}=1^{-}$ states in ^{124}Sn via inelastic scattering of ^{17}O measured in our experiment together with the experimental sensitivity limit. The relative data are reported in Table 5.2.

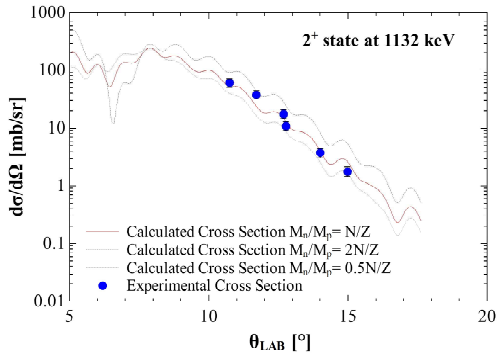

(a) 1132 keV

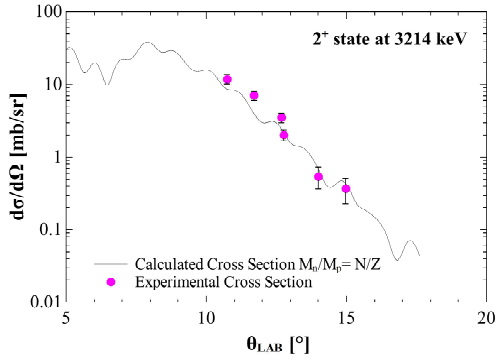

(b) 3214 keV

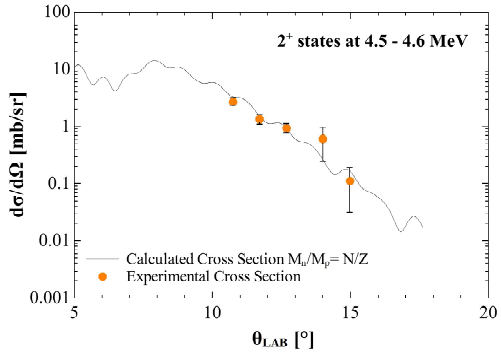

(c) 4.5 MeV

Figure 5.9: Experimental cross sections for the E2 transitions of ^{124}Sn measured in (^{17}O, ^{17}O'γ) experiment. The dashed line represent the calculated cross section with the FRESCO code.

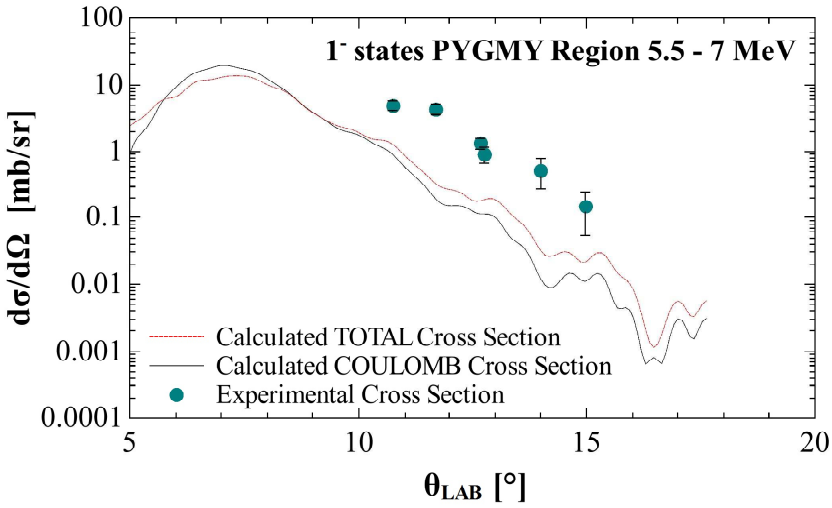

(a) PDR integrated region: 5.5 - 7 MeV

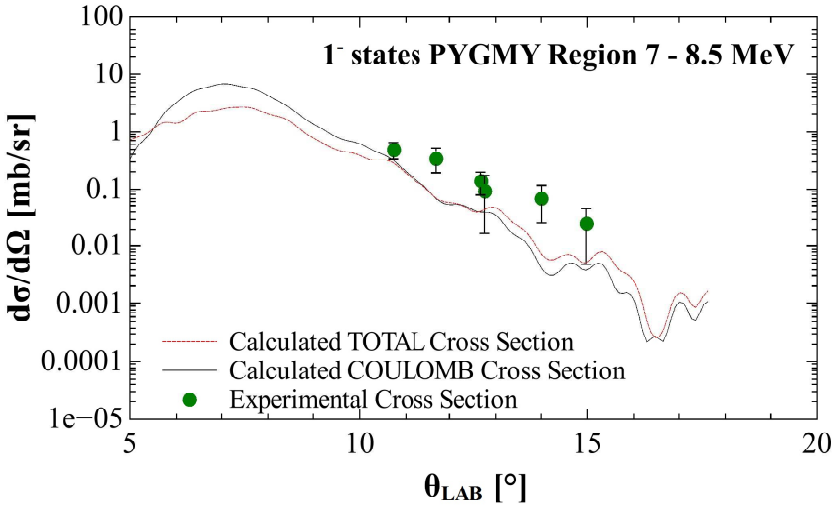

(b) PDR integrated region: 7 - 8.5 MeV

Figure 5.10: Experimental cross sections for the PDR transitions below ((a) panel) and above ((b) panel) 7 MeV of ^{124}Sn measured in (^{17}O, ^{17}O'γ) experiment. The dashed line represent the calculated Coulomb cross section with the FRESCO code, based on [64].

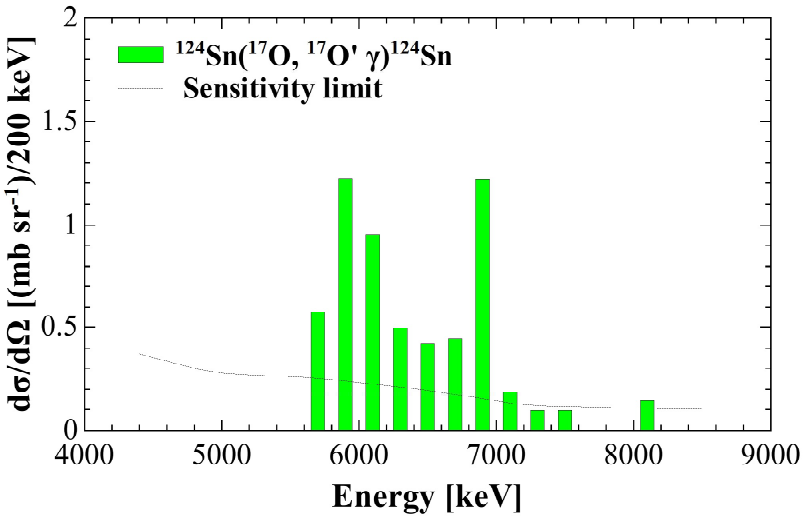

Figure 5.11: Cross sections for the excitation of $J^{\pi}=1^{-}$ states in ^{124}Sn via inelastic scattering of ^{17}O. The dashed black line represents the sensitivity limit.

In this analysis the experimental energy-dependent sensitivity limit, based on the background present in the spectra, has been evaluated with the following condition for the minimum peak area as follows:

$$A \geq \frac{1}{2p^2} + \sqrt{\frac{1}{4p^4} + \frac{2B}{p^2}} \tag{5.8}$$

where A in the peak area, B in the background and p the relative uncertainty of the peak area, $p = \frac{\Delta A}{A}$ that it is required to be smaller than $p \leq 0.7$ to be accounted for the analysis. Fig. 5.12 reports the same plot compared to the cross sections measured in the (α, $\alpha'\gamma$) experiment [65], pink plot, and the $B(E1) \uparrow$ strength distribution obtained in the (γ, γ') experiment [64], blue plot. It has to be pointed out that the cross section measured in the (α, $\alpha'\gamma$) experiment it refers to a scattering angle of $\theta_{\alpha}=3.5^{\circ}$.

In order to evaluate the nature of these $J^{\pi}=1^{-}$ states, the ratio of calculated excitation cross sections and the measured cross sections is define as:

$$\xi = \frac{(\frac{d\sigma}{d\Omega})_{Calculated}}{(\frac{d\sigma}{d\Omega})_{experiment}} \tag{5.9}$$

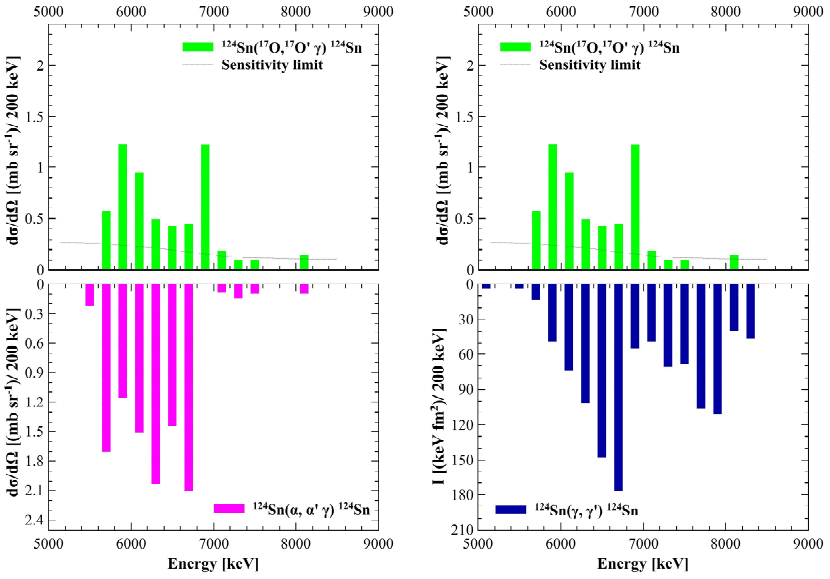

Figure 5.12: Cross sections for the excitation of $J^{\pi}=1^{-}$ states in ^{124}Sn via inelastic scattering of ^{17}O, green plot, compared to the cross sections measured in the $(\alpha, \alpha'\gamma)$ experiment [65], pink plot, and the B(E1) strength distribution obtained in the (γ, γ') experiment [64], blue plot. The dashed black line represents the sensitivity limit in our experiment.

Fig. 5.13 shows this ratio ξ. The (a) panel shows the ratio measured for the observed transitions integrated in the two energy regions below and above 7 MeV. The (b) panel shows the ratio measured for the observed transitions integrated in bins of 200 keV. In both panels the ratio for the states at 4 MeV is reported. The averaged value is 9% for the energy region between 5.5 and 7 MeV and 30% above 7 MeV. These results point out that the contribution of the Coulomb excitation in our experiment is negligible and the excitation of the $J^{\pi}=1^{-}$ states is dominated by the nuclear interaction. In addition the results shows the different underling structure of this PDR states, more isoscalar for the low-energy part and more isovector for the high-energy one.
Furthermore the ratio Δ define as:

$$\Delta = \frac{(\frac{d\sigma}{d\Omega})_{experiment} - (\frac{d\sigma}{d\Omega})_{Calculated}}{(\frac{d\sigma}{d\Omega})_{experiment}} \tag{5.10}$$

have been evaluated and compared to the one measured in the (α, α' γ) experiment [65]. In this case if the states is pure *isoscaler* the ratio Δ will be equal 1 otherwise if the ratio is equal to 0 the states is pure *isovector*. Fig. 5.14 shows the ratio Δ in (^{17}O, ^{17}O' γ), left panel, compared to the one for (α, $\alpha'\gamma$) experiment [65], right panel. The ratio Δ has been evaluated for the observed transitions integrated in bins of 200 keV. As can been seen, even this plot underling the more *isoscalar* nature of the observed transitions in our experiment as it has been observed in the (α, $\alpha'\gamma$) experiment.

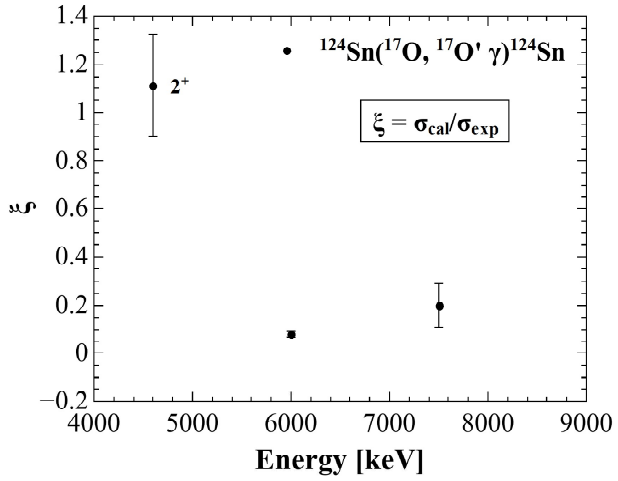

(a) PDR integrated in the two enery region: 5.5-7 MeV and 7-8.5 MeV

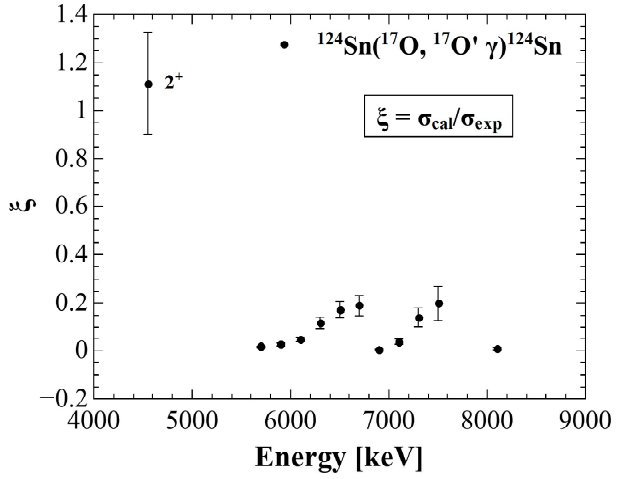

(b) PDR integrated in bin of 200 keV

Figure 5.13: Ratio ξ of the calculated and measured cross section in (^{17}O, ^{17}O' γ). The (a) panel shows the ratio measured for the observed transitions integrated in the two region below and above 7 MeV. The (b) panel shows the ratio measured for the observed transitions integrated in bins of 200 keV. In both panels the ratio for the states at 4 MeV is reported.

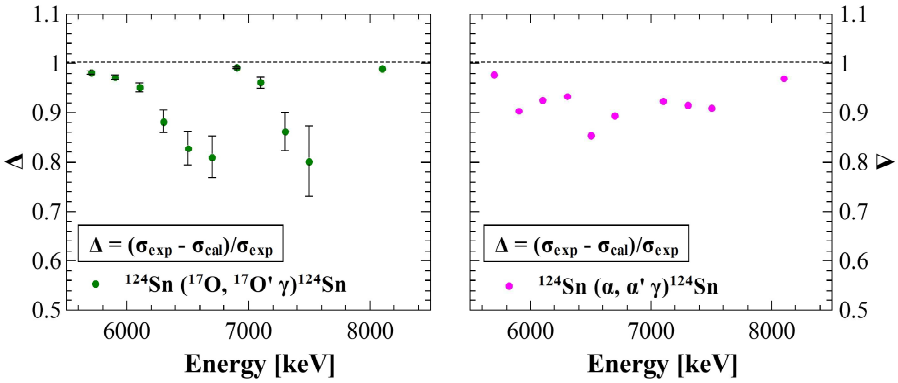

Figure 5.14: Ratio Δ in (^{17}O, ^{17}O' γ), left panel, and in (α, $\alpha'\gamma$) experiment [65], right panel. The ratio Δ has been evaluated for the observed transitions integrated in bins of 200 keV.

Conclusion

The understanding of the electric-dipole response around the binding energies is presently attracting considerable interest since there are still many open questions regarding its nature. For this reason, an experiment aimed at the study of the γ-decay from high-lying bound and unbound states in several nuclei (^{124}Sn, ^{208}Pb and ^{140}Ce) has been performed at Legnaro National Laboratories (LNL).
The giant resonance modes have been excited by inelastic scattering of ^{17}O beam at 20 MeV/u. The gamma-decay from such high-lying states has been measured with the AGATA Demonstrator array coupled to an array of 9 large volume $LaBr_3$:Ce scintillator detectors, named HECTOR$^+$. In order to identify the reaction channel, the beam like-ejectiles have been measured, in coincidence with the γ-rays, by two segmented silicon telescopes prototypes of the TRACE project mounted inside the scattering chamber.
The analysis described in this thesis has been focused on the studies of the Pygmy Dipole Resonance in the ^{124}Sn nucleus.
Thanks to the correlation between the γ-ray energy and the excitation energy transferred to the target nucleus it has been possible to identify the gamma decay of the PDR states to the ground state. The multipolarity of the observed gamma transitions has been determined with remarkable sensitivity thanks to angular distribution measurements and it has been shown that the γ-ray spectrum in the 5-8 MeV energy range is dominated by E1 transitions, consistently with the results of previous NRF experiments. Additionally, even it was not the main subject of this study, the gamma decay from the $J^\pi=2^+$ states and their corresponding cross sections have been investigated since these states have not yet been measured with hadronic probes. The experimental data have been compared to the cross section calculations performed with the FRESCO code in DWBA approximation based on

(γ,γ') data in literature.

Concerning the gamma decay from the PDR states, the measured intensities and the differential cross sections have been compared to the ones measured in (γ, γ') and (α, $\alpha'\gamma$) experiments. Similarly to what has been found using the (α, $\alpha'\gamma$) reaction, even in this case the results seem to indicate that there are two groups of states one with a more isoscalar character and the other with a more isovector nature. We can therefore say that the inelastic scattering of ^{17}O at 20 MeV/u was successfully used to measure the gamma decay from the PDR states of ^{124}Sn, and that the results point to the presence of a splitting of the nature of the PDR similar to what has been observed with the (α, $\alpha'\gamma$) technique. This observation represents further evidence for the splitting of the dipole response of the atomic nuclei which has been observed up to now also in ^{140}Ce, ^{138}Ba and ^{208}Pb. This is the first time such an effect has been measured in a different mass region and with heavy ions as a probe.

A deeper understanding of the nuclear structure properties of the low lying dipole strength and of the Giant Quadrupole Resonance requires systematic studies, in different region of masses. Concerning the stable nuclei the next experiments should be focused in different mass region (Zn, Sn, Ce, and Ba isotopes) in order to better understand the properties of this resonance as a function of the mass. The experimental set-up should be improved with respect to the energy resolution of the Silicon telescopes that can allow a better identification of the ground state decay of the PDR states. In addition the γ-ray efficiency detection should be improved by using the HECTOR$^+$ and AGATA array in their complete configurations. Finally, the experimental technique used in this work could be also used at future facilities (such as SPES), in order to study the structure of the PDR in more neutron-rich system in inverse kinematics at 20 MeV/u with solid, weakly bound targets such as ^{13}C.

Appendix A

Binary Reaction Kinematics

This appendix will discuss the kinematics of a binary interaction of the type:

$$a + A \longrightarrow b + B \tag{A.1}$$

where a is an incoming beam ion of mass m_a and velocity $\vec{v_a}$, A is a target nucleus of mass m_A, at rest in the laboratory frame of reference, and the reaction products are a lighter, beam-like ejectile b with mass m_b and velocity $\vec{v_b}$, and a heavier, target-like recoil B with mass m_B and velocity $\vec{v_B}$.
In sec. A.1 the expressions in the laboratory frame of reference for the quantities of eq. A.1 are calculated. Furthermore, formulas for the transformation of quantities between laboratory and centre-of-mass frames of reference are given in sec. A.2. For simplicity, only classical kinematics have been considered, neglecting relativistic effects.

A.1 Laboratory Frame of Reference

Fig. A.1 shows a schematic view of the bynary reaction in the laboratory frame of reference. The assuming that A is at rest, the laws of energy and momentum conservation imply that:

$$K_a = K_b + K_B \tag{A.2}$$

and

$$\begin{aligned} m_a v_a &= m_b v_b \cos\theta_b + m_B v_B \cos\theta_B \\ m_b v_b \sin\theta_b &= m_B v_B \sin\theta_B \end{aligned} \tag{A.3}$$

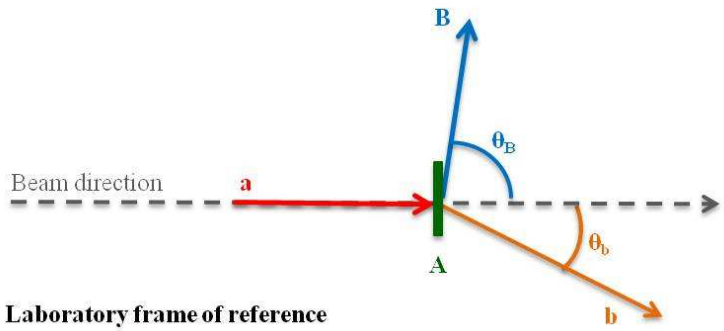

Figure A.1: Schematic view of a binary reaction in the laboratory frame of reference.

where the angles θ_b and θ_B are define in Fig. A.1; K_a, K_b and K_B are the kinetic energies of a, b and B respectively; Q is the Q-value of the reaction, that is the difference between the initial and final mass of the system:

$$Q = (m_a + m_A - m_b - m_B)c^2 - E_{ex} \tag{A.4}$$

where E_{ex} is the excitation energy transferred to the internal degrees of freedom of either nuclei. From eq. A.3, it is very easy to calculate that

$$\begin{aligned} \tan\theta_b &= \frac{\sin\theta_b}{\sqrt{\frac{m_a K_a}{m_b K_b}} - \cos\theta_b} \\ v_B &= v_b \frac{m_b \sin\theta_b}{m_B \sin\theta_B} \end{aligned} \tag{A.5}$$

Making use of eq. A.2 it is also possible to calculate the relation between K_b and θ_b for a given values of Q and K_a, but that is outside of our interest.

A.2 Centre-of-Mass Frame of Reference

In experimental nuclear physics, all observations take place in a reference frame that is at rest in the laboratory, referred to as the laboratory frame of reference. From the theoretical point of view, however, the motion of the centre of mass is of no consequence for the properties of a nuclear reaction. It is then often more convenient to use a moving coordinate frame in which the centre of mass of the

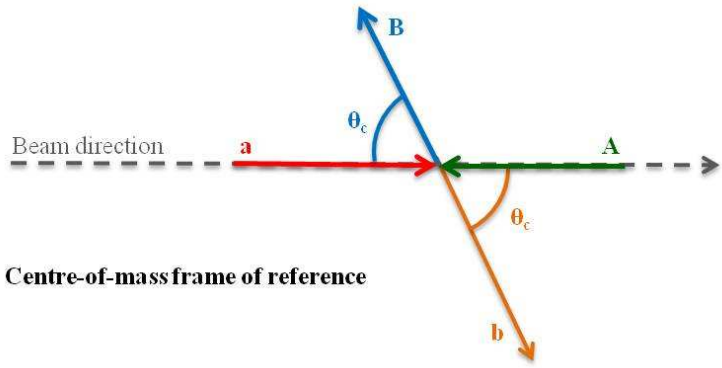

Figure A.2: Schematic view of a binary reaction in the centre-of-mass frame of reference.

two colliding nuclei is at rest, called the centre-of-mass coordinate system. In the centre-of-mass frame of reference, see Fig. A.2, both nuclei are moving towards each other with equal and opposite momenta:

$$m_a v'_a = m_A v'_A \tag{A.6}$$

where v'_a and v'_A are projectile and target speed in the centre-of-mass system. If v_{CM} is the speed of the centre of mass in the laboratory frame of reference, then by definition of centre of mass one has

$$v_{CM} = v_a \frac{m_a}{m_a + m_A} \tag{A.7}$$

meaning that the velocities of a and A in the centre-of-mass system are:

$$\begin{aligned} v'_a &= v_a - v_{CM} = v_a \frac{m_A}{m_a + m_A} \\ v'_A &= v_A - v_{CM} = -v_A \frac{m_a}{m_a + m_A} \end{aligned} \tag{A.8}$$

After the collision, b and B move in opposite direction in the centre-of-mass frame, due to momentum conservation, as shown in Fig. A.2; their direction forms an angle θ_c with the direction before the collision (that is the beam direction). This implies that

$$m_b v'_b = m_B v'_B \tag{A.9}$$

where v'_b and v'_B are the speeds of b and B in centre-of-mass system, related to the speeds in the laboratory system by:

$$\begin{aligned} v'_b \cos\theta_c &= v_b \cos\theta_b - v_{CM} \\ v'_b \sin\theta_c &= v_b \sin\theta_b \end{aligned} \tag{A.10}$$

It should be noted that, if the Q-value is non-zero, the velocity of the centre of mass changes between the initial and final state, with the relation:

$$v_{CM,f} = v_{CM,i} \frac{m_a + m_A}{m_b + m_B} \tag{A.11}$$

Typically, however, the Q-value is only $\sim 10^{-3} - 10^{-5}$ of the total mass of the system and we can assume $v_{CM,f} \cong v_{CM,i}$. Using eq. A.10 one obtains the relation between the angles in the laboratory and centre-of-mass systems:

$$\tan\theta_b = \frac{\sin\theta_c}{\cos\theta_c + \gamma} \tag{A.12}$$

where γ is the ratio of the velocities of the centre of mass and of the particle b in the centre-of-mass frame of reference:

$$\gamma = \frac{v_{CM}}{v'_b} = \sqrt{\frac{m_a m_b}{m_A m_B} \frac{K_a}{(1 + \frac{m_a}{m_A})Q + K_a}} \tag{A.13}$$

The second equality has been derived using eq. A.2.

Appendix B

Unfolding

As mentioned in sec. 3.2, the use of tracking algorithms can greatly improve the P/T ratio of the AGATA Demonstrator compared to traditional HPGe arrays. Unfortunately, a sizeable fraction of the measured spectrum still corresponds to Compton-scattered γ-rays. For this reason, it is possible to apply the Compton unfolding techniques implemented in the RADWARE software package and described in [70], which we will now briefly recall.

The main idea of the unfolding procedure is to subtract the Compton continuum associated to each photopeak through a deconvolution of the detector response function. The spectrum is scanned starting from the highest energy, and for each channel the background is calculated with the assumption that only photopeak counts are left in the bin and subtracted. This requires an accurate knowledge of the detector response as a function of the primary photon energy. The response function can be measured with monochromatic γ-ray sources only at selected energies, so that a dedicated technique is necessary to interpolate and extrapolate the response function at all the other energies. In particular, the technique described in [70] divides the Compton background in 3 components, corresponding to the backscatter peak, the continuum, and the Compton edge. When interpolating the experimental data, each component is transformed smoothly as a function of energy. The response function also takes into account the intensity of the first and second escape peak, which are taken as 1 channel large so that as the photopeak is scanned, two escape peaks with the same shape and width are subtracted.

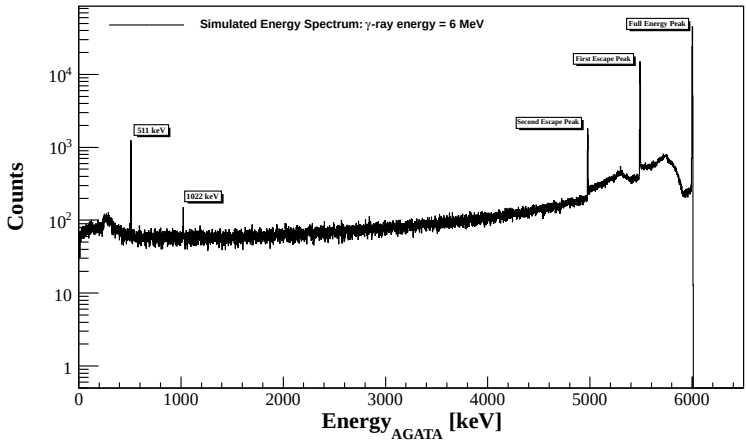

Figure B.1: Energy spectrum for a γ-ray of 6 MeV obtained with the simulation code described in [42].

In our case, the response function of the AGATA Demonstrator was computed with the GEANT4 simulation code developed by E. Farnea [42] for various photon energies, going from 1 MeV to 15 MeV. The GEANT4 code gives as an output a file containing all the interaction points for each primary event; this file was used to perform the tracking on the simulated data with the MGT code [56], which is the same we used for the experimental data. Fig. B.1 shows energy spectrum for a γ-ray of 6 MeV obtained with the simulation code described in [42].

We tuned the parameters of the unfolding algorithm on the energy spectrum measured with the AmBe-Ni source, since it is important for us to perform the procedure correctly at high energies. The results of the unfolding procedure is shown in Fig. B.2 for the AmBe-Ni spectrum: the black spectrum is the original, the red spectrum is after the unfolding. The Compton shoulder and first escape peak of the large peak at 4.4 MeV is not completely removed, probably because of the large width of the line (which is Doppler broadened, see 4.5). The blue arrows indicate the escape peaks. The unfolding procedure cleanly removes both the Compton continuum and the escape peaks.

This procedure could be applied to the experimental energy spectrum in order to subtract the Compton continuum and the escape peaks still present. Unfortunately for the ^{124}Sn the statistics in the PDR region were insufficient and too fragmented

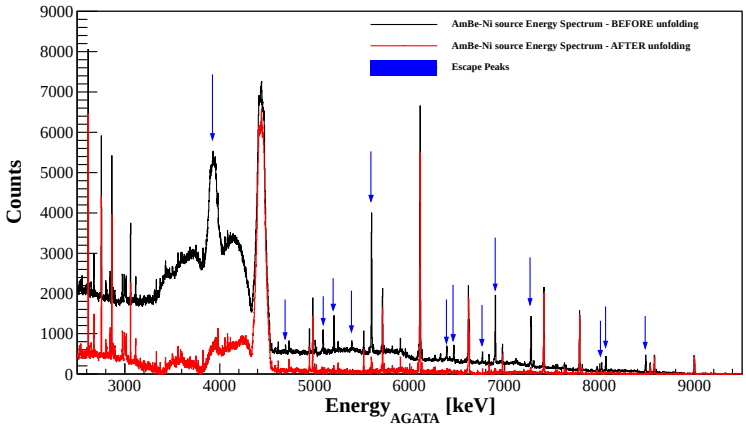

Figure B.2: Energy spectra measured with the AGATA Demonstrator for the AmBe-Ni composite source, before (in black) and after (in red) the unfolding procedure. The blue arrows indicate the escape peaks that with the unfolding procedure are clearly removed.

to applying the ufolding procedure. Anyway, this procedure has been applied on the other nuclei measured in our experiment (^{208}Pb, ^{90}Zn and ^{140}Ce).

Appendix C

FRESCO Computer Code

As mentioned in Chap. 2, all the inelastic scattering cross section calculations for our experiment were performed in the DWBA approximation by the FRESCO code [35]. The inputs required by the code are:

- the entrance and exit channels of the reaction
- the beam energy
- the energy, spin and parity of the excited state
- the depth, radius and diffusiveness for both the real and the imaginary part of the optical potential
- the nuclear deformation parameter (related to RDEF(k))
- the Coulomb deformation parameter (related to B(Ek))
- the range of scattering angles (in the centre-of-mass frame of reference) for which to perform the calculations

The parameters used for the calculation of the differential cross section are reported in Table C.1 and C.2.

Fig. C.1 shows the input of the FRESCO code for the cross section calculation for the population of the PDR states in ^{124}Sn with an ^{17}O beam at 20 MeV/u. The general variables refers to the numerical parameters used in the coupled channel

Projectile and Target parameters

Nucleus	Atomic Weight	Atomic Number	Spin and Parity
^{17}O	17	8	$\frac{5^+}{2}$
^{124}Sn	124	50	0^+

Table C.1: Projectile and target parameters for the inelastic scattering of ^{17}O+^{124}Sn

Optical potential parameters

V	R_{v0}	a_v	W	R_{w0}	a_w
50	1.16	0.67	32	1.16	0.67

Table C.2: Optical potential parameters for the inelastic scattering of ^{17}O+^{124}Sn.

calculations: *thmin* and *thmax* indicate the angular range, in the center-of-mass frame, used for the calculation, *thinc* is the angular increment; *jtmax* indicates the number of partial wave considered; *rmatch* is the maximum distant for the integration. In the "masses and states" part, the projectile and target ions characteristics are define concerning the masses, the ground and excited states. The last part of the input file is focused on the definition of the Coulomb and Nuclear potentials and the deformation parameters.

The differential cross sections for the population of the PDR states in ^{124}Sn at the beam energy used in the experiment (20 MeV/u) are shown in Fig. C.2. The highlighted red region shows the angular range covered by the Silicon Telescope detectors during the experiment.

It has to be pointed out that the calculations performed with the FRESCO code were in complete agreement with the ones performed with the PTOLEMY code.

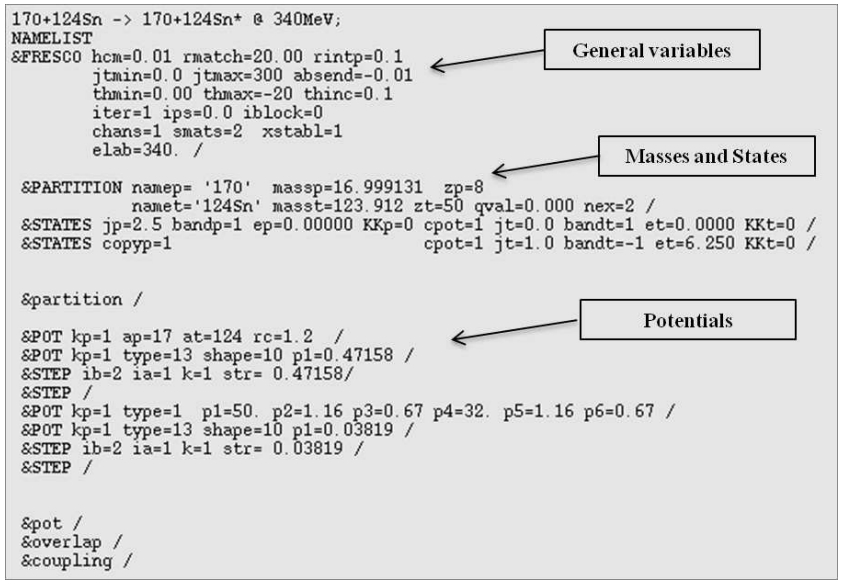

Figure C.1: Input file of the FRESCO code for the cross section calculation in DWBA for the population of the PDR states in ^{124}Sn with an ^{17}O beam at 20 MeV/u.

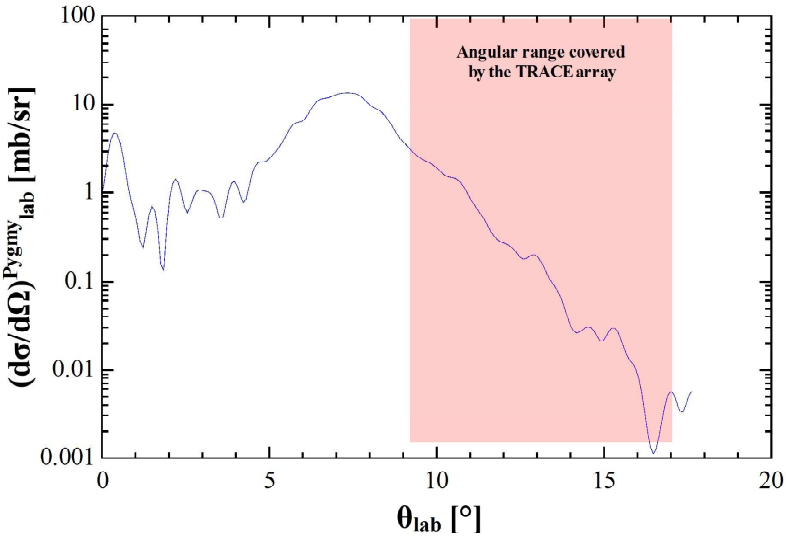

Figure C.2: Cross section calculation with the DWBA approach for the population of the 1^- states in ^{124}Sn with an ^{17}O beam at 20 MeV/u. The red region indicates the angular range covered by the TRACE array

Bibliography

[1] P.F. Bortignon, A. B. & Broglia, R. *"Giant Resonances: Nuclear Structure at Finite Temperature"* (Harwood Academic Publishers, 1998).

[2] Harakeh, M. & van der Woude, A. *"Giant Resonances: Fundamental High-Frequency Modes of Nuclear Excitation"* (Oxford University Press, 2001).

[3] Bothe, W. & Gentner, W. *Zeitschrift für Physik* **106**, 236 (1937).

[4] Goldhaber, M. & Teller, E. *Physical Review* **74**, 1046 (1948).

[5] Steinwedel, H. & Jesen, J. H. D. *Zeitschrift Naturforschung Teil A* **5**, 413 (1950).

[6] Wieland, O. *et al. Phys. Rev. Lett.* **102**, 092502 (2009).

[7] Carbone, A. *et al. Phys. Rev. C* **81**, 041301 (2010).

[8] Brown, B. A. *Phys. Rev. C* **85**, 5296 (2000).

[9] Furnstahl, R. J. *Nuclear Phys. A* **706**, 8 (2002).

[10] Goriely, S. *Phys. Lett. B* **436**, 10 (1998).

[11] Litvinova, E. *et al. Nuclear Phys.* **823**, 26 (2009).

[12] Mohan, R. *et al. Phys. Rev. C* **3**, 1740 (1971).

[13] Gambacurta, D. *et al. Phys. Rev. C* **84**, 034301 (2011).

[14] Tsoneva, T. & Lenske, H. *Phys. Rev. C* **77**, 024321 (2008).

[15] Hartmann, T. *et al. Phys. Rev. Lett.* **93**, 192501 (2004).

[16] Baran, V. *et al. Phys. Rev. C* **85**, 051601 (2012).

[17] Liang, J. *et al. Phys. Rev. C* **75**, 054320 (2007).

[18] Litvinova, E. *et al. Phys. Rev. C* **78**, 014312 (2008).

[19] Pascu, S. *et al. Phys. Rev. C* **85**, 064315 (2012).

[20] Paar, N. *et al. Rep. Prog. Phys.* **70**, 691 (2007).

[21] Paar, N. *et al. Phys. Rev. C* **67**, 034312 (2003).

[22] Savran, D. *et al. Prog. Part. Nucl. Phys.* **70**, 210 (2013).

[23] Roca-Maza, X. *et al. Phys. Rev. C* **85**, 024601 (2012).

[24] Kneissl, U. *et al. Prog. Part. Nucl. Phys.* **37**, 349 (1996).

[25] Savran, D. *et al. Phys. Rev. Lett* **97**, 172502 (2006).

[26] Endres, J. *et al. Phys. Rev. Lett* **105**, 212503 (2010).

[27] Bracco, A. & Crespi, F. C. L. In *EPJ Web Conf.*, vol. 38, 03001 (2013).

[28] Nicolini, R. *"Pygmy structures in ^{208}Pb and ^{90}Zn studied with the inelastic scattering of ^{17}O at 20 MeV/u"*. Ph.D. thesis, University of Milan (2011).

[29] Derya, V. *et al. J. Phys. Conf. Ser.* **366**, 012012 (2012).

[30] Bertrand, F. E. *et al. Nucl. Phys. A* **482**, 287 (1988).

[31] Beene, J. *et al. Phys. Rev. C* **39**, 1307 (1989).

[32] Beene, J. *et al. Phys. Rev. C* **41**, 920 (1990).

[33] Satchler, G. R. *"Introduction to Nuclear Reactions"* (Oxford University Press, 1990).

[34] Satchler, G. R. *"Direct Nuclear Reactions"* (Oxford University Press, 1983).

[35] Thompson, I. Fresco code. URL `http://www.fresco.org.uk`.

[36] Sjoreen, T. *et al. Phys. Rev. C* **29**, 1370 (1984).

[37] Mengoni, D. *"Trace: a highly-segmented Silicon detector for light charged particles emitted in fusion-evaporation and direct nuclear reactions"*. Ph.D. thesis, University of Padova (2008).

[38] Akkoyun, S. *et al. Nucl. Instrum. and Meth. in Phys. Res. A* **668**, 26 (2012).

[39] Giaz, A. *et al. Nucl. Instrum. and Meth. in Phys. Res. A* **729**, 910 (2013).

[40] Grave, X. *et al.* In *IEEE Transactions on Nuclear Science* (2005).

[41] http://www.sparrowcorp.com/products/software.
"Kmax - Advanced tools for industry, education and research".

[42] Farnea, E. *et al. Nucl. Instrum. and Meth. in Phys. Res. A* **621**, 331 (2010).

[43] Georgiev, A., Gast, W. & Lieder, R. M. In *IEEE Transactions on Nuclear Science*, vol. 41, 1116 (1994).

[44] Recchia, F. *et al. Nucl. Instrum. and Meth. in Phys. Res. A* **604**, 555 (2009).

[45] Olariu, A. *et al.* In *IEEE Transactions on Nuclear Science*, vol. 53, 1028–1031 (2006).

[46] Kröll, T. & Bazzacco, D. *Nucl. Instrum. and Meth. in Phys. Res. A* **565**, 691 (2006).

[47] Crespi, F. C. L. *et al. Nucl. Instrum. and Meth. in Phys. Res. A* **570**, 459 (2007).

[48] Boston, A. J. *et al. Nucl. Instrum. and Meth. in Phys. Res. B* **261**, 1098 (2007).

[49] Kojouharov, I. *et al.* In *IEEE Nuclear Science Symposium Conference Record*, vol. 3, 2213 (2007).

[50] Kröll, T. & Bazzacco, D. *Nucl. Instrum. and Meth. in Phys. Res. A* **463**, 227 (2001).

[51] http://mgs2005.in2p3.fr/Mgs.php. "MGS software".

[52] Crespi, F. C. L. *et al. Nucl. Instrum. and Meth. in Phys. Res. A* **620**, 299 (2011).

[53] van der Marel, J. & Cederwall, B. *Nucl. Instrum. and Meth. in Phys. Res. A* **437**, 538 (1999).

[54] Schmid, G. J. *et al. Nucl. Instrum. and Meth. in Phys. Res. A* **430**, 69 (1999).

[55] Lopez-Martens, A. *et al. Nucl. Instrum. and Meth. in Phys. Res. A* **533**, 454 (2004).

[56] Bazzacco, D. *Nucl. Phys. A* **746**, 248 (2004).

[57] Crespi, F. C. L. *et al. Nucl. Instrum. and Meth. in Phys. Res. A* **705**, 47 (2013).

[58] Avigo, R. *Caratterizzazione dei rivelatori HPGe segmentati con raggi gamma ad alta energia.* Master's thesis, University of Milan (2011).

[59] http://pro.ganil-spiral2.eu/laboratory/detectors/exogam/exogam detectors.

[60] Crespi, F. C. L. *et al. Nucl. Instrum. and Meth. in Phys. Res. A* **602**, 520 (2007).

[61] Boiano, C. *et al.* In *IEEE Nuclear Science Symposium Conference Record*, 2068 (2008).

[62] Knoll, G. *"Detector and Radiation measurements"* (Winley, 2010).

[63] Grave, X. *et al.* In *Real Time Conference, 2005. 14th IEEE-NPSS* (2005).

[64] Govaert, K. *et al. Phys. Rev. C* **57**, 2229 (1998).

[65] Endres, J. *et al. Phys. Rev. C* **85**, 064331 (2012).

[66] Lui, Y. W. *et al. Phys. Rev. C* **70**, 014307 (2004).

[67] Morinaga, H. *"In-Beam Gamma-Ray Spectroscopy"* (Elsevier Science Ltd, 1977).

[68] Iimura, H. *Nuclear Data Sheets* **80**, 895 (1997).

[69] Horen, D. *et al. Phys. Rev. C* **44**, 128 (1991).

[70] Radford, D. C. *Nucl. Instrum. and Meth. in Phys. Res. A* **258**, 111 (1987).

Acknowledgements

Alla fine di ogni lungo e complesso lavoro è doveroso ringraziare le persone che l'hanno reso tale. Innanzi tutto vorrei ringraziare la prof.ssa Angela Bracco per avermi proposto questo lavoro di tesi, per i preziosi consigli e per l'interesse mostrato.
Un grosso grazie va anche a tutto il gruppo di spettroscopia gamma di Milano per l'aiuto durante l'esperimento e per il supporto datomi durante l'analisi. In particolare vorrei ringraziare il prof. Franco Camera, il dott. Sergio Brambilla e il dott. Ciro Boiano che con grande sforzo hanno messo a punto l'elettronica e l'acquisizione dati. Senza di voi l'esperimento non sarebbe mai partito.
Parlando della parte sperimentale, non posso che ringraziare tutto il gruppo di AGATA di Padova e Legnaro che ha svolto un ruolo fondamentale sia durante la presa dati che dopo l'esperimento, per la parte di presorting dei dati di AGATA. In particolare ringrazio il dott. Dino Bazzacco, il dott. Daniele Mengoni, il dott. Francesco Recchia, il dott. Enrico Farnea, la dott.ssa Caterina Michelagnoli, il dott. Javier Valiente e il dott. Andrea Gottardo.
Un ringraziamento speciale va al dott. Fabio Crespi che, con grande pazienza, mi ha aiutato in questa complessa analisi dati (soprattutto nei momenti di sconforto durante la correzione dei drift dei silici....).
Grazie anche al dott. Oliver Wieland per avermi fatto da cotutor e per avermi letto e corretto la tesi.
Moreover, I would like to thank prof. Elias Khan for agreeing to referee this thesis and for the constructive comments.
Un ringraziamento particolare va alle mie compagne di ufficio: Valeria, Anabel e Agnese. Grazie per tutti i momenti condivisi in questi anni di lavoro, per tutte le trasferte e per tutti i turni di notte fatti insieme. Ringrazio anche Simone C., Riccardo, Simone B. e Giovanna per le pause pranzo, per le trasferte e le giornate

di lavoro insieme.

Un ringraziamento molto molto speciale va alla Fede e al Giova che sono stati, prima che compagni di università, dei grandi amici. Grazie per avermi supportato e sopportato in questi anni e per essermi stati veramente vicino quando ne ho avuto bisogno. Non smetterò mai di ringraziarvi.
Grazie mille agli amici di sempre: Fabio, Ricco, Doni e Lety; anche se ci si vede poco, vi ho sempre nel cuore.
Grazie ai miei amici Disagiati per le serate folli di questi ultimi anni.
Grazie anche ai ragazzi del golf che intrattengono le mie domeniche sportive con dei discorsi molto molto interessanti (dove è il tee, dove è il tee...).
Grazie alle mie vecchie, Fede e Vero, e nuove, Lelina, coinquiline per aver condiviso con me i miei primi anni (deliranti) fuori casa.
Grazie alla Maurina, al Dema e a Stewe che hanno assecondano la mia idea malsana di seguire il corso di Cinese, xièxie.
Grazie agli abitanti, vecchi e nuovi, della Nuova Zelanda. La mia esperienza universitaria non sarebbe mai stata la stessa senza di voi.

Last but not least: grazie alla mia amica Francesca. Grazie per essere la persona che sei. Non smetterò mai di ringraziarti per avermi tenuto a galla in questi ultimi anni, per avermi ascoltata, compresa e aiutata sempre e comunque. Grazie perchè senza di te la vita sarebbe molto ma molto più triste. Ti voglio bene amica mia.

E ora il ringraziamento più importante di tutti: grazie infinitamente alla mia famiglia. Grazie a Mamma e Papà che mi sono sempre stati vicini, che mi hanno sempre supportata e spronata ma che sopratutto mi hanno insegnato a non mollare mai. Grazie di cuore. Vi adoro.
Un grazie particolare va al mio fratellino, il Moccio. Sei veramente una persona speciale. Spero con tutto il cuore che tu riesca a realizzare tutti i tuoi sogni perchè te lo meriti veramente.

Ed infine vorrei ringraziare tutte le persone che sono arrivate, che sono passate, che se ne sono andate e che sono sempre rimaste: è grazie a voi che sono diventata la persona che sono oggi. GRAZIE.